Excitation waves on complex networks

vorgelegt von Diplom-Physiker
Thomas Marius Isele
aus Hamburg

Von der Fakultät II – Mathematik und Naturwissenschaften
der Technischen Universität Berlin
zur Erlangung des akademischen Grades eines
Doktor der Naturwissenschaften
–Dr. rer. nat.–

genehmigte Dissertation

Promotionsausschuss:

Vorsitzender: Prof. Dr. Mario Dähne
Berichter: Prof. Dr. Eckehard Schöll, Ph.D.
Berichter: Dr. Astero Provata

Tag der wissenschaftlichen Aussprache: 17. Dezember 2014

Berlin 2014
D 83

To my dear parents Gabriele and Wolfgang Isele.

Acknowledgements

I would like to thank Prof. Schöll for his supervision, providing me with a research assistant position and teaching me how to work independently; Dr. Philipp Hövel for regular helpful discussions and carefully reading the manuscript; Dr. Astero Provata for coming from Athens to be in the committee shortly before Christmas; Judith Lehnert for helpful discussions and having the patience to listen to my first rehearsal defense talk; Paul Geffert and Peter Kalle for listening to my second rehearsal defense talk and giving helpful feedback; Benedikt Hartung for being a good collaborator (congratulations on your excellent Bachelor's degree); Niklas Hübel for being the most pleasant, relaxed and fun office mate, who also became a friend; the entire AG Schöll for always creating a good, fun and friendly atmosphere (including excellent espresso "MK1"); my parents for supporting me through all those crooked paths that finally led me here and last but not least my girlfriend Joanna Scheffel for being patient, sweet and (when necessary) stern.

Abstract

In this thesis, we study the propagation of excitation waves emerging on many units of FitzHugh-Nagumo systems that are coupled by complex network structures. We focus on several different model network structures that are important in the study of complex network systems. These are regular ring networks, regular tree networks, minimal small-world models and Newman-Watts small world models.

For excitation waves on regular ring networks, we study two limiting regimes (high and low coupling strength) with special focus on the points in this regime where stable waves become unstable. Using numerical simulation and continuation, we show that the destabilization at low coupling strength together with that at high coupling strength implies that the total range of admissible coupling strengths for wave propagation is finite and the dispersion relation is given by a closed curve.

In the study of regular tree networks, we find a critical degree of the non-leaf nodes which depends on the coupling strength and above which no wave propagation is possible. We calculate this critical degree in the high coupling strength regime using profile equations of an approximate continuum system and kinematical theory. In the low coupling strength regime we are able to successfully apply the so-called active point approximation. Using this, we predict and find an optimum value of the coupling strength at which the critical degree is highest. Finally, we apply our findings to wave propagation on Erdős-Rényi random networks.

In the study of minimal small-world networks, seemingly simple systems that consist of a ring network with one additional link, we discover a host of intricate dynamical patterns. These patterns include period multiplications, propagation failure, generation of secondary waves and more. We study the mechanisms and conditions which lead to the generation of these patterns in detail using numerical simulations. We find that the patterns can be selected by simply adjusting the coupling strength and the distance that the additional link spans. Moreover, we study the influence of network size and coupling range on the occurence of these patterns. Finally, we perform analytical approximations for some transition thresholds in the system.

Last but not least we study the influence of Newman-Watts small-world topologies on excitation wave propagation. Our findings agree with that of other authors in that a high number of additional long-range links leads to propagation failure. However, we study this system in the full range of admissible coupling strengths, discovering different behavior in the regimes of low and high coupling strength. In the low coupling strength regime we are able to apply some of the results of our study of minimal small-world networks and calculate the transition to propagation failure. In both high and low coupling strength regime, we study the scaling behavior with respect to system size and coupling range.

Our results have implications for the understanding of the generation of spatio-temporal patterns in network systems. Many of the mechanisms for propagation failure and pattern generation are general and not restricted to the particular dynamics we employed. Moreover, small-world topologies are ubiquitous in the physical world and the understanding of wave propagation on these could prove important.

Zusammenfassung

In dieser Dissertation untersuchen wir die Ausbreitung von Erregungswellen auf komplexen Netzwerken von FitzHugh-Nagumo Systemen. Wir konzentrieren uns auf einige unterschiedliche Netzwerkmodelle, die für die Erforschung von komplexen Netzwerken wichtig sind. Bei diesen handelt es sich um reguläre Ringnetzwerke, reguläre Baumnetzwerke, minimale kleine-Welt-Netzwerke und Newman-Watts kleine-Welt-Netzwerke.

Bei Erregungswellen auf regulären Ringnetzwerken untersuchen wir zwei Grenzbereiche (sehr hohe und sehr niedrige Kopplungsstärken), wobei unsere Aufmerksamkeit auf jenen Punkten in diesen Bereichen liegt, an denen stabile Wellen instabil werden. Wir benutzen numerische Simulation und Lösungsverfolgung um zu zeigen, dass die Destabilisierung bei niedrigen, zusammen mit der bei hohen Kopplungsstärken impliziert, dass der Gesamtbereich von Kopplungsstärken, für die Wellenausbreitung möglich ist, endlich ist und dadurch die Dispersionsrelation durch eine geschlossene Kurve dargestellt wird.

Für Baumnetzwerke zeigen wir, dass es einen kritischen Grad der Knoten (Blätter ausgenommen) gibt, der von der Kopplungsstärke abhängt und überhalb dessen keine Ausbreitung von Erregungswellen möglich ist. Wir berechnen diesen kritischen Grad mithilfe von Profilgleichungen einer Kontinuumsnäherung und der kinematischen Theorie. Im Bereich niedriger Kopplungsstärken können wir erfolgreich die sogenannt Aktive-Punkt Näherung zur Anwendung bringen. Mithilfe dieser können wir einen optimalen Wert der Kopplungsstärke vorhersagen und berechnen, bei der der kritische Grad ein Maximum annimmt. Abschliessend wenden wir die gewonnenen Ergebnisse auf die Ausbreitung von Erregungswellen in Erdős-Rényi Zufallsnetzwerken an.

Bei der Erforschung von minimalen kleine-Welt-Netzwerken, scheinbar einfachen Systemen, die aus einem regulären Ring mit einer einzigen zusätzlichen Kante bestehen, entdecken wir eine große Menge komplizierter dynamischer Muster. Beispiele dieser Muster sind Periodenvervielfachungen, Ausbreitungsunterdrückung, die Entstehung von Sekundärwellen und mehr. Wir untersuchen die Mechanismen und Bedingungen die zur Entstehung dieser Muster führen im Detail mithilfe von numerischen Simulationen. Es stellt sich heraus, dass aus diesen Mustern mithilfe von lediglich zwei Parametern, der Kopplungsstärke und der Entfernung die die zusätzliche Kante überbrückt, ausgewählt

werden kann. Des weiteren untersuchen wir den Einfluss der Netzwerkgröße und der Kopplungsreichweite auf das Vorhandensein dieser Muster. Um diesen Teil abzurunden führen wir noch analytische Näherungen einiger Schwellwerte in diesem System durch.

Zu guter Letzt untersuchen wir den Einfluss von Newman-Watts kleine-Welt Topologien auf die Ausbreitung von Erregungswellen. Unsere Ergebnisse stimmen insofern mit denen anderer Autoren überein, als dass eine hohe Anzahl zusätzlicher Kanten zu Ausbreitungsunterdrückung führt. Allerdings untersuchen wir das System im kompletten Bereich der zulässigen Kopplungsstärken und entdecken unterschiedliches Verhalten im Bereich kleiner und großer Kopplungsstärken. Im Bereich niedriger Kopplungsstärken können wir erfolgreich einige Ergebnisse aus der Untersuchung von minimalen kleine-Welt-Netzwerken anwenden und den Übergang zu Ausbreitungsunterdrückung berechnen. Sowohl im Bereich hoher, als auch im Bereich niedriger Kopplungsstärken untersuchen wir das Skalierungsverhalten in Bezug auf Netzwerkgröße und Kopplungsreichweite.

Unsere Resultate haben Auswirkungen auf das Verständnis der Entstehung raum-zeitlicher Muster auf Netzwerksystemen. Viele der Mechanismen für Ausbreitungsunterdrückung und Musterbildung sind allgemein für anregbare Dynamiken gültig und nicht auf das konkrete, von uns benutzte Beispielsystem (FitzHugh-Nagumo) beschränkt. Außerdem sind kleine-Welt-Netzwerke in unserer Welt allgegenwärtig und ein verbessertes Verständnis für Wellenausbreitung auf diesen könnte sich als sehr nützlich erweisen.

Contents

Chapter 1

Introduction

1.1 Excitation waves

Excitability describes the reactions of a nonlinear dynamical system to perturbations of its stable steady state. When perturbed only a little, the system will fall back to this stable steady state immediately. However, when the perturbation surpasses a certain threshold, the system will show a strong reaction in making a large excursion in its phase space after which it returns to the stable steady state again. A very important characteristic of an excitable system is the refractory time after an excitation. Only after a certain amount of time has passed after an excitation, the system can be excited again.

There are many examples for excitable systems, arguably the most prominent being that of a nerve cell which fires an action potential in response to a stimulus. Another example is a forest, which burns down when for example a lightning strikes. After having burnt down it takes a couple of years until the forest has grown back so densely that a lightning would cause a forest fire again.

Excitable media are spatially extended dynamical systems that have local dynamics that are excitable. Neighboring points are interacting via some process like e.g. diffusion. In such an excitable medium, excitation waves occur. An excitation wave can be described as the localized departure from a quiescent state (the stable steady state) at some place in the system which then propagates through the medium mediated by the spatial interaction processes. During an excitation wave, an area that is excited exerts above-threshold stim-

uli to neighboring areas and thus recruits these into becoming excited as well. This way, an excitation wave that is propagating through the medium also features a refractory tail which consists of the areas that have just undergone excitation and are now in the refractory phase of the local excitable dynamics.

Excitation waves are commonly used model systems in a wide area of applications. Examples include the propagation of electrical impulses in different biological tissues [1, 2, 3], chemical reactions [4, 5] and waves of spreading depression in the cortex [6, 7, 8]. The influence of nonlocal, long-range coupling upon wave propagation has been studied in [9, 10, 11, 12, 13].

1.2 Excitation waves on networks

Many systems in the world that we live in are best described by complex networks; discrete units, coupled together in complex patterns which define the interactions between the units. The study of dynamical systems that are coupled to form complex networks and the emerging dynamics, which can differ in its collective behavior from the behavior of the individual units is a research topic that has received much attention during the past years [14, 15, 16, 17, 18, 19, 20, 21]. Various phenomena known from spatially extended systems can be transferred to complex networks. This has been demonstrated for e.g. Turing patterns [22] and front propagation [23, 24] and also to some extent for activity in excitable media [25, 26].

In this thesis, we investigate the question how excitation spreads through a network of excitable units. How does the topology influence the propagation process? What dynamical patterns can arise and how is the stability affected? Moreover the influence of the generic discreteness of systems organized in network architecture is of interest as is the structure of the solutions, when the size of the network is varied.

To adress these questions some forethoughts are necessary and helpful. In general, the notion of a wave implies that there is some spatial expansion of the system that carries the wave. Networks in general do not need to be embedded in space, they can be a purely abstract construct, e.g. a social network. However, on networks, a natural measure of distance between two nodes is given by the minimal number of links that have to be traversed in order

to get from one to the other. In many network architectures that are studied in the context of complex networks, the average distance between two nodes is very small, though the network can be very large. A famous popular expression for this phenomenon is that any two humans in this world are, on average, connected by a chain of no more than six acquaintances. The consequence for excitation waves is that ongoing activity in the form of spreading excitation is not found on such networks because every node of the network will be reached in very short time and after that a re-excitation will be made impossible by the refractory phase of the underlying excitable system so that the network quickly ends up being completely in the quiescent state again [26].

On the other hand, modifications of the spatial structure of an excitable medium have an influence on the properties of traveling waves. Examples of these in the literature concern the influence of curvature and inhomogeneities [27, 28, 29, 30].

We want to take a different approach and study excitation waves on network structures that –though they have no direct analogue in continuous systems– arise as modifications of very regular network structures. The regularity of the initial network structure provides a notion of space that we need in order to have an understanding of what a wave is. Even if the initial network structure is left unmodified, its discreteness will have an influence on the propagation of waves.

The network structures we will be investigating in this thesis are (regular) tree networks, Newman-Watts small world networks and networks that we call *minimal small world* networks. Regular tree networks are well suited model systems to study the influence of a node's degree because in such a network, every node has the same degree. Under some conditions the results from regular tree networks can be applied to other networks which makes them even more attractive. Newman-Watts small-world networks [31] arise by adding links randomly to a ring network. We use this particular prescription for generating small-world networks instead of the Watts-Strogatz prescription [32] because in the latter, links are deleted, and thus the space-like structure is destroyed. Small-world networks are an interesting study object because on the one hand, as the number of added links rises, the average distance goes down and the collective effect will lead to failure of the propagating traveling wave

solution. On the other hand, secondary excitations can be triggered through the additional links. For small-world networks however, all statements are statements about the average over many realizations with the same number of added links, as the number of added links alone does not fix the topology. Even with a few added links, the possibilities to distribute them are extremely numerous, and cannot really be put into a useful scheme. In contrast, minimal small-world networks are ring networks with exactly one added link which is the smallest possible dose of small-world modification, hence the name. We are interested in studying them because they allow us to exactly extract the effect that an additional link has on wave propagation and hopefully trace back some of the effects encountered in the study of small-world networks to these effects. An added link in a ring network is a nonlocal yet localized modification because it connects distant points but does so only in one or two places, respectively. This sort of modification is generic to the network structure of the system, yet the regularity of the underlying ring network is important, otherwise it would not be possible to speak of distant nodes in that sense.

1.3 Existing work

Some work on the matter we want to pursue has already been accomplished. We want to give a short (by no means complete) outline of the results in this particular field. We restrict ourselves to results that will prove useful later on or for which we could help deepen the understanding.

In [33], wave propagation in a discrete excitable medium is studied. The author finds a critical coupling strength below which the propagation of excitation waves does not take place. Moreover, she analytically estimates this critical coupling strength by using the time scale separation of the underlying system in a method that is versatile and useful. We will use variations of this method in Chapters 5 and 6. She also describes the propagation on the discrete medium (in the regime of low coupling strengths) as *saltatory*, by which she means that excitation is passed from cell to cell of the discrete medium in a temporally well separated manner. Other work that is concerned with this problem is found in [34], where also the failure of propagation in a discrete excitable medium is studied. There, the authors investigate in detail

the phenomena that occur before the actual failure. We will observe similar phenomena in a different context (above the critical coupling strength) in Chapter 6. It remains to say that from the network perspective, all these works are concerned with regular lattices. In more complex topologies we expect to find more consequences of the inherent discreteness; the results of the above mentioned articles will help our understanding of these.

The authors of [23] study front propagation on bistable units organized in regular tree architectures. Their interesting results show that the degree of a node can have a large impact on the propagation of fronts. They observe pinning of fronts up to reversal of the propagation direction. We want to emphasize that the pinning in this case is of different origin than that on discrete lattices. On trees, the branching ratio (and thus the degree of the nodes) is causing the pinning and even the reversal of the propagation direction at coupling strengths at which on a regular lattice fronts would propagate normally. In that work, the result from the regular trees is also successfully applied to front propagation on random networks. We will build upon this work and do a similar analysis for excitable units instead of bistable ones in Chapter 5.

Excitable units organized in small-world architectures have been studied in [25] and [26]. In both articles, the focus lies on the emergence of self-sustained patterns from initial conditions which would not lead to ongoing activity on a regular lattice instead of a small-world architecture. In [25], the excitable units under consideration are integrate-and-fire neurons which are pulse coupled with a delay. It is noteworthy at this point that traveling waves in this system are only possible because of the delay in the coupling and the velocity of waves in this system is directly related to the delay. Even though this model is very simple and in some respect artificial, it already shows some of the properties that we will also encounter when investigating the influence of small-world topologies on wave propagation in Chapter 7, namely that a density of additional links that exceeds a certain threshold supresses ongoing activity. In [26], a discrete time model of excitability (that of [35]) is used for the individual cells. The results of this article are in accord with the former one in that above a critical density of shortcut links no persistent activity is possible. The authors exemplarily look at the dependence with

respect to system size and coupling strength. The dependence on coupling strength however is investigated only within a very small range. Moreover, in both articles, the different effects that one single link can have depending on coupling strength is not adressed. Also the effect of varying the coupling range of the underlying regular lattice network is not taken into account.

1.4 Goals

Having achieved an overview about existing results, we are now in a position to define in more detail the goals of this thesis. First of all, we want to use a generic, continuous time model for excitability, as the 'finer resolution' of a continuous time model is better suited to discover subtleties that can arise in the interplay of many units in a complex network. We want to use only bidirectional links in our network because firstly, this will make it easier to define a continuum limit and secondly we think it is more natural to assume that two units that are coupled exert mutual influence rather than unidirectional only. From [33], we have learned that for low global coupling strengths, the propagating wave solutions on a regular lattice show behavior that is due to the discreteness of the system. On the other hand, in numerics, regular lattices are used as discretizations of spatially continuous system. We want to look at this from a network perspective and find the appropriate limit in which solutions on a discrete network system are best described by a limiting continuous system. In anticipation of the results of Chapter 4, we can already say that this will be the case for high global coupling strengths. This sets the goal for each studied system to explore the full range of possible global coupling strengths and comparing solutions in the low coupling strength discrete regime with those in the high coupling strength continuum regime. When possible, we also want to apply appropriate modifications of the analytic methods provided by [33] to our network systems in the discrete regime. Wherever applicable, we also want to find out about the influence of the coupling range, a parameter that has no direct analogue in continuous models.

With regular tree networks, we want to investigate the influence of the degree of a node on the existence and properties of traveling wave solutions. Using regular tree networks, we can also pursue the question how excitation on

a network can spread most effectively, meaning that it reaches as many nodes as possible within a certain time. If possible, we want to apply the results obtained from the study of regular tree networks to network structures that can in some limit locally be approximated by tree networks. In [23], this has been done for random networks.

Before turning our attention to full-blown Newman-Watts small-world networks that feature many additional long-range links, we want to find out about the effect of the elementary modification applied in constructing these networks. To this end we investigate what we call *minimal small-world networks*, regular ring networks that have one additional link. We want to find out how this one additional link modifies the behavior of the traveling wave. Is one additional link in the right/wrong place enough to cause propagation failure? What are the conditions for those effects and what are the dynamical mechanisms?

In Newman-Watts small-world networks, we want to investigate the behavior over the entire range of coupling strengths that allow wave propagation. We are also interested in whether the effects found for minimal small-world networks can under some conditions be used to understand or even predict the behavior of waves on small-world networks. Also, for small-world as well as minimal small-world networks, we are interested in the influence of the network size and the coupling range.

1.5 Outline

In Chapter 2, we summarize the network theory concepts that are used within this thesis. Section 2.1 reviews the fundamentals of network theory and explains how the structure of a complex network can be used to define the coupling between dynamical units. Sec. 2.2 gives a short account on network measures. In Sec. 2.3, those network models used in this thesis are introduced and explained. These are regular lattices in Sec. 2.3.1, regular tree networks in Sec. 2.3.2, random networks in Sec. 2.3.3 and small-world networks in Sec. 2.3.4.

In Chapter 3, we introduce the FitzHugh-Nagumo system, a generic continuous time model for excitable dynamics. In Sec. 3.1, general properties of

excitable systems are explained in some detail as well as the different variants of those systems. Sec. 3.2 gives a detailed account on the behavior of the FitzHugh-Nagumo system. A special focus is put on the mechanism of how excitability emerges in the FitzHugh-Nagumo model. For this, fast and slow subsystems are introduced as limit cases in Secs. 3.2.1 and 3.2.2 as well as the canard phenomenon in Sec. 3.2.3. In Sec. 3.2.4, we explain how the interplay of these ingredients leads to the emergence of excitable behavior in the FitzHugh-Nagumo system. With Sec. 3.3, the chapter is closed by an account on the conditions under which the stable steady state of the FitzHugh-Nagumo system leads to a stable homogeneous steady state of the spatially extended FitzHugh-Nagumo system. Put differently, we calculate the conditions for Turing instabilities in a FitzHugh-Nagumo reaction-diffusion system.

After the prelude of Chapters 2 and 3, Chapter 4 introduces the principal theme whose variations are at the heart of this thesis: Traveling excitation wave solutions of the FitzHugh-Nagumo system on regular lattice network and on a spatially continuous FitzHugh-Nagumo reaction-diffusion system. Sec. 4.1 is concerned with excitation waves in the spatially continuous system. We give a detailed account on the methods that can be used to calculate the dispersion relation in Sec. 4.1.1, whereas Sec. 4.1.2 discusses in detail the methods that need to be employed in order to compute spectra and assess the stability of the traveling wave solutions. In Sec. 4.2 we look at the traveling wave solutions that exist on one-dimensional discrete lattices of FitzHugh-Nagumo units. In Sec. 4.2.1, we develop the appropriate limit in which the discrete lattice system converges to a continuous reaction-diffusion system of the previous section. Sec. 4.2.2 discusses the properties of traveling wave solutions on the regular lattice in the discrete regime. We conclude the chapter with Sec. 4.2.3 by giving a summarizing acount of the behavior of traveling wave solutions throughout the entire possible range of coupling strengths also taking into account the influence of the size of the lattice and the coupling range. At this point we first encounter the different scaling behaviors in the discrete and in the continuum regime of the coupling strength.

Chapter 5 treats excitation waves on regular tree networks. First, we introduce the model and some first general observations in Sec. 5.1.1. We observe that above a certain critical degree, no excitation wave propagation is possible

on tree networks. In Sec. 5.1.2, we explain an important simplification of the model, that is used throughout the rest of the chapter. Sec. 5.2 is concerned with the regime of high coupling strengths. In addition to successfully using the continuum regime methods of Chapter 4, an analytical calculation along the lines of the kinematical theory of [36] is done in Sec. 5.2.2. In Sec. 5.3, we are concerned with the low coupling strength discrete regime for excitation waves on tree networks. We study this by means of direct numerical continuation in Sec. 5.3.1 and a modification of the analytic method of [33] in Sec. 5.3.2. Finally, we apply our results to the case of Erdős-Rényi random networks in Sec. 5.3.3

In Chapter 6, we study the effects that are imposed on wave propagation by a single added link to a regular ring network. We introduce these minimal small-world network models and its symmetries in detail in Sec. 6.1. In Sec. 6.2, we give detailed accounts on all different behaviors that we observed. Sec. 6.3 summarizes the different behaviors that one additional link can cause in a so-called *phase diagram*. The dependence of these phase diagrams on system size and coupling range is studied in Sec. 6.3.1 for low, in Sec. 6.3.2 for high and in Sec. 6.3.3 for intermediate coupling strengths. In Sec. 6.4 we perform analytical calculations for the location of some transitions in the phase-diagrams.

In Chapter 7, we consider the collective effects of many additional links on wave propagation. In Sec. 7.1, we first shortly introduce the model and the general observations made. In Sec. 7.1.1 we explore the low coupling strength discrete regime. Here we are able to apply some of the results obtained for minimal small-world models in the previous chapter. In Sec. 7.1.2 we investigate the high coupling strength continuum regime and perform a detailed analysis of the scaling behavior at high coupling strengths. In Sec. 7.1.3, we very briefly report on the finding of an optimum coupling strength. In Sec. 7.2 we construct a mean-field approximation for excitation wave propagation on Newman-Watts small-world network models. Finally, we successfully use this mean-field approximation to predict the critical number of additional links that quenches wave propagation in the limit of large coupling strengths.

Chapter 2

Complex networks

There are many examples of real-world systems that can be described as complex networks. We ourselves form social networks of friendships and collaborations, use transportation networks and the world-wide-web, consist of delicately balanced networks of protein interactions and think with a huge, very complex network of neurons in our head. A network can be very concrete, embedded in real space and tangible, like a city's public transportation network or it can be abstract, i.e., not linked to physical space at all, like the network of scientific collaborations. Connections in a network can be undirected (e.g. "A played chess against B, thus B also played chess against A") or directed (e.g. "A taught playing chess to B"). Connections can also be all alike, or they can be differing in strength (e.g. close friends vs. acquaintances). The mathematical basis for the description of networks is graph theory [37], whose birth is most commonly traced back to Leonhard Euler's solution to the Königsberg bridge problem in 1736 [38]. Originally, graph theory was mostly concerned with small, more or less regular networks. In more recent times the interest in large to very large (thousands to millions of nodes) networks that at first display no regular construction patterns has grown immensely [39, 20, 19]. Statistical properties, evolution of and dynamics controlled by the topology of complex networks are in the focus of current research [32, 14, 22, 40, 41, 17] as well as applications [42, 43, 44, 45].

This chapter is structured as follows: We review the basic concepts and notions from the theory of complex networks that are needed to understand the remainder of this thesis in Sec. 2.1. This includes fundamental definitions,

like directed and undirected networks, link weights, adjacency and Laplacian matrix. Our elaboration on these matters follows [19] very closely. In Sec. 2.2, we introduce some network measures that are used to describe statistical properties of networks and we present those network models that are used later on in this work in Sec. 2.3.

2.1 Fundamentals

Formally, a network or graph consists of a set $\mathfrak{N} \neq \emptyset$ of *nodes* and a set $\mathfrak{L}$ of *links* (or *edges*). A link is described by the pair of nodes that this link connects. If these are ordered pairs, we speak of a *directed* network, if they are not ordered, the network is said to be *undirected*. Two nodes that are connected are called *neighbors*. We prevent multiple edges between the same nodes and links of a node to itself by additionally requiring that a link is described by a distinct (ordered) pair of distinct nodes. In a graphical representation, directed links are usually visualized by an arrow between the two nodes, whereas undirected links are simply drawn as a line. The number of links that start (end) in a certain node j are called the *out- (in-)degree* $k_j^{\text{out}}(k_j^{\text{in}})$ of a node. In an undirected network both coincide and we simply speak of the degree k_j. The *size* $N = |\mathfrak{N}|$ of the network is the number of elements of $\mathfrak{N}$. In an undirected network with N nodes, $|\mathfrak{L}| \leq N(N-1)/2$. A graph is said to be *dense* if $|\mathfrak{L}| = \mathcal{O}(N^2)$ and *sparse* if $|\mathfrak{L}| \ll N^2$.

If a third set $\mathfrak{W}$ with entries from $\mathbb{R}$ and $|\mathfrak{W}| = |\mathfrak{L}|$ is given, the network is called *weighted*. For such a network, every link effectively has a number attached, marking e.g. the strength of the connection or the distance. For weighted networks, the (in/out) *strength* of a node is defined similarly to the degree by adding all weights of all (in/out) links of that node.

2.1.1 Adjacency, Laplacian and Incidence matrix

To describe a network by its sets of nodes $\mathfrak{N}$ and edges $\mathfrak{L}$ is only one possibility. More common, at least in the physics community, is the definition by the

adjacency matrix $\mathcal{A}$ which is a $N \times N$-matrix defined by

$$\mathcal{A}_{ij} = \begin{cases} 1 & \text{if there is a link from node } j \text{ to node } i \ (\Leftrightarrow (j,i) \in \mathfrak{L}) \\ 0 & \text{else} \end{cases}, \tag{2.1}$$

where we have implicitly used a bijection between $\mathfrak{N}$ and $\{1, 2, .., N\}$. The adjacency matrix for an undirected network is always symmetric.

Using the adjacency matrix, the (in- and out-)degree of node i are given by

$$k_i^{\text{in}} = \sum_{j=1}^{N} \mathcal{A}_{ij}\,, \qquad\qquad k_i^{\text{out}} = \sum_{j=1}^{N} \mathcal{A}_{ji}\,. \tag{2.2}$$

For undirected networks, in- and out-degree are not distinguished as both coincide.

The *Laplacian matrix* $\mathcal{L}$ of a network is defined by

$$\mathcal{L}_{ij} = \mathcal{A}_{ij} - \delta_{ij} k_j^{\text{in}}\,, \tag{2.3}$$

where δ_{ij} is the Kronecker symbol. By construction, 0 is always an eigenvalue of $\mathcal{L}$ (with eigenvector $(1, 1, ...1)^\top$) and the row sum $\sum_{j=1}^{N} \mathcal{L}_{ij} = 0$. The Gershgorin circles of $\mathcal{L}_{ij}$ are those circles that have their center at $\mathcal{L}_{ii}$ and have radius $\sum_{j\neq i} |\mathcal{L}_{ij}|$. By construction, the diagonal elements $\mathcal{L}_{ii}$ are negative and $\sum_{j\neq i} |\mathcal{L}_{ij}| = \sum_{j\neq i} \mathcal{L}_{ij} = -\mathcal{L}_{ii}$. Thus, all Gershgorin circles of $\mathcal{L}_{ij}$ are located in the left half-plane including zero. The Gershgorin circle theorem [46] states that for a quadratic matrix with entries from $\mathbb{C}$, all eigenvalues are located in the union of its Gershgorin circles. This immediately implies that all eigenvalues of the Laplacian matrix are located in the left half-plane including zero and thus have non-positive real part.

A lot of information about the topology of the underlying network can be extracted from the spectra of the adjacency and Laplacian matrix. For example, the multiplicity of the eigenvalue 0 of the Laplacian matrix is equal to the number of connected components of the network. However, an exhaustive account on this is beyond the scope of this chapter and we refer to [19] and references therein.

Both $\mathcal{A}$ and $\mathcal{L}$ can be generalized to weighted networks, replacing the entries "1" in the definition of $\mathcal{A}$ by the pertaining weight. The generalization of the adjacency matrix is usually called the *weight matrix*.

For completeness, we want to introduce the *incidence matrix* $\mathcal{B}$ for unweighted networks as well. $\mathcal{B}$ is a $N \times |\mathfrak{L}|$-matrix defined for undirected networks by

$$\mathcal{B}_{ij} = \begin{cases} 1 & \text{if link } j \text{ is incident to node } i,\ i \in \mathfrak{N},\ j \in \mathfrak{L} \\ 0 & \text{else} \end{cases} . \tag{2.4}$$

For directed networks, the nonzero entries are either 1 or -1 depending on whether the link enters or leaves the node. The Laplacian matrix can be expressed by $\mathcal{L} = \mathcal{B}\mathcal{B}^\top$.

2.1.2 Dynamics on networks

Complex networks are widely used to model physical, biological and social processes [47]. The nodes of a network can be considered as dynamical entities and the links between them as the influence these entities exert on each other. The topology of the network has a great impact on the possible solutions, even details of the topology can be very important [45]. In most real world systems, the dynamics will also have an influence on the topology, as for example in neurophysiological learning processes modeled by Hebbian learning [48]. However, as long as the evolution of the network takes place on a much larger timescale than the dynamics, the simplification of dynamics on a static topology is justified. This timescale separation holds for many real-world systems [39].

In this work we are solely concerned with time-continuous dynamical systems on static network topologies. Next, we want to give a short overview about the notations and terms used. Let

$$\dot{u} = f(u; \alpha)\,, \tag{2.5}$$

be a dynamical system, with $u \in \mathbb{R}^m$, $\alpha \in \mathbb{R}^p$ and the dot the derivative with respect to time t. u is referred to as the *dynamical variable(s)* and α are the *parameters*. Equation (2.5) is called the *local dynamics*. First we assign a copy of this system to every node of a network $(\mathfrak{N}, \mathfrak{L})$ so that we write u_i for the value of the dynamical variables on node i. It is possible to assign different parameter values α_i to each node but in the context of this work, we keep the parameters global, thus $\alpha_i \equiv \alpha$. Next, the dynamical equation is modified by

a coupling term which is governed by the links in the network. Depending on the system $f(u;\alpha)$ that is used, different choices for the coupling term are appropriate. Common choices are coupling terms described by the adjacency matrix (2.1)

$$\dot{u}_i = f(u_i;\alpha) + C\sum_{j=1}^{N}(\mathcal{A}_{ij}u_j) \tag{2.6}$$

or the Laplacian matrix (2.3)

$$\begin{aligned}\dot{u}_i &= f(u_i;\alpha) + C\sum_{j=1}^{N}(\mathcal{L}_{ij}u_j)\\ &= f(u_i;\alpha) + C\sum_{j=1}^{N}(\mathcal{A}_{ij}u_j - u_i)\ ,\end{aligned} \tag{2.7}$$

where $C \in \mathbb{R}^{m\times m}$ is the (global) *coupling matrix*, it determines how the components of the local dynamics (2.5) exert influence on each other. The coupling type (2.7) is also referred to as *diffusive coupling*. In some sense, diffusive coupling can be regarded as natural, as nodes in the same dynamical state do not influence each other and, for modeling concentrations, fluxes will be from high to low concentration. In the case of discrete lattice networks, the coupling (2.7) is the discretization of the diffusion operator. If the network in question is weighted, both types of couplings can also be adjusted by the link weights.

In general, $U \equiv \{u_i\}$ is a dynamical system itself. Its properties are determined by the local dynamics (2.5), by the network topology and by the coupling matrix C. A major task in the study of dynamics on complex networks is to separate these influences. Sometimes, depending on the type of solution studied, this is possible by analytic techniques like e.g. the master stability function approach [49, 17], which we use (in a simple variant) in Sec. 3.3. In many cases, however, this is not easily achievable analytically and numerical techniques become the appropriate choice.

2.2 Network measures

Network measures are numbers that can be calculated for a complex network and give information about a certain aspect of the topology. Many different

measures exist, even for the same property. We give a short account on those mesasures that we need later on. For simplicity, we consider only undirected, unweighted networks.

2.2.1 Clustering

The *clustering coefficient* addresses the question how the neighbors of a particular node relate to each other. If there is a high local cohesion in the graph, neighbors of one node tend to be neighbors to each other as well. There are two slightly differing definitions of the clustering coefficient. The first one is given by the fraction of node triples that are triangles at the same time.

$$C^{(1)} \equiv \frac{3 \times \#\text{ of triangle subgraphs in the graph}}{\#\text{ of connected triples in the graph}} \,. \tag{2.8}$$

Another definition has been introduced by Watts and Strogatz in [32]. For this, one first defines the local clustering coefficient

$$c_i \equiv \frac{\sum_{j,m=1}^{N} (\mathcal{A}_{ij}\mathcal{A}_{jm}\mathcal{A}_{mi})}{k_i(k_i-1)} = \frac{\#\text{ of triangles containing } i}{\#\text{ of triples connected to } i} \,,$$

which yields the global clustering coefficient

$$C^{(2)} \equiv \bar{c} = \frac{1}{N}\sum_{i=1}^{N} c_i \,. \tag{2.9}$$

For both clustering coefficients $0 \leq C \leq 1$ holds, but they are not equal in general. For a good account on the differences between the two, we refer to [20].

2.2.2 Shortest paths

The shortest path from a node i to node j is the smallest sequence of links in $\mathfrak{L}$ that leads from node i to node j. The lengths of shortest paths for all pairs of nodes can be written into a matrix $\{d_{ij}\}$. Then, a typical measure used to characterize a network is the *average shortest path length*

$$l \equiv \frac{1}{N(N-1)} \sum_{i,j=1}^{N} d_{ij} \,. \tag{2.10}$$

By convention, $d_{ij} = \infty$ if there is no path between nodes i and j. Thus $l \in [0, \infty) \cup \{\infty\}$, diverging, as soon as the network has disconnected components. There are several ways to overcome this difficulty, as to limit the summation to pairs of nodes that are connected or to calculate the average of d_{ij}^{-1}. In the remaining chapters, however, we will only be concerned with connected networks. The length of the longest shortest path is called the *Diameter* of the network, given by $\mathrm{Diam}(G) = \max\{d_{ij}\}$. For a more detailed account on shortest path measures, we refer to [19, 20].

2.3 Network models

Network models are used to construct networks that have certain properties. Usually, they exist as a number of rules on how to construct the topology or how to modify the topology of a given network. All network models introduced here are undirected and unweighted.

2.3.1 Regular lattices

In the context of networks, 'regular' means $k_i = k \ \forall i \in \mathfrak{N}$. Regular lattices are networks with the most regular structure, embedded in a Euclidean space $\mathbb{R}^n$, $n \in \mathbb{N}$, they provide a regular tiling. A one-dimensional regular lattice is usually called a *chain*. If this chain is finite and closed, it is called a regular *ring*.

We will be concerned with (modifications of) regular rings mostly. In a regular ring, one node can be connected to more than one node in its vicinity (in euclidean space). The number of neighbors (in the network sense) divided by two is called the *nearest neighbor number* or *coupling range* and is denoted by R. The adjacency matrix of a regular ring can be expressed as

$$\mathcal{A}_{ij} = \sum_{m=1}^{R} \left(\delta_{ij+m} + \delta_{ij-m}\right) . \tag{2.11}$$

Regular ring networks are very well connected locally and the two clustering coefficients coincide. $C^{(2)}$ can be easily calculated (assuming $N > 3R$) by

counting the edges in the subgraph of neighbors of node i and using Eq. (2.9).

$$C^{(2)} = \frac{3}{4}\left(\frac{2R-2}{2R-1}\right) .$$

If $R \geq N/3$, additional links become introduced into this subgraph, $C^{(2)}$ increases above $3/4$ and becomes 1 for $R = N/2$, because then there is a link between every pair of nodes.

On the other hand, two nodes on opposite sides of the ring can only be reached by a long sequence of links. For a regular ring, average path length and diameter can easily be calculated

$$l = \frac{N}{4R} , \qquad \mathrm{Diam}(G) = \frac{N}{2R} .$$

In a general network, there is no notion of space in the sense of allowing a Galilean-like tranformation. Because of the regular structure, a ring network can provide this notion by the natural embedding into euclidean space (resp. S^1) and discrete rotations.

2.3.2 Regular tree networks

A connected network that has no cycles (paths leading back to the same node where every link in the path is only visited once) is called a *tree*. Nodes in a tree that have degree $k = 1$ are called *leaves*.

If all nodes have the same degree k, one speaks of a *regular tree*. For $k > 1$, this only works if the graph is infinitely large, because for $k > 1$ and finite N, leaves have to exist in order to avoid cycles. In the context of this work we somewhat loosen the definition and call a tree a regular tree if all nodes except leaves have the same degree. The number $k - 1$ is called the *branching ratio* of a regular tree.

In a tree, a node can be assigned as the *root* node. This provides an orientation towards and away from the root as well as an ordering of the nodes by the distance to the root node. All nodes that are at the same distance to the root node constitute a *shell*. There is no natural choice for a root node, choosing a different node in a finite regular tree just changes the distances to the leaves and an infinitely extended regular tree looks exactly the same regardless of which node is chosen as the root node. Examples for a regular tree network and for a real-world tree network are shown in Fig. 2.1.

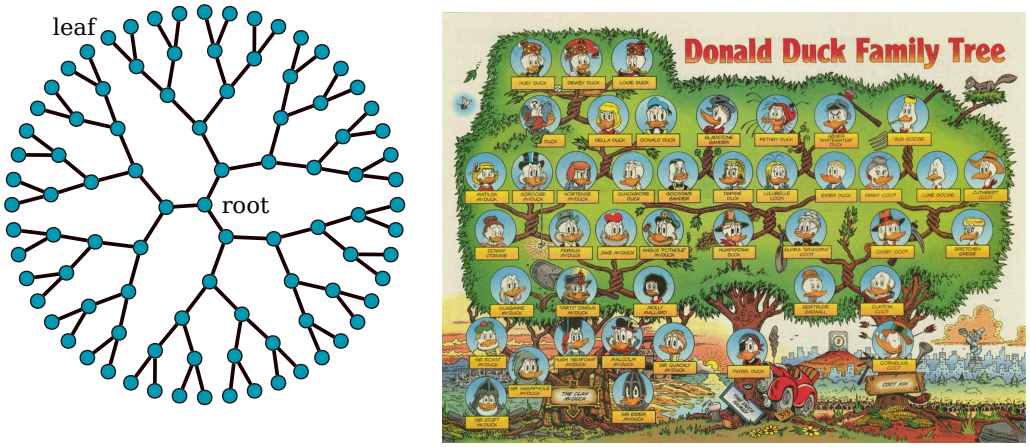

(a) (b)

Figure 2.1: (a) A regular tree network with branching factor 2 (degree of non-leaf nodes $k = 3$). The picture is arranged such that from the chosen root node every leave has the same distance. (b) A real-life tree network taken from [50].

2.3.3 Random networks

Erdős and Rényi proposed and investigated a simple model to generate a complex network [51, 52]. In this model, N unconnected nodes are taken and every pair of nodes is connected with probability p. A network constructed this way has an average degree $\langle k \rangle = pN$.

When taking the limit $N \to \infty$, $\langle k \rangle$ is held constant. In the ensemble of graphs defined this way, there occurs a transition at $\langle k \rangle = 1$. For $\langle k \rangle < 1$, the graph consists of many small unconnected components with finite mean size. For $\langle k \rangle > 1$, almost all nodes belong to a large so-called giant-component which is of order $\mathcal{O}(N)$. For $\langle k \rangle = 1$, the largest component in the graph is of order $\mathcal{O}(N^{2/3})$ [19].

In the limit of large N, the average shortest path length in an Erdős-Rényi random graph is given by $l = \log N / \log \langle k \rangle$ [32]. Since the probability for a link between two nodes is p and does not depend on whether these nodes share a common neighbor, we have $C^{(2)} = p \to 0$ in the limit of $N \to \infty$ [32]. By the same argument, the probability that a fixed node is part of a cycle of length m tends to zero in the limit of large N (and constant $\langle k \rangle$). Thus, for a random graph, all nodes up to distance m of a fixed node become increasingly likely to resemble a tree with the fixed node as the root in the limit of large N.

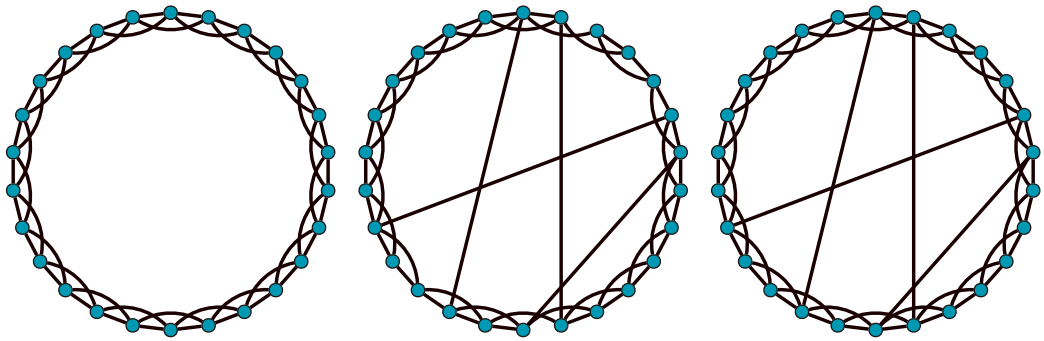

(a) (b) (c)

Figure 2.2: (a) Regular Ring network with $N = 26$, $R = 2$. (b) Watts-Strogatz small-world based on (a) with $n = 4$ rewired links. (c) Newman-Watts small-world based on (a) with $n = 4$ added links.

2.3.4 Small-world networks

In a famous experiment, Milgram [53] demonstrated that in real-life social networks, arbitrarily chosen persons are connected by paths of an average length of only six. This and the fact that in those networks most connections are between individuals that are geographically close to each other led to the terminology of a *small-world* network for a network that has a high clustering coefficient and small average path length.

While in random networks, the average path length scales with $\log N$, the clustering coefficient goes to zero in the limit of large N, see Sec. 2.3.3. In contrast to that are regular lattices, where the clustering coefficient is independent of the system size, but the average path length scales with N, see Sec. 2.3.1. Watts and Strogatz [32] proposed a model that interpolates between these two extremes by randomly rewiring links in a regular ring with a probability p. They showed that for some range of p, the obtained network shows a small average path length (scaling with $\log N$ if $p \gg 1/(2NR)$ [31]), while the clustering coefficient is nearly unchanged. With that they obtained a network model which combines the two above features, a behavior which was only known from real-life networks up to that point.

Newman and Watts [31] (and independently Monasson [54]) proposed a slight variant of this new model in which the links are not rewired but added to the regular lattice with some fixed probability p. The overall behavior is

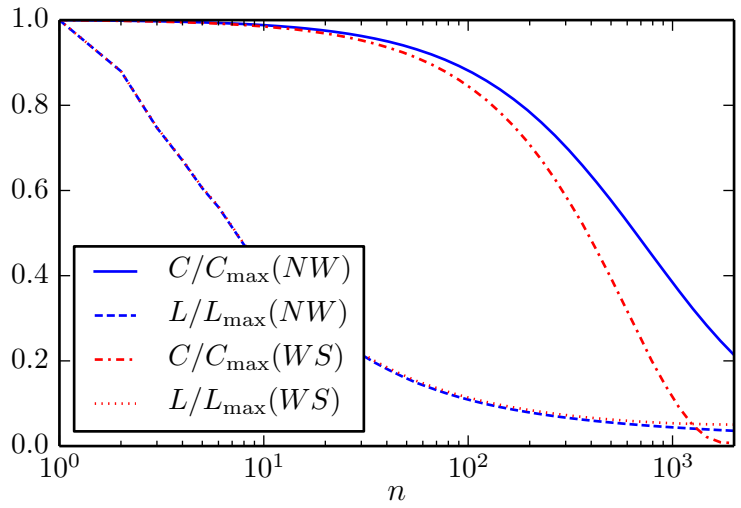

Figure 2.3: Behavior of clustering coefficient $C^{(2)}$ and average shortest path length l vs. number n of added/rewired links for the Newman-Watts (NW, blue, solid and dashed) and Watts-Strogatz (WS, red, dash-dotted and dotted) small-world network models. The base network is a regular ring with $N = 1000$, $R = 2$ and an average over 200 realizations has been performed for every n.

the same, but the latter is easier to handle in analytic studies. Moreover, adding links in contrast to rewiring, where local links are deleted, does not have an influence on the local structure and thus in some sense preserves the notion of space that a regular lattice provides. This is the reason, why in our studies of excitation waves on small-world networks (Chaps. 6 and 7) we use the Newman-Watts model of a small-world network. We further adopt the slight modification that we parameterize the ensembles of Newman-Watts small-world networks by the *number* n of added edges instead of the *probability* p. The network properties of both Watts-Strogatz and Newman-Watts small-worlds have been extensively studied in the literature [31, 55, 56] and they are popular in modeling real-world systems and as a generic topology for dynamical systems on networks [57, 58, 59, 60]. A schematic picture of both models is shown in Fig. 2.2 and the behavior of $C^{(2)}$ and l are visualized in Fig. 2.3.

Chapter 3

The FitzHugh-Nagumo model

In this chapter we introduce the dynamical system that will serve as a model system for excitability throughout this work. We will discuss in detail its dynamical properties and the mechanism by which it exhibits excitability. Finally, we will discuss the necessary and sufficient conditions in order that this system exhibits a Turing instability.

This chapter is structured as follows: In Sec. 3.1, we review the notion of excitability and explain the different types of excitability. In Sec. 3.2, we introduce the differential equations that are the FitzHugh-Nagumo system, discussing limiting fast subystem in Sec. 3.2.1, slow subsystem in Sec. 3.2.2 and the important canard phenomenon in Sec. 3.2.3. Using these ingredients, we explain the mechanism for the generation of excitability in Sec. 3.2.4. Sec. 3.3 is devoted to calculate the conditions for the Turing instability in a FitzHugh-Nagumo reaction-diffusion system.

3.1 Excitable systems, type-I and type-II excitability

Excitability is a property that dynamical systems with a stable steady state can exhibit. Initial conditions close enough to this stable steady state will decay back to it directly, one speaks of *sub-threshold* excitation When initial conditions above a certain threshold are chosen, the system will perform a large-amplitude excursion before returning to the stable steady state. Typically the amplitude in reaction to such a *super-threshold* perturbation is at

least one order of magnitude larger than the distance between threshold and stable steady state. All excitable systems can also act as oscillators when the parameters of the system are changed over a certain bifurcation value into the oscillating regime.

Although neurons are not the only excitable system in the physical world, they are the most prominent and well studied example. In 1948, Hodgkin performed experiments on axons of carcinus maenas (the common shore crab), investigating their behavior when brought into the oscillating regime by a stimulating current [61]. He found that oscillating neurons can be divided into two major classes. Type-I neurons can oscillate at arbitrarily low frequencies, the frequency depends on the strength of the stimulating current and can vary over a large bandwidth. Type-II neurons have a minimum frequency of oscillation. The onset of oscillation happens with that frequency and the bandwidth of achievable frequencies is limited. Hodgkin also identified a third type of neurons which is somewhere between type-I and type-II [62].

In the parameter regime of self-sustained stable oscillations, there is typically no stable steady state (although there are neuron models in which a stable limit cycle and a stable fixed point coexist in a small parameter regime cf. Ref. [63]). In terms of bifurcation theory, the transition to an oscillator can either occur by the stable steady state losing its stability in a supercritical Hopf bifurcation or when the stable steady state vanishes in a saddle-node bifurcation on an invariant circle (SNIC). The saddle-node bifurcation has to be a SNIC because the orbit pertaining to excitation must be connected to the stable steady state. For completeness we want to mention that indirect transitions from excitable to oscillatory behavior via saddle-homoclinic and subsequent saddle-node bifurcation or through a saddle-node of periodic orbits and a subsequent subcritical Hopf-bifurcation showing a coexistence between oscillating and resting behavior in the (small) parameter range between both respective bifurcations exist as well, see [63, 64, 65].

It was pointed out by Rinzel and Ermentrout in 1989 that the SNIC and the Hopf mechanism correspond exactly with both types identified by Hodgkin [66]. The onset of oscillations via a Hopf bifurcation occurs at a finite frequency, whereas at the point of a SNIC bifurcation there is a homoclinic orbit that has infinite period and thus frequency zero. For modeling both types of dynam-

ics, there are prototypical dynamical systems. For type-I, a common choice is the normal form of the SNIC bifurcation (also called SNIPer for Saddle-Node Infinite Period). For type-II, perhaps the most widely used model is the FitzHugh-Nagumo model [67, 68], which we will introduce in this chapter.

3.2 The FitzHugh-Nagumo system

Richard FitzHugh developed his model in order to separate the abstract property of excitability from the physical basis of ionic currents in the Hodgkin-Huxley model [69]. By reducing the dimensionality of the four-dimensional Hodgkin-Huxley model and reducing the complicated gating functions to one third order polynomial, FitzHugh's model [67] was much easier to simulate on the analog computers he was using (which were at least carport-sized at that time). Shortly after FitzHugh, Jin-Ichi Nagumo developed an equivalent electronic circuit for this model [68] and since that time the equations are known as the FitzHugh-Nagumo equations. Nowadays, the FitzHugh-Nagumo model is arguably one of the best studied models of excitability [70, 71, 72, 73, 74, 75]. Sometimes, this model is also related to as Bonhoeffer-van der Pol model, FitzHugh himself suggested this name. The history of the development of this model is described in more detail in Ref. [76].

The FitzHugh-Nagumo model is given by the following set of equations:

$$\dot{u} = u - \frac{u^3}{3} - v + I \tag{3.1a}$$

$$\dot{v} = \varepsilon(u - \gamma v - \beta)\,, \tag{3.1b}$$

where u and v are called the *activator* and *inhibitor* variables and $0 \leq \gamma$, $0 < \varepsilon \ll 1$ and β are parameters. β is called the *threshold* parameter and ε is called the *timescale separation* parameter respectively. The parameter γ is needed to model neuron properties as excitation block [63]. We only need the basic properties of type-II excitability and thus we set $\gamma = 0$ throughout the remainder of this work. The parameter I is an input current used for stimulation of the neuron model. In its place we will have coupling terms later on in order to model input from other elements. The excitability properties of Eqs. (3.1) can be studied with $I = 0$ in dependence on the initial conditions.

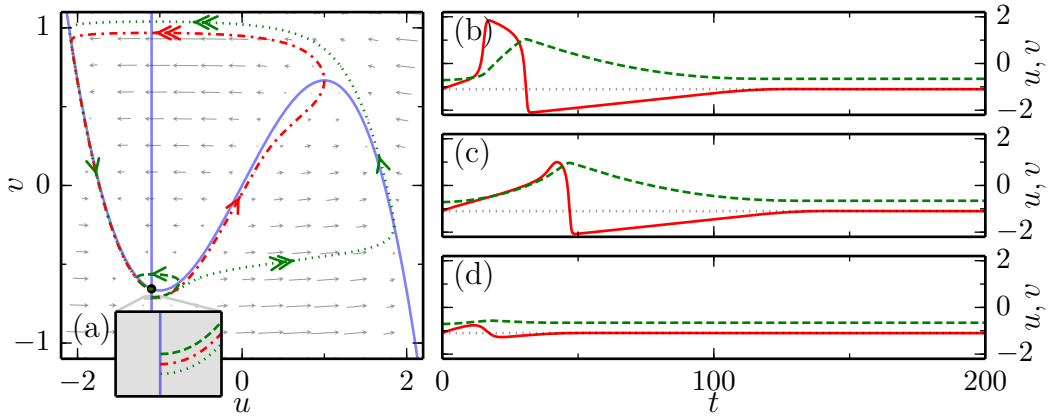

Figure 3.1: Solutions to Eqs. (3.2). (a) Phase portrait (u, v) including vector field (gray arrows), nullclines (blue solid), a sub-threshold solution (green dashed), a super-threshold solution (green dotted) and the canard trajectory that serves as threshold trajectory (red dash-dotted). (b)-(d) u (red solid) and v (green dashed) vs. time t for (b) super-threshold, (c) canard and (d) sub-threshold trajectories. Parameters: $\beta = -1.1$, $\varepsilon = 0.04$.

Thus the model we are using in this work reads

$$\dot{u} = u - \frac{u^3}{3} - v \tag{3.2a}$$

$$\dot{v} = \varepsilon(u - \beta)\,. \tag{3.2b}$$

A picture of the phase-plane of this system is shown in Fig. 3.1. The u and v nullclines are given in blue, with the u-nullcline being the cubic one. The steady state at

$$u_0 = \beta\,, \qquad\qquad v_0 = \beta - \beta^3/3 \tag{3.3}$$

is stable for $|\beta| > 1$ and unstable for $|\beta| < 1$. At $\beta = \pm 1$, the system undergoes a supercritical Hopf bifurcation. The Jacobian J of the right-hand side of the system at the steady state is given by

$$J = \begin{pmatrix} 1 - \beta^2 & -1 \\ \varepsilon & 0 \end{pmatrix}\,,$$

which for $\beta = \pm 1$ has eigenvalues $\pm i\sqrt{\varepsilon}$. Thus, the onset of oscillations at the Hopf bifurcation point happens with a frequency $\sqrt{\varepsilon}$. Looking at Fig. 3.2(a), the magnitude of the oscillation seems not to have the typical square root

shaped behavior, it rather seems to go to a maximum value right away. This is partially true, as the typical Hopf behavior occurs only in a tiny parameter range close to the Hopf bifurcation, see Fig. 3.2(b). After that, the behavior is dominated by the so-called *canard* phenomenon or canard explosion which is a consequence of the timescale separation [63] and will be explained in Sec. 3.2.3.

The Hopf bifurcation at $\beta = \pm 1$ defines the oscillatory behavior of Eqs. (3.2) as type-II. For the system being excitable, however, the timescale separation and the canard phenomenon is vital. In the (u, v)-plane for Eqs. (3.2), Fig. 3.1(a), changes in the u direction (horizontal) happen fast, whereas changes in the v direction (vertical) happen slowly. The combination of both timescales results in Eqs. (3.2) exhibiting excitable behavior in accord with the definition given at the beginning of Sec. 3.1. This is described in more detail in Sec. 3.2.4.

If the transformation $t \to \tilde{t} = \varepsilon t$ is applied, Eqs. (3.2) become

$$\varepsilon \dot{u} = u - \frac{u^3}{3} - v \tag{3.4a}$$

$$\dot{v} = (u - \beta)\,, \tag{3.4b}$$

where the derivative is now with respect to $\tilde{t}$. Eqs. (3.2) are also called *fast system* and Eqs. (3.4) are called *slow system*. Units of time are given by the changes of fast or slow dynamical variable. For $\varepsilon \neq 0$, both formulations are equivalent [77]. To make the effects of timescale separation clearer it is helpful to study both the slow and the fast system in the limit $\varepsilon \to 0$. Fenichel's theorems [78, 77] guarantee that the objects obtained in this limit perturb smoothly when ε is finite but small.

In the following, we will discuss in detail the fast and slow subsystem as well as the canard phenomenon. Finally, we will explain the mechanism that generates excitability in the FitzHugh-Nagumo system.

3.2.1 Fast subsystem

Considering Eqs. (3.2) in the limit $\varepsilon \to 0$ yields:

$$\dot{u} = u - \frac{u^3}{3} - v \tag{3.5a}$$

$$\dot{v} = 0\,. \tag{3.5b}$$

The second equation renders v constant, thus this is a one-dimensional dynamical system with dynamical variable u and parameter v. It is also called the Schlögl model [79, 13]. The system undergoes saddle-node bifurcations at $v = \pm 2/3$ and either has a single stable steady state ($|v| > 2/3$) or two stable steady states ($|v| < 2/3$) separated by an unstable one.

In the phase plane Fig. 3.1(a), the fast subsystem can be visualized by drawing a horizontal line at a specific value of v. This horizontal line has one, two or three intersections with the u-nullcline. When there is one, this corresponds to the single stable steady state; when there are three, the outer ones correspond to the stable steady states and the middle one to the unstable steady state. The case of two intersections is the marginal case at which Eqs. (3.5) undergo a saddle node bifurcation. This divides the u-nullcline of Eqs. (3.2) into three parts according to the stability property of the limiting fast system Eqs. (3.5). The outer ones are called the stable part and the middle section is called the unstable part.

The fast system in the limit $\varepsilon \to 0$ can be used to estimate whether a sudden stimulus ($I > 0$ instantaneously applied) will lead to an excitation. Without the stimulus, the system is at rest and $u = u_0$, $v = v_0$, the values of the stable steady state. When the stimulus is applied instantaneously, the system remains at these values, but the u-nullcline is shifted upwards. Drawing the horizontal line at v_0 in order to visualize the fast subsystem with included stimulus, this possibly has just one intersection with the shifted u-nullcline left. If this is the case, the system will go to this steady state of Eqs. (3.5) corresponding to the other stable part of the u nullcline and thus, the stimulus will trigger an excitation.

3.2.2 Slow subsystem

As discussed above, the transition to and from the excited state happens on the fast timescale. When the fast dynamics has happened, u and v move on (or very close to) one of the stable parts of the u-nullcline. Eqs. (3.4) in the limit $\varepsilon \to 0$ can be used to describe this dynamics. They now read

$$0 = u - \frac{u^3}{3} - v \tag{3.6a}$$

$$\dot{v} = (u - \beta)\,. \tag{3.6b}$$

This is an ordinary differential equation with an additional algebraic constraint. Note that the derivative is with respect to $\tilde{t} = \varepsilon t$. Eq. (3.6a) constrains the system to the u-nullcline.

To eliminate the algebraic constraint, we calculate $\dot{v}$ in terms of $\dot{u}$ and u using Eq. (3.6a) and plug the result into Eq. (3.6b), yielding [80]

$$\dot{u} = \frac{u - \beta}{1 - u^2}\,. \tag{3.7}$$

A closed form solution $u(t)$ of the initial value problem to Eq. (3.7) is not known (to our knowledge). However, using separation of variables and subsequent integration of Eq. (3.7), we can calculate the time Δt, the system Eqs. (3.2) takes for going from a value u_1 to a value u_2, on the same part of the u-nullcline, not crossing β.

$$\begin{aligned}\Delta t\Big|_{u_1}^{u_2} = \varepsilon^{-1}\Delta\tilde{t}\Big|_{u_1}^{u_2} &= \varepsilon^{-1}\int_{u_1}^{u_2}\frac{1-u^2}{u-\beta}\mathrm{d}u \\ &= \varepsilon^{-1}\left[(1-\beta^2)\ln(u-\beta) - u\left(\beta + \frac{u}{2}\right)\right]_{u_1}^{u_2}\,.\end{aligned} \tag{3.8}$$

Fenichel showed that for $\varepsilon > 0$ but small, stable and unstable part of the u-nullcline perturb smoothly to stable and unstable parts of the so-called *slow manifold* which are close to the respective parts of the u-nullcline. For analytical approximations see [80, 81].

3.2.3 Canard phenomena

Canards occur in various singularly perturbed systems and have first been studied in Ref. [83]. We want to explain the phenomenon for Eqs. (3.2). The treatment is close to that in [63].

Eqs. (3.2) have a supercritical Hopf bifurcation at $\beta = \pm 1$ but the typical square-root shaped behavior of the amplitude occurs only in a very small range of β. A close-up of the amplitude behavior after the Hopf bifurcation at $\beta = -1$ is shown in Fig. 3.2(b). The square-root shaped behavior is present between $\beta = -1$ and $\beta \approx -0.99536$ (which is the point marked (d)), a parameter interval of $\Delta\beta \approx 4.64\times10^{-3}$. After the point (d), the amplitude becomes large almost instantly, $\Delta\beta \approx 7.77\times10^{-7}$ between the points marked (e) and (i).

The reason for this behavior lies in the timescale separation. Due to the small value of ε, outside the u-nullcline, the vector field $(\dot{u}, \dot{v})$ is almost pre-

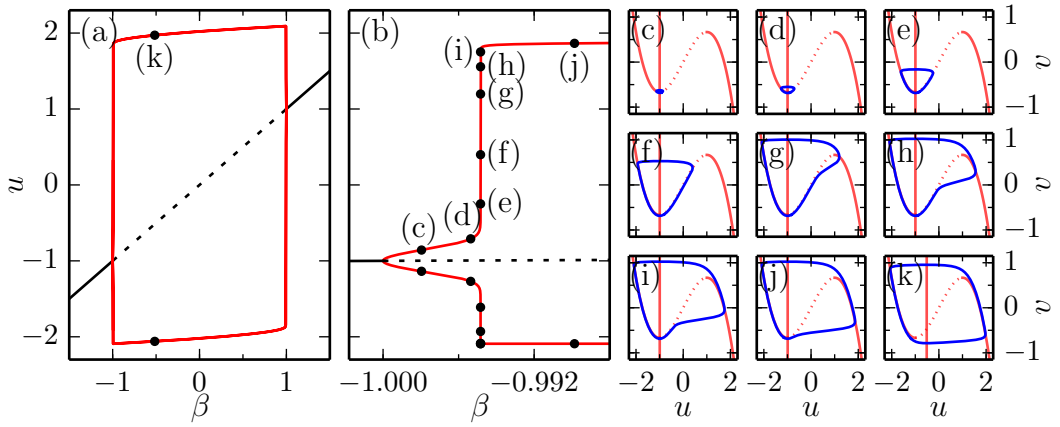

Figure 3.2: Bifurcation diagram of Eqs. (3.2). (a) stable steady state (black solid), unstable steady state (black dashed) , max(u) and min(u) of stable periodic solutions (red solid) vs. β. (b) blow up of (a) behind Hopf bifurcation point at $\beta = -1$ showing canard behavior. (c)-(k) periodic solutions marked in (a) and (b) in the u-v plane (blue) and nullclines of u and v (red). Other parameters: $\varepsilon = 0.04$. The data has been generated using AUTO-07p [82].

cisely directed in the u-direction away from the middle branch of the u-nullcline. This dictates the steps of transition from the small (Hopf) limit cycles (Fig. 3.2(c),(d)) to the large amplitude relaxation oscillator limit cycles (Fig. 3.2(j),(k)).

A point that is exactly on the unstable part of the slow manifold (which is close but not identical to the cubic nullcline) is transported along it by the flow of Eqs. (3.2). Any point that is not exactly on it, however, will jump away from it very fast, going to the left or right stable branch of the u-nullcline. The time spent on the unstable part of the slow manifold is of order $1/\varepsilon$. Thus in order to stay on it, using linear approximation of the fast system, initial conditions need to be specified with a precision of about $\Delta u \approx \exp(-1/\varepsilon)$. For $\varepsilon = 0.04$ as in Fig. 3.2 this means $\Delta u \approx 1.4{\times}10^{-11}$! As the normal Hopf behavior gives an evolution of the amplitude $\Delta u \propto \beta^{1/2}$, we can estimate that within a region of $\Delta\beta \approx \exp(-2/\varepsilon) \approx 3.7{\times}10^{-6}$, the limit cycle will stay on the unstable part of the slow manifold for a considerable amount of time. These are the limit cycle solutions shown in Fig. 3.2(e)-(i). They are called *canard cycles* and the amplitude blow-up in the region of parameter, in which they are present, is called *canard explosion*.

There are also trajectories following the unstable part of the slow manifold when $|\beta| > 1$ and the steady state of Eqs. (3.2) is stable. Because no assumptions about the value of β have been made for the above reasoning, it can be applied to the case where a stable fixed point exists as well. Any trajectory that stays close to the unstable part of the slow manifold for a considerable amount of time is called a *canard trajectory*. In practice, canard trajectories are hard to find because of the required precision in the initial conditions. A good trick to find them is to reverse the direction of time in the computations and starting with initial conditions where a desired canard trajectory should end. A common choice for the FitzHugh-Nagumo equations is to integrate backwards from the point where stable and unstable branch of the u-nullcline meet. In Fig. 3.1, for the case $\beta = -1.1$, a canard trajectory has been plotted using this method starting from $(u, v) = (1, 2/3)$.

Canard is French for "duck" and the origin for this terminology might lie either in the similarity of appearance of some of the canard limit cycles with a duck in the eyes of the French mathematicians Benoit, Callot et Diener [84] or the term alludes to canards in newspapers because canard trajectories are almost impossible to achieve in real-world systems.

3.2.4 Excitability in the FitzHugh-Nagumo system

We now consider Eq. (3.2) with a value of β shortly before the Hopf bifurcation, so that the steady state is stable without loss of generality, let $\beta < -1$. Depending on the initial conditions, any amplitude in the response of the system can be achieved (usually taking u as the measure for the amplitude). In the literature, this behavior is classified as the absence of all-or-none behavior [85]. It is related to the absence of a sharp threshold in Eqs. (3.2) like, e.g., the stable manifold of a saddle-point would provide for example.

As it has been discussed in the last section, trajectories that result in medium-amplitude excitations lie on the unstable part of the slow manifold and thus follow the unstable part of the u-nullcline closely. Although there is sharp threshold, separating sub-threshold initial conditions from super-threshold ones, the region of initial conditions that lead to such medium-amplitude solutions is too small to be practically relevant (see last section).

FitzHugh has classified three different types of thresholds in neural systems

in Ref. [86] and termed this one "quasi-threshold". A common choice for the quasi-threshold in the FitzHugh-Nagumo system is the (canard) trajectory that goes through the point where stable and unstable part of the u-nullcline meet on the opposite side of the stable steady state. For all practical purposes, initial conditions that are more to the side of the stable fixed point will result in sub-threshold excitations and initial conditions on the other side will result in full super-threshold excitations with the transition region being negligibly small.

A typical sequence in an idealized excitation cycle starting with the system being in the stable steady state can be described as follows. (i) A (sudden) perturbation either changes the initial conditions or (temporally) the position of the quasi-threshold such that the current state of the system is on the other side of the quasi-threshold. (ii) Following the flow in the u-direction, v stays almost constant while u rises to a value on the stable branch of the u-nullcline (fast timescale) (iii) The system moves upwards on the stable branch of the u-nullcline until it meets the unstable branch (slow timescale). (iv) The system jumps back in negative u-direction to the other branch of the stable u-nullcline (fast timescale). (v) The system relaxes into the stable steady state on the stable branch of the u-nullcline (slow timescale). In Fig. 3.1(a), a super-threshold excitation cycle for $\beta = -1.1$ and $\varepsilon = 0.04$ is shown in the (u, v) plane. Parts governed by the fast timescale (ii,iv) are marked by a double arrow whereas those governed by the slow timescale (i,iii) are marked by a single arrow.

The threshold parameter β determines the distance of the stable steady state to the quasi-threshold and thus how much it takes to trigger a super-threshold excitation. In practice, β should be close to the Hopf bifurcation. As discussed, a small value of the timescale separation parameter ε is vital for the system to be excitable. However, a too large separation of timescales is difficult for certain numerical tasks as the fast timescale requires small timesteps and the slow timescale long simulation time which in combination renders the numerics of such problems numerically expensive. Especially for the simulation or continuation of spatially extended systems, where dynamics on both timescales can happen simultaneously at different points in space, the problem can only be partially overcome by using adaptive methods. Thus, ε should be

chosen small but not too small for the sake of feasible numerical computations. We will adopt values of $\beta = -1.1$ and $\varepsilon = 0.04$ as standard values for both parameters in this work.

3.3 The Turing instability in the spatially extended FitzHugh-Nagumo system

In this work we will consider FitzHugh-Nagumo systems that will be coupled in a network topology as described in Sec. 2.1.2. We will solely be concerned with coupling by the Laplacian matrix as in Eq. (2.7). Closely related to the Laplacian coupling on a regular lattice is the coupling of a spatially extended field of FitzHugh-Nagumo systems coupled by the Laplace operator. The connection will be worked out in detail in Sec. 4.2.1. For now it suffices to say that the spectrum of both the Laplacian matrix of an arbitrary undirected network as well as the spectrum of the Laplace operator is contained in $\mathbb{R}_0^-$ (negative real numbers including 0).

As discovered by Turing, coupling a spatially extended system by the Laplace operator can destabilize steady states that are stable for the local dynamics [87]. His seminal work describes this mechanism for pattern formation in spatially extended systems now called *Turing instability* and is considered one of the most influential publications of the 20th century being cited over 4400 times as of today. Turing patterns on complex networks have been studied in Refs.[22, 88, 89, 90].

In the following, we want to determine under which conditions the FitzHugh-Nagumo model given by Eqs. (3.1) shows a Turing instability for $I = 0$. The equations for a spatially extended FitzHugh-Nagumo model coupled by the Laplace operator are

$$\dot{u} = u - \frac{u^3}{3} - v + D_u u_{xx} \tag{3.9a}$$

$$\dot{v} = \varepsilon(u - \beta - \gamma v) + D_v v_{xx}\,, \tag{3.9b}$$

where $D_u, D_v \geq 0$ are the diffusion constants for u and v respectively. The other constants are described in Sec. 3.2. Now, $u = u(t, x)$, $v = v(t, x)$ and u_{xx}, v_{xx} denotes the second derivative with respect to space.

We assume that Eqs. (3.9) without the spatial coupling ($D_u = D_v = 0$) have a homogeneous stable steady at $u(t,x) \equiv u_0$, $v(t,x) \equiv v_0$. We examine small perturbations $\delta U = (\delta u, \delta v)$ of the homogeneous steady state for $D_u, D_v \neq 0$, employing the notations $U = (u, v)$ and $f(u) = u - u^3/3$.

$$U = U_0 + \delta U = U_0 + \int_k \delta_k \mathrm{e}^{ikx} \mathrm{d}k =: U_0 + \int_k (\delta U)_k \mathrm{d}k \,,$$

where δk is the k-th spatial mode of the perturbation obtained by Fourier transformation. Assuming that U is very close to U_0 we find

$$\dot{\delta}_k \approx \left[\begin{pmatrix} f'(u_0) & -1 \\ \varepsilon & -\varepsilon\gamma \end{pmatrix} - k^2 \begin{pmatrix} D_u & 0 \\ 0 & D_v \end{pmatrix} \right] \delta_k =: M_k \delta_k \tag{3.10}$$

Thus, the problem reduces to the question whether the matrix M_k has a positive eigenvalue. We find

$$\mathrm{tr} M_k = \mathrm{tr} M_0 - k^2 (D_u + D_v) < 0 \,,$$

because $D_u, D_v > 0$ and with M_0 being the Jacobian for the local dynamics at the stable steady state we have $\mathrm{tr} M_0 < 0$ because $f'(u_0) = 1 - u_0^2 < 0$ for $|u_0| > 1$. Thus, M_k can have at most one eigenvalue with positive real part and this is the case iff there is a $k \in \mathbb{R}$ such that

$$\begin{aligned} 0 > \det M_k &= \left(f'(u_0) - k^2 D_u\right)\left(-\varepsilon\gamma - k^2 D_v\right) + \varepsilon \\ &= k^4 \underbrace{D_u D_v}_{=:A} - k^2 \underbrace{\left(f'(u_0) D_v - \varepsilon\gamma D_u\right)}_{=:B} + \det M_0 \\ &= k^4 A - k^2 B + \det M_0 \,. \end{aligned} \tag{3.11}$$

This gives $B > 0$ as a necessary condition and thus

$$f'(u_0) D_v > \varepsilon\gamma D_u \,. \tag{3.12}$$

For $\gamma = 0$ we have $u_0 = \beta$, which is stable iff $|\beta| > 1$. Then $f'(u_0) = 1 - \beta^2 < 0$ which violates (3.12), and thus there can be no Turing instability for $\gamma = 0$. However, it has been shown in [11] that Turing instabilities can be induced by nonlocal (cross-species) coupling.

For completeness let us consider the case $\gamma > 0$. As a numerical continuation of the supercritical Hopf bifurcation in the parameters γ and β reveals, the

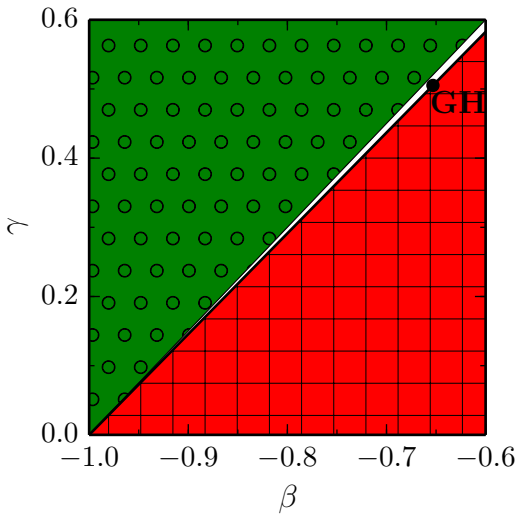

Figure 3.3: Regions of stability of the homogeneous steady state of Eqs. (3.9) in the (β, γ) parameter plane. Green with circles: stable for all values of D_v/D_u. Red hatched: unstable (also for $D_u = D_v = 0$). White: Turing instability is possible if condition (3.13) is satisfied. The border between unstable and Turing region is given by a line of Hopf bifurcations. The border between stable and Turing region is given by $\beta = 2\gamma/3 - 1$. The point GH marks a Bautin (generalized Hopf) bifurcation. Other parameters: $\varepsilon = 0.04$ (diagram does not depend on ε).

u-value of the Hopf bifurcation point becomes larger than -1 for $\gamma > 0$. A short calculation shows that for $\beta = 2/3\gamma - 1$, $u_0 = -1$.

Thus it is possible to find values of γ and β between these two lines for which (u_0, v_0) can be a stable steady state (for $D_u = D_v = 0$) with $|u_0| < 1$ and thus $f'(u_0) > 0$. A scan of the parameter plane (β, γ) shows that this region is very small (see Fig. 3.3). In conclusion, choosing $D_v/D_u > \varepsilon\gamma/f'(u_0)$ will satisfy condition (3.12).

The right-hand side of condition (3.11) has a local minimum at $k^2 = B/2A$. The value of this local minimum is given by $\min_k(\det M_k) = -B^2/4A + \det M_0$. Thus, the necessary and sufficient condition for (3.11) is

$$\det M_0 < \frac{B^2}{4A},$$

as both sides are positive

$$\sqrt{\det M_0} < \frac{B}{2\sqrt{A}}$$
$$\Rightarrow \quad 2\sqrt{\det M_0} < f'(u_0)\sqrt{\frac{D_v}{D_u}} - \varepsilon\gamma\sqrt{\frac{D_u}{D_v}}$$

thus finally

$$\sqrt{\frac{D_v}{D_u}} > \frac{1}{f'(u_0)}\left(\sqrt{\det M_0} + \sqrt{\det M_0 + \varepsilon\gamma f'(u_0)}\right) . \tag{3.13}$$

Conditions (3.12) and (3.13) are compatible, as both result in infimum values for D_v/D_u.

The calculation also holds for units of FitzHugh-Nagumo systems coupled by the Laplacian matrix of a network as in Eq. (2.7). One simply replaces the $-k^2$ and the k^4 in Eq. (3.11) with Λ_k and Λ_k^2 respectively, where Λ_k are the eigenvalues of the Laplacian, indexed by k. Because $\Lambda_k \leq 0$, the entire calculation holds one-to-one for this case, giving the same conditions for a destabilization of the homogeneous steady state on a complex network. In the complex network case, these conditions are not sufficient, however, because there might be no eigenvalues of the Laplacian in the region where $\det M_k$ could become negative.

Chapter 4

Excitation waves on a discrete lattice and in the continuum limit

In this chapter, we will present the basic theme whose variations will be at the core of this work. We will give a presentation of the behavior of excitation waves in the FitzHugh-Nagumo model on a one-dimensional regular lattice. Varying the global coupling strength, different dynamical regimes will be dominant. The limit of very small and very large coupling strengths will be discussed as well as the influence of the coupling range R.

Modifications of the regular lattice and their influence on the dynamics of traveling excitation waves will be studied in the following three chapters. These are tree networks in Chapter 5, minimal small-world networks (regular rings with one additional long-range link) in Chapter 6 and Newman-Watts small-world networks in Chapter 7.

This chapter is structured as follows: Firstly in Sec. 4.1, we will briefly review waves in a continuous one-dimensional FitzHugh-Nagumo reaction-diffusion system as this is an important limiting case. In that section we will also discuss the basic techniques with which the dispersion relation (Sec. 4.1.1) and the stability (Sec. 4.1.2) for traveling waves can be calculated. In Sec. 4.2, we will consider the one-dimensional regular ring network of FitzHugh-Nagumo units. We will discuss the two limiting cases of high coupling strength (Sec. 4.2.1) and low coupling strength (Sec. 4.2.2). In Sec. 4.2.3, we will present a summarizing dispersion relation for excitation waves on this network.

4.1 Waves in a FitzHugh-Nagumo reaction-diffusion system

We will consider a one-dimensional FitzHugh-Nagumo reaction-diffusion system obeying the following equations:

$$\dot{u} = u - \frac{u^3}{3} - v + u_{xx} \tag{4.1a}$$

$$\dot{v} = \varepsilon(u - \beta)\,, \tag{4.1b}$$

where $u(t,x)$, $v(t,x)$ both are spatially extended fields of activator and inhibitor respectively. The dot ($\dot{u}$) marks the derivative with respect to time t and u_{xx} the second derivative of u with respect to space x. The system is spatially coupled by a diffusion term in the activator variable only, mimicking the injected current of Eq. (3.1a) which is classically used in the FitzHugh-Nagumo model to trigger excitations. Any constant $D > 0$ multiplying the diffusion term can be scaled to unity by a rescaling of the space variable $x \to (1/\sqrt{D})x$. If the parameters of the dynamics (without the diffusion term) are in the regime of excitability (cf. Sec. 3.2.4), a setup like this is also called an *excitable medium*.

From Sec. 3.3, we conclude that no Turing instability is possible for Eqs. (4.1) as this would require both a nonzero coupling to the inhibitor in Eq. (4.1b) as in Eqs. (3.9) ($\gamma > 0$) and a (large) diffusion term for the inhibitor field v. Apart from the stable homogeneous steady state, stable traveling wave solutions exist (see e.g. [36]). Traveling waves are non-uniform solutions that are given by $u(t,x) = \tilde{u}(x - ct)$ and $v(t,x) = \tilde{v}(x - ct)$, where $\tilde{u}$, $\tilde{v}$ are called the wave *profile*. Traveling waves are localized excitations that travel through the medium at uniform speed c without changing shape thus they are stationary in a co-moving frame (see Sec. 4.1.1). A special case of (periodic) traveling waves are traveling pulses, which are traveling waves with $\lim_{x-ct\to\pm\infty} \tilde{u} = u_0$ and $\lim_{x-ct\to\pm\infty} \tilde{v} = v_0$. A traveling pulse that consists of just one excitation is called *singular*. Waves in an infinitely extended medium with infinitely many equidistant excitations are called *wave trains*. They are equivalent (except for stability properties) to waves in a finite medium with periodic boundary conditions.

4.1.1 Dispersion relation

The speed c of a traveling wave is dependent on the spatial extension of the medium, on the boundary conditions and on the type of wave. We consider two cases of boundary conditions: (i) periodic boundary conditions $x \in [0, L]$ and $u(t, 0) = u(t, L)$, $v(t, 0) = v(t, L)$ and (ii) infinitely extended medium $x \in \mathbb{R}$.

By using the spatio-temporal symmetry $u(x, t) = \tilde{u}(x - ct)$ of the solution, and defining the comoving frame coordinate $\xi := x - ct$, we can reduce the partial differential equation system (4.1) to a system of ordinary differential equations for the profiles. For the derivatives with respect to t and x, we have

Written as a first-order system and using

$$\dot{u}(x, t) = -c\tilde{u}' , \qquad u_{xx} = \tilde{u}'' ,$$

this reads (dropping the tilde)

$$u' = w \tag{4.2a}$$

$$v' = -\frac{\varepsilon}{c}(u - \beta) \tag{4.2b}$$

$$w' = -cw - \left(u - \frac{u^3}{3} - v \right) , \tag{4.2c}$$

where u', v', w' denote the derivatives with respect to ξ.

The stable homogeneous steady state (u_0, v_0) of Eqs. (4.1) appears as an (unstable if ξ is considered as 'time') steady state $(u_0, v_0, 0)$ of Eqs. (4.2). Wave train solutions on an infinitely extended medium and waves on a medium with periodic boundary conditions appear as periodic solutions of Eqs. (4.2). The periodic solution is required to have period $T = L$ (the distance between wave peaks or the extension of the medium respectively). This requirement fixes the additional free parameter c in Eqs. (4.2). Singular pulses on an infinitely extended medium appear as a homoclinic solution to the steady state $(u_0, v_0, 0)$ which appears as the limit of periodic orbits when $T \to \infty$. The parameter c takes a finite value in this limit.

For a given L, there can be multiple values c for which periodic orbits with period L exist for Eqs. (4.2). The relation of $c(L)$ is commonly called *dispersion relation*. A picture of the dispersion relation is shown in Fig. 4.1(DR) together with selected stable and unstable solutions, marked (A)-(D) and (a)-(d), respectively. Detailed information about the dispersion relation of wave trains in excitable media is found in [91, 92, 93].

The change of the wave profile for the stable solutions can be described in the following way: For large L, the stable profiles have the same shape to very good approximation (see Fig. 4.1(D) and (C)). The transitions from resting to excited (in u) are relatively steep. The difference between the profiles is the length of the interval of ξ that is spent at (or rather very close to) the steady state. Also, the propagation speed c does not change significantly with L and c attained by solution (D) is almost identical to the speed at $L \to \infty$. If L decreases, the transitions between rest and excited state become less steep and the inhibitor level v becomes more elevated throughout the entire profile. This is visible in Fig. 4.1(A), (B), (Aa) and (Bb), where the closed solid blue curve is significantly shifted to higher v values (especially visible in (Aa)). For the unstable (with respect to t) solutions, the amplitude of the profile is diminished very strongly and the shape barely changes, only the amount of ξ at (or very close to) the steady state differs, see Fig. 4.1(a)-(d). A very rigorous mathematical account on the stable and unstable waves profiles in the FitzHugh-Nagumo reaction-diffusion system, using singular perturbation theory is found in Ref. [73].

4.1.2 Calculation of spectra and stability

The stability of traveling waves as solutions to Eqs. (4.1) cannot be inferred from the linearization of Eqs. (4.2) around the corresponding profile solutions. This does always have characteristic multipliers with modulus greater than one even though the corresponding traveling wave can be stable.

The stability of traveling waves obeying Eqs. (4.1) can be assessed using a technique combining Bloch wave decomposition and numerical continuation, described in detail in Ref. [94]. Since this technique will become important in Secs. 5.2.1 and 7.2, we want to give a short outline.

Assume that $U_{\mathrm{tw}}(\xi) = U_{\mathrm{tw}}(x - ct)$ is the profile of a wave train solution with spatial period L, satisfying the equation

$$\dot{U} = F(U) + DU_{xx}\,, \tag{4.3}$$

where D is the (constant) coupling matrix describing the influence of the components of U on each other. Note that $U_{\mathrm{tw}}(\xi)$ is L-periodic $U_{\mathrm{tw}}(0) = U_{\mathrm{tw}}(L)$. In our case, $U = (u, v)$ and $D = \mathrm{diag}(1, 0)$. With the ansatz $U(t, x) =$

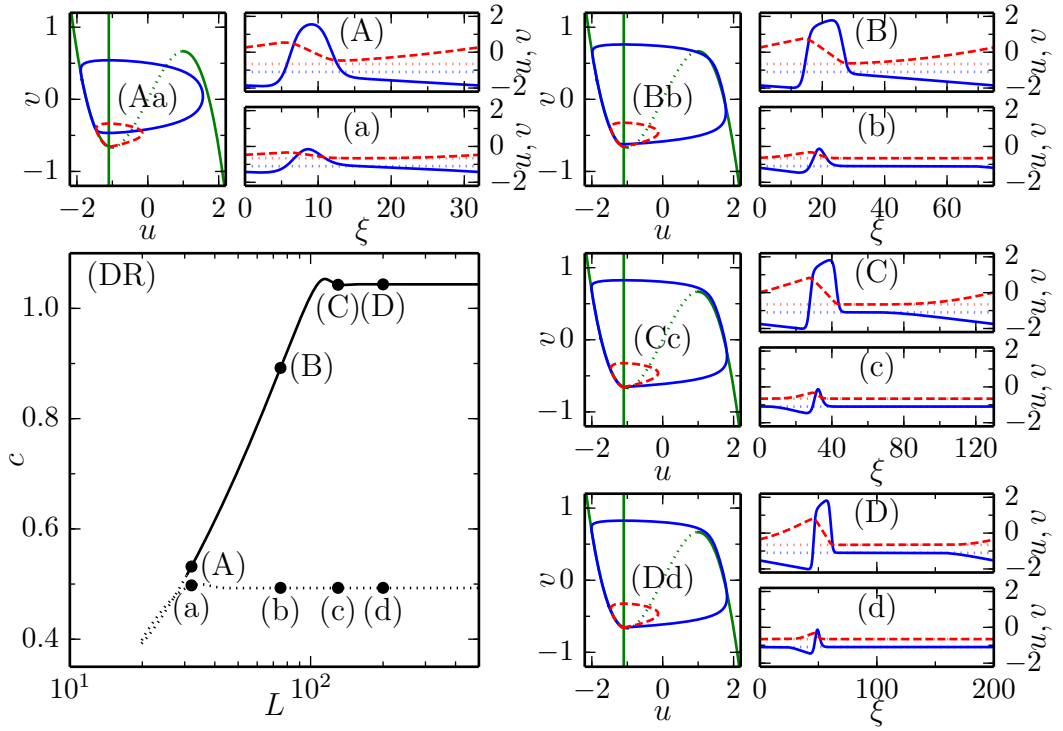

Figure 4.1: Wave solutions in Eqs. (4.1) with periodic boundary conditions, found as periodic solutions to Eqs. (4.2). (DR), Dispersion relation: Branch of stable traveling wave solutions (black solid) and unstable traveling wave solutions (black dotted). Size of domain L vs. propagation speed c. (Aa): Phase portrait (u, v) of exemplary stable (blue, solid) and unstable (red dashed) traveling wave solutions at $L = 32$ together with nullclines (green dotted). (A): u (blue solid) and v (red dashed) vs. comoving frame coordinate ξ for stable solution at $L = 32$, steady state values for u (blue dotted) and v (red dotted). (a): u (blue solid) and v (red dashed) vs. comoving frame coordinate ξ for unstable solution at $L = 32$, steady state values for u (blue dotted) and v (red dotted). (Bb),(B),(b) : Same as (Aa),(A),(a) for $L = 75$. (Cc),(C),(c) : Same as (Aa),(A),(a) for $L = 130$. (Dd),(D),(d) : Same as (Aa),(A),(a) for $L = 200$. Other parameters: $\varepsilon = 0.04$, $\beta = -1.1$. All waves are traveling to the right in Eqs. (4.1). The diagram data has been generated using AUTO-07p [82].

$U_{\mathrm{tw}}(x-ct)+\mathrm{e}^{\lambda t}\delta U(x-ct)$, δU being a small perturbation and $\xi = x-ct$, we obtain

$$\begin{aligned}\dot{U}(t,x) &= \dot{U}_{\mathrm{tw}}(\xi) + \mathrm{e}^{\lambda t}\left[\lambda\delta U(\xi) - c\delta U'(\xi)\right] \\ &= F(U(t,x)) + DU_{xx}(t,x)\,.\end{aligned}$$

Since δU is small, we have

$$\begin{aligned}F(U(t,x)) + DU_{xx}(t,x) &= F(U_{\mathrm{tw}}(\xi) + \mathrm{e}^{\lambda t}\delta U(\xi)) + DU''_{\mathrm{tw}}(\xi) + \mathrm{e}^{\lambda t}\delta U''(\xi) \\ &\approx F(U_{\mathrm{tw}}(\xi)) + DU''_{\mathrm{tw}}(\xi) \\ &\quad + \mathrm{e}^{\lambda t}\left[\partial F\big|_{U_{\mathrm{tw}}(\xi)}\delta U(\xi) + D\delta U''(\xi)\right]\end{aligned}$$

Since $U_{\mathrm{tw}}(\xi)$ satisfies Eq. (4.3), we obtain

$$\begin{aligned}\lambda\delta U(\xi) &= \partial F\big|_{U_{\mathrm{tw}}(\xi)}\delta U(\xi) + c\delta U'(\xi) + D\delta U''(\xi) \\ &=: \mathcal{L}\,\delta U(\xi)\,.\end{aligned} \tag{4.4}$$

In all of the above, ∂F denotes the Jacobian matrix of F, $\dot{(\ )}$ denotes the derivative with respect to time, $(\ )_x$ the derivative with respect to space and $(\ )'$ the derivative with respect to ξ. Eq. (4.4) is the eigenvalue equation for the operator $\mathcal{L}$ defined by the righ-hand side. Since $\partial F\big|_{U_{\mathrm{tw}}(\xi)}$ is L-periodic, Eq. (4.4) is an ordinary differential equation with time periodic coefficients. For this type of equation, as a consequence of Bloch's theorem, the general solution $\delta U(\xi)$ ($\xi \in \mathbb{R}$) is the product of an L-periodic function $P(\xi)$ and a factor $\mathrm{e}^{2\pi i\nu\xi/L}$ or equivalently

$$\delta U(\xi + L) = \mathrm{e}^{2\pi i\nu}\delta U(\xi)\,, \tag{4.5}$$

where ν is the Bloch wavenumber in units of $L/(2\pi)$. The operator $\mathcal{L}$ for an infinitely extended wave train U_{tw} has no isolated eigenvalues [95]. Its spectrum consists of the so-called *essential spectrum* and every eigenvalue λ in the essential spectrum admits a solution satisfying Eqs. (4.4) and (4.5) with some $\nu \in [0,1)$. If the traveling wave, for which the spectrum is calculated is subjected to (ML)-periodic boundary conditions, admitting M wave peaks, those points of the essential spectrum that have $\nu \in \{0, M^{-1}, 2M^{-1}, ..., (M-1)M^{-1}\} \subset [0,1)$ appear as eigenvalues of $\mathcal{L}$. Note that $\delta U = U'_{\mathrm{tw}}$ is always a solution of Eq. (4.4) with $\lambda = 0$. This is the so-called *Goldstone mode*, which reflects the translational symmetry of the problem.

In the case of the FitzHugh-Nagumo reaction-diffusion system, Eq. (4.4) combined with the boundary condition (4.5) defines the following boundary value problem (derived from the linearized system):

$$\delta u' = \delta w \tag{4.6a}$$

$$\delta v' = \frac{1}{c}\left(\lambda\delta v - \varepsilon\delta u\right) \tag{4.6b}$$

$$\delta w' = \lambda\delta u - \left[(1-u_{\mathrm{tw}}^2)\delta u - \delta v\right] - c\delta w \tag{4.6c}$$

$$\delta u(L) = \mathrm{e}^{i2\pi\nu}\delta u(0) \tag{4.6d}$$

$$\delta v(L) = \mathrm{e}^{i2\pi\nu}\delta v(0) \tag{4.6e}$$

$$\delta w(L) = \mathrm{e}^{i2\pi\nu}\delta w(0)\,, \tag{4.6f}$$

where u_{tw} is (the u part of) the profile of a traveling wave solution to Eqs. (4.1) with spatial period L and propagation speed c.

The boundary value problem (4.6) can be used in a numerical continuation software like AUTO-07p to continue the eigenvalue λ the Bloch wavenumber ν and the eigenfunction $(\delta u, \delta v, \delta w)$ for the essential spectrum. In order to start the continuation one eigenvalue and eigenfunction for each connected component of the essential spectrum has to be found (approximately). This can be done by numerically solving the eigenvalue equation (4.4) subjected to periodic boundary conditions using discretization and/or Fourier transformation.

By calculating the essential spectra for wave trains in Eqs. (4.1), we were able to evaluate the stability of traveling waves and other complex changes of the spectrum that occur when going along the branch of traveling wave solutions. The dispersion relation (propagation velocity c vs. domain size L) including the leading parts of the (essential) spectrum for selected points (c)-(k) is illustrated in Fig. 4.2.

Starting with a stable traveling wave profile for large L, the calculated spectrum tell us that a destabilization of the wave occurs at a minimum L value for stable propagation of $L_{\mathrm{min}} \approx 30.756$ by two complex conjugate eigenvalues with nonzero imaginary part. However this point does not yet mark the lowest possible propagation speed c attained by traveling wave solutions. This is attained by the branch of unstable solutions after lowering L further to a value of $L \approx 19.6$. After that, the branch of unstable solutions continues, after undergoing a saddle-node bifurcation, in direction of rising L with the speed

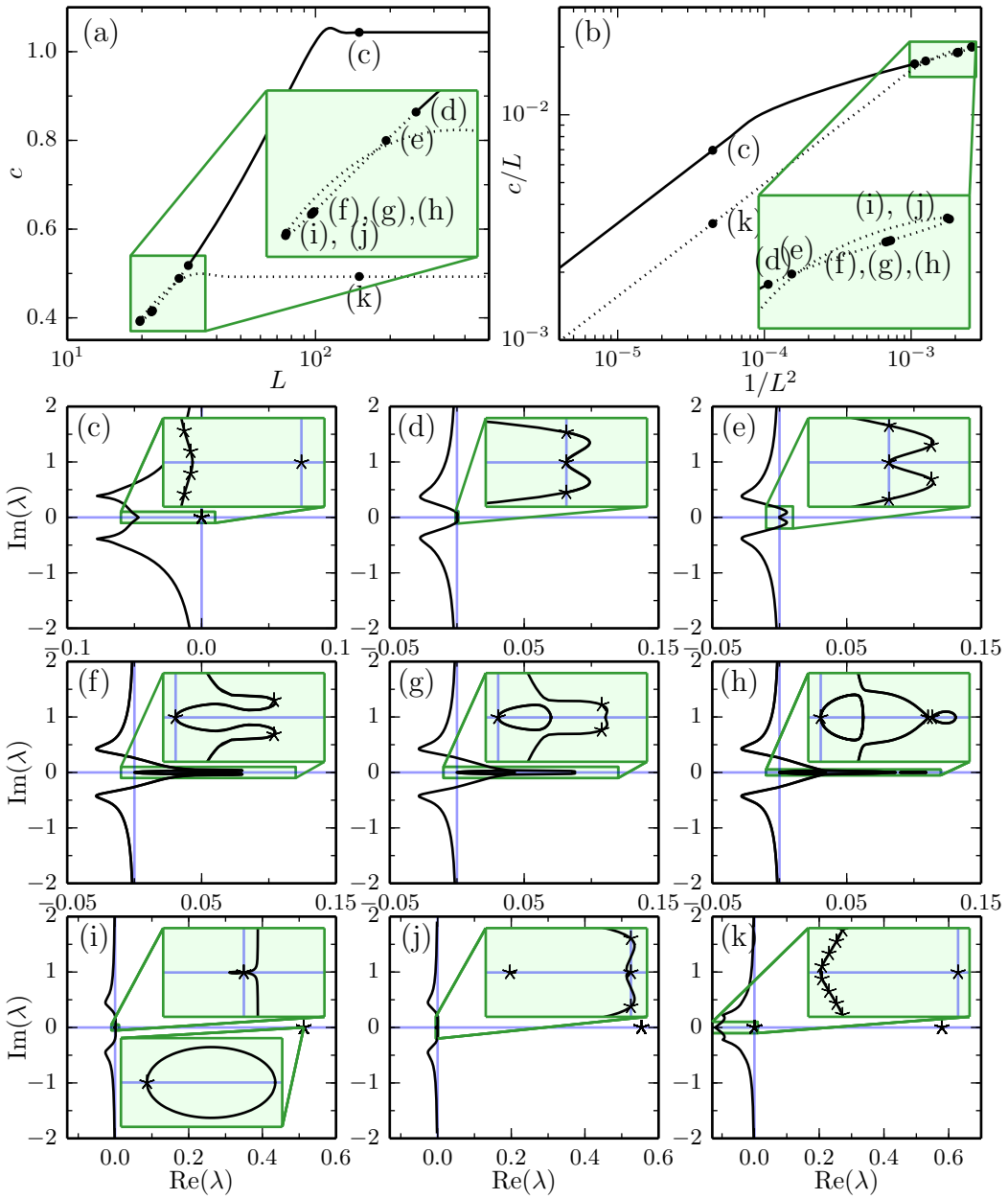

Figure 4.2: Dispersion relation for traveling wave solutions of Eqs. (4.1), including spectra. (a) Dispersion relation of Eqs. (4.1) i.e., propagation velocity c vs. domain size L (see also Fig. 4.1). (b) Same dispersion relation in the transformed coordinates $1/L^2$ and c/L which are more adequate for networks. (c)-(k) Leading part of the essential spectrum for selected points marked in panels (a),(b). The insets in (a), (b) show an enlarged view of the green rectangles, the insets in (c)-(k) show a enlargement of the spectrum near the origin. Those points that are in the spectrum for the system with *periodic* boundary conditions are marked by an asterisk. Parameters: $\beta = -1.1,\ \varepsilon = 0.04$.

converging against $c \approx 0.493$. On this branch, L can increase without bounds, and this branch is associated with the transition to an (unstable) solitary traveling pulse. Also on the stable branch, L can increase without bounds but the solutions do not lose stability and converge to a stable propagating solitary pulse with the propagation speed attaining a value of $c \approx 1.044$.

After the destabilization at $L_{\min}$, the spectrum changes in a complex way, leaving in the end an isolated eigenvalue as the only object in the right half-plane. In the pictures of the spectrum, Fig. 4.2(c)-(k), the essential spectrum is marked by continuous lines and the values of the essential spectrum that occur for L-periodic boundary conditions are marked with asterisks. The latter will be the relevant ones for our model as we will be dealing with systems with periodic boundary conditions. The changes in spectrum at the points (c)-(k) are following the sequence: (c) All eigenvalues are in the left half-plane (except for the one that is always present at zero corresponding to the Goldstone mode of translation invariance), (d) two complex conjugate eigenvalues crossing the imaginary axis at $L_{\min}$, (e) a second pair of complex conjugate eigenvalues crossing the imaginary axis, (f),(g) from the leading part of the essential spectrum, a circle comprising the Goldstone mode eigenvalue forms and detaches, (h) the first two eigenvalues that have crossed the imaginary axis merge on the real axis and split in different directions, (i) one of the eigenvalues that has merged on the real axis crosses zero, (j) the second two eigenvalues that have crossed the imaginary axis cross the imaginary axis again in the opposite direction, (k) one eigenvalue remains in the right half-plane, the rest of the eigenvalues are in the left half-plane (again except for the Goldstone mode eigenvalue at zero). Thus, after the first instability at $L_{\min}$, a scenario with several secondary instabilities evolves.

Note that wave trains would already destabilize at a value of L a bit larger than $L_{\min}$ (before point (d)) because part of the essential spectrum with $\nu \neq 0$ crosses the imaginary axis before the first eigenvalue with $\nu = 0$ does so at $L_{\min}$.

Next, we will discuss the behavior of waves on regular rings. Here, the traveling waves are subject to effects of the inherent discreteness of the system.

4.2 FitzHugh-Nagumo model on a one-dimensional regular ring network

Let us consider identical FitzHugh-Nagumo systems on the nodes of a regular ring network with N nodes and coupling range R. The units are coupled by their diffusive coupling in the activator variable u. This is the coupling scheme from Eq. (2.7). The adjacency matrix for a such a regular ring network is given in Eq. (2.11) The equations for such a system read

$$\dot{u}_i = u_i - \frac{u_i^3}{3} - v_i + D\sum_{m=1}^{R}(u_{i-m} + u_{i+m} - 2u_i) \tag{4.7a}$$

$$\dot{v}_i = \varepsilon(u_i - \beta), \qquad i \in \{1, ..., N\}\,, \tag{4.7b}$$

all indices are to be understood modulo N. $u_i(t)$ and $v_i(t)$ are the activator and inhibitor level on node i, respectively. The parameters of the FitzHugh-Nagumo system ε and β are global, as all units are considered identical. We consider $\varepsilon = 0.04$ and $\beta = -1.1$, putting the local dynamics into the excitable regime. The parameter $D > 0$ defines the strength of the coupling. Again, there can be no Turing stability in the system because the $\dot{v}_i$ does not depend on v ($\gamma = 0$, see Eqs. (3.2)) and there is no coupling in v.

Due to the regular coupling structure on the ring network there is a (discrete) translation invariance in the system, which provides a notion of space that in turn enables us to speak of traveling waves. As there is no rescaling of space possible in this system (without changing the resolution of the discretization), the coupling strength D in Eq. (4.7a) cannot be scaled to 1. Apart from the stable homogeneous steady state there exist travelling wave solutions on this ring network in a certain range of D. Depending on whether D is small or large, those traveling waves have different properties. For large D, Eqs. (4.7) resemble a continuous reaction-diffusion system (in a certain limit). This will be discussed next in Sec. 4.2.1. For small D, the discrete nature of Eqs. (4.7) is dominating, which will be discussed in Sec. 4.2.2. We study wave-like solutions that exhibit exactly one peak on the ring.

4.2.1 High coupling strength – continuum regime

Let us first consider the case where $R = 1$ (nearest neighbor coupling on the ring). We denote the coupling term for node i in Eq. (4.7a) by c_i.

If $R = 1$, we obtain

$$c_i = D(u_{i-1} + u_{i+1} - 2u_i)\,. \tag{4.8}$$

Comparing this to the definition of the second derivative of a function $u(x)$

$$u''(x) = \lim_{h\to 0} \frac{u(x-h) + u(x+h) - 2u(x)}{h^2} \tag{4.9}$$

leads us to the definition $h := 1/\sqrt{D}$, which in turn defines the equivalent spatial distance between two neighboring nodes of the ring network. In conclusion, the ring network has a circumference of $L = N/\sqrt{D}$ and we can define $x := ih$. Therefore, using $u(x) = u(ih) := u_i$, we rewrite Eq. (4.8) as follows

$$c_i = h^{-2}\big[u(x-h) + u(x+h) - 2u(x)\big]\,.$$

Thus, in the limit

$$N \to \infty \tag{4.10a}$$

$$D \to \infty \tag{4.10b}$$

$$\text{with } \frac{N}{\sqrt{D}} = \text{const} =: \tilde{L}\,, \tag{4.10c}$$

we have $c_i \to u''(x)$ and Eqs. (4.7) (for $R = 1$) are equivalent to the one-dimensional reaction-diffusion system with periodic boundary conditions Eqs. (4.1) and domain size $\tilde{L}$.

In general, R can be greater than 1. The limit of the coupling term c_i in that case, using the above definition of $u(x)$ and h, reads

$$\begin{aligned}
\lim_{D\to\infty} c_i &= \lim_{D\to\infty} D \sum_{m=1}^{R} (u_{i-m} + u_{i+m} - 2u_i) \\
&= \lim_{h\to 0} \sum_{m=1}^{R} \frac{u(x-mh) + u(x+mh) - 2u(x)}{h^2} \\
&= \sum_{m=1}^{R} \lim_{h\to 0} \frac{u(x-mh) + u(x+mh) - 2u(x)}{h^2}\,.
\end{aligned}$$

Rescaling $\tilde{h} := mh$ yields

$$\begin{aligned}\lim_{D\to\infty} c_i &= \sum_{m=1}^{R} \lim_{\tilde{h}\to 0} m^2 \frac{u(x-\tilde{h}) + u(x+\tilde{h}) - 2u(x)}{\tilde{h}^2} \\ &= \sum_{m=1}^{R} m^2 u''(x)\,. \end{aligned} \tag{4.11}$$

Defining

$$q(R) := \sum_{m=1}^{R} m^2 = \frac{1}{6} R(R+1)(2R+1)\,, \tag{4.12}$$

we conclude that by rescaling the spatial variable of the limiting reaction-diffusion system as $x \to q(R)^{-1/2} x$, in the limit

$$N \to \infty \tag{4.13a}$$

$$D \to \infty \tag{4.13b}$$

$$\text{with } \frac{N}{\sqrt{Dq(R)}} = \text{const} =: L\,, \tag{4.13c}$$

Eqs. (4.7) are equivalent to the one-dimensional reaction-diffusion system with periodic boundary conditions Eqs. (4.1) and domain size L. Note that for $q(R = 1) = 1$ and thus the lengths in the limits (4.13c) and (4.10c) are identical.

Summarizing, if N and D in Eq. (4.7) are large enough, the system behaves like the reaction-diffusion system (4.1) (with domain size L and periodic boundary conditions). If N is fixed and D is increased, the 'virtual' length L of the ring decreases. In Sec. 4.1.2, we have shown that there is a minimum length $L_{\min}$ for stable propagation of waves. This $L_{\min}$ gives

$$D_{\max} = \frac{N^2}{L_{\min}^2 q(R)} \tag{4.14}$$

as a maximum coupling strength for stable wave propagation on a regular ring network with N nodes and coupling range R.

4.2.2 Low coupling strength – discrete regime

If D is large, the part of the wave that is transitioning from rest to excited state (the leading front) typically occupies more than one node at a time.

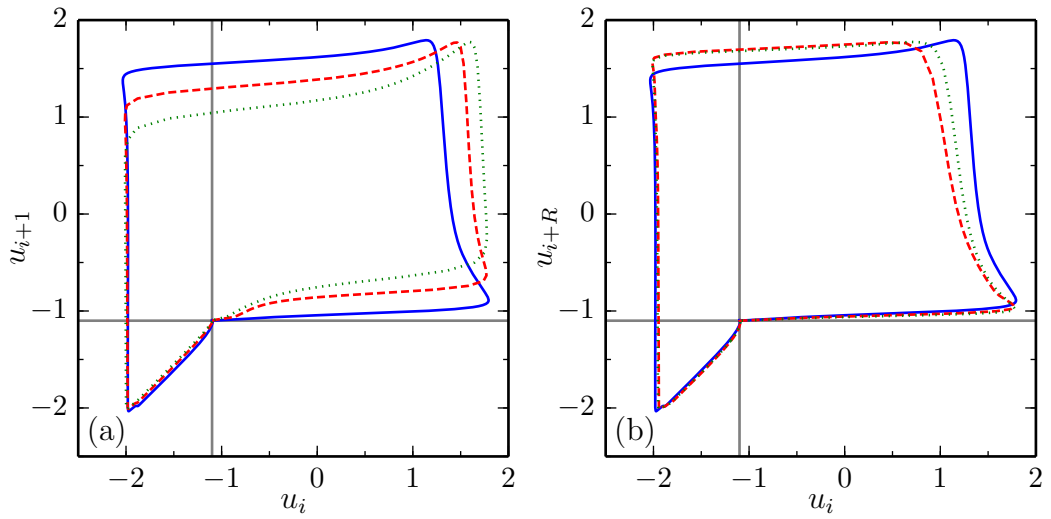

Figure 4.3: Lissajous plot of the activator variable for selected solutions: $N=40$, $R=1$, $D=0.036$ (blue solid), $N=80$, $R=2$, $D=0.024$ (red dashed), $N=120$, $R=3$, $D=0.018$ (green dotted) (same solutions as in Fig. 4.4(c),(d),(e)). (a) u_i vs. u_{i+1}. (b) u_i vs. u_{i+R}. Gray lines mark activator resting value $u_0=\beta$. Other parameters: $\varepsilon=0.04$, $\beta=-1.1$.

If D decreases, this leading front becomes thinner. For low D, the leading front, and therefore the wave, propagates in a 'saltatory' way, which means that successive nodes make the transition from rest to excited individually and temporally separated.

This behavior can be seen e.g. in Fig. 4.3(a) and (b), where the activator value of a node u_i is portrayed against the activator value of the subsequent node u_{i+1} (Fig. 4.3(a)) or u_{i+R} (Fig. 4.3(b)). In these plots, the trajectories leaving the respective resting states u_0 are almost perfectly parallel to the coordinate axes, showing the separate transition to excitation of subsequent nodes. In contrast, the case of large D (Sec. 4.2.1) would result in curves closer to the diagonal as neighboring nodes undergo excitation more simultaneously. This behavior is also noticeable in Fig. 4.4(c)(iv) (which will be discussed in detail in Sec. 4.2.3), where a space-time plot is shown or in the phase portrait of Fig. 4.4(c)(i).

In the system of $2N$ coupled ordinary differential equations given by Eqs. (4.7), a traveling wave solution is a periodic solution with a well-defined period T, given by the time the wave needs to go around the ring exactly once. We call

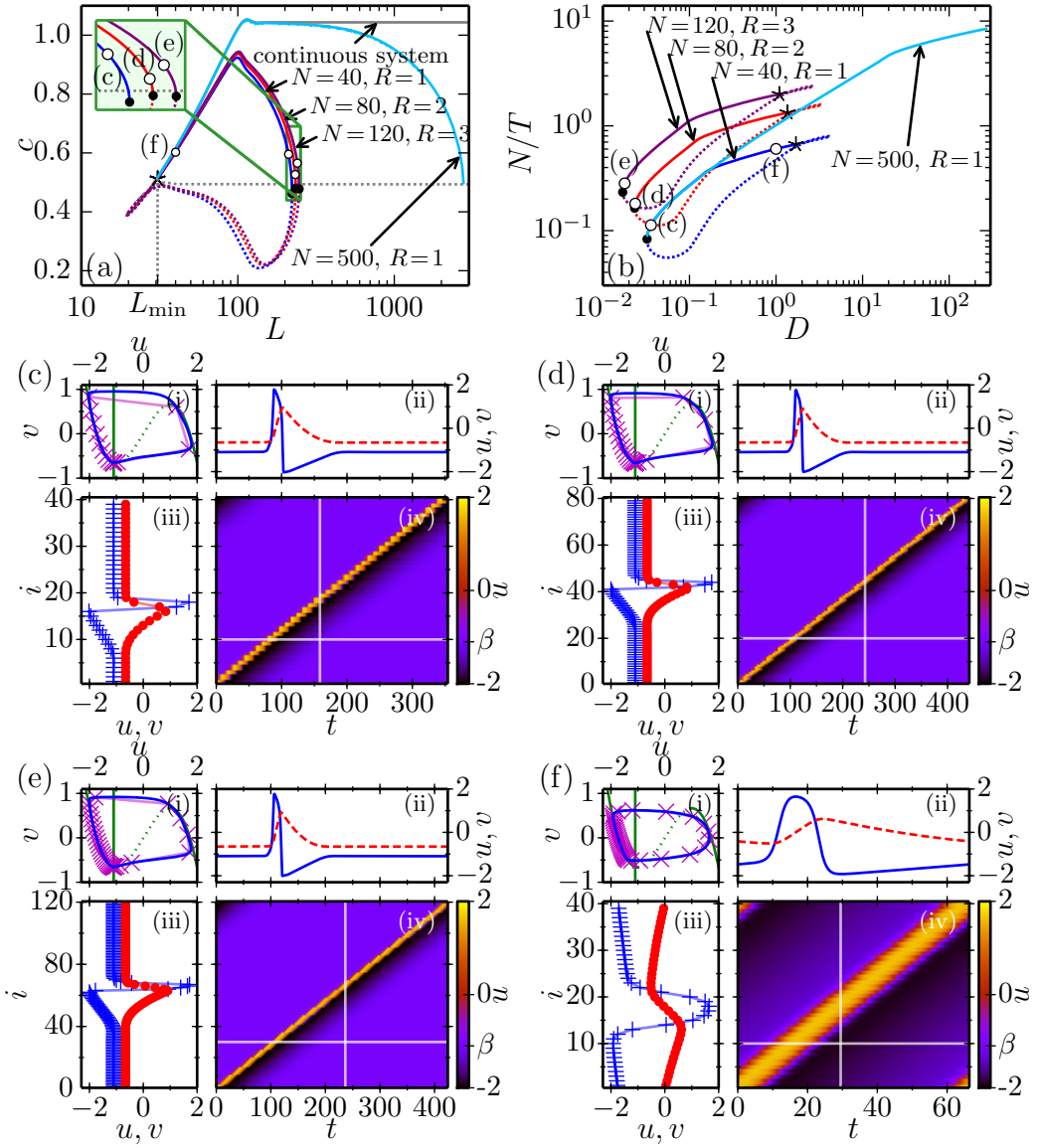

Figure 4.4: Dispersion relation and selected solutions for regular ring networks. (a) $L = N/\sqrt{q(R)D}$ vs. c for branches of stable (solid) and unstable (dotted) solutions for Eqs. (4.7) with $N = 40$, $R = 1$ (blue), $N = 80$, $R = 2$ (red), $N = 120$, $R = 3$ (purple), $N = 500$, $R = 1$ (light blue) and for the continuous system (4.1) (gray). Asterisks mark destabilizing torus bifurcation, black dots mark destabilizing saddle-node bifurcations. Circles mark selected solutions. (b) same as (a) but D vs. c and without solution branches of continuous system. (c) Solution for $N = 40$, $R = 1$, $D = 0.036$ with $c = 0.596$, $L = 211.05$. (d) $N = 80$, $R = 2$, $D = 0.024$ with $c = 0.527$, $L = 232.74$. (e) $N = 120$, $R = 3$, $D = 0.018$ with $c = 0.565$, $L = 240.05$. (f) $N = 40$, $R = 1$, $D = 1.0$ with $c = 0.602$, $L = 40.0$. (Caption continues on next page)

Figure 4.4: (continued) For each solution: (i) (u, v)-plane with path of each node (blue), all nodes' states at one instant of time (magenta crosses). (ii) u (blue solid) and v (red dashed) of one node vs. time t. (iii) u (blue plus symbols) and v (red dots) vs. node # at one instant of time (same as for (i), marked by vertical line in (iv)). (iv) space-time plot of activator u. White horizontal and vertical lines mark node and time for (i),(ii) and (iii). Other parameters: $\varepsilon = 0.04$, $\beta = -1.1$. Solution branches for $N = 40, N = 80, N = 120$ and the continuous system have been obtained by continuation, solution branch for $N = 500$ has been obtained by numerical simulation.

the time between successive jumps the wave's *pace*. It can be calculated as N/T. At low coupling strengths D, a further decrease of D leads to a decrease of the pace N/T and below a minimum value of $D_{\min}$, stable propagation is no longer possible on the ring network [33]. As described in Ref. [34], in that case, the intervals between successive jumps become longer until propagation fails at some node. The dispersion relation (see Fig. 4.4) reveals that at $D_{\min}$, the branch of stable waves collides with a branch of unstable ones in a saddle-node bifurcation.

This type of propagation failure has no analogue in a continuous system. In a one-dimensional reaction-diffusion system, a factor D in front of the spatial coupling term of Eq. (4.1a) can be scaled to one by rescaling space as $1/\sqrt{D}$. Thus decreasing D is equivalent to increasing L and in the limit $D \to 0$, $L \to \infty$ and traveling wave solutions converge to a stable singular traveling pulse.

For traveling waves in the regime of low coupling strengths D, the part of the ring network that is not at rest typically occupies only a few nodes. Thus, the size of the ring N (if it is large enough) does not have an influence on $D_{\min}$. This is in contrast to $D_{\max}$ on which N clearly has an influence (see Sec. 4.2.1).

The coupling range R, however, has an impact on $D_{\min}$, which is shown in Fig. 4.5. Increasing R decreases $D_{\min}$, the dependence can be fitted very well to a function of the form $f(R) = aR^{-1} + bR^{-2}$. The wave's pace at the destabilization point seems to follow a simple linear law, N/T at the destabilization point can be fitted to a function $f(R) = a + bR$. Despite these seemingly

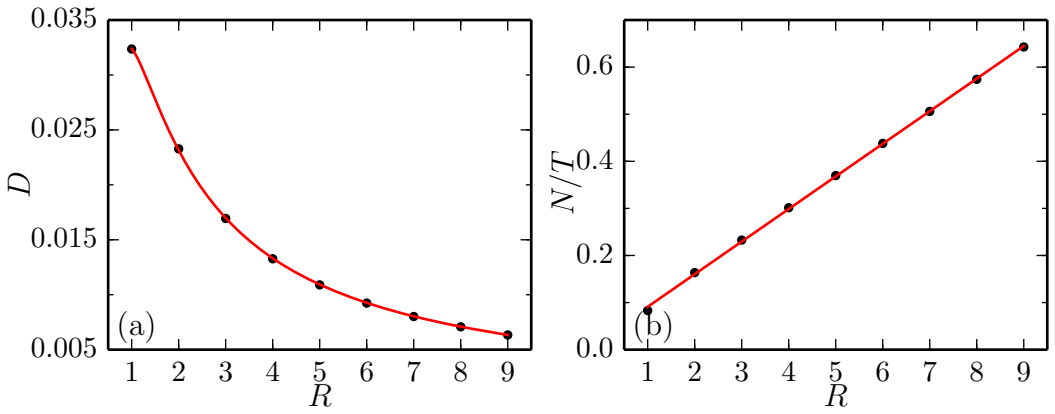

Figure 4.5: Locus of destabilizing saddle-node bifurcation. (a) $D_{\min}$ of destabilizing saddle-node bifurcation vs. coupling range R (black dots). Fitting function $f(R) = 0.06R^{-1} - 0.028R^{-2}$ (red solid). (b) wave 'pace' N/T (time between successive jumps) at destabilizing saddle-node bifurcation vs. coupling range R (black dots). Fitting function $f(R) = 0.022 + 0.69R$. Other parameters: $N = 110$, $\varepsilon = 0.04$, $\beta = -1.1$. Diagram data has been obtained using numerical continuation of the full system Eqs. (4.7).

good agreement, we have not been able to come up with a satisfying analytical explanation for this functionality.

4.2.3 Dispersion relation

Natural quantities of traveling wave solutions on a ring network are the period T of the solution (viewed as a periodic solution to a system of $2N$ coupled ordinary differential equations) and the wave pace N/T. The parameter that is varied is the coupling strength D. In the high D regime, better quantities to compare solutions arise by the limit (4.13). These are the 'virtual' length $L = N/\sqrt{q(R)D}$ and the 'virtual' speed $c = L/T$.

We have performed direct numerical continuation of the entire possible range of D for networks with $N = 40$, $R = 1$, $N = 80$, $R = 2$ and $N = 120$, $R = 3$ yielding branches of stable and unstable solutions. These are shown in Fig. 4.4(a),(b) along with a branch of stable solutions for $N = 500$, $R = 1$ and the branches for the continuous system (only (a)).

In Fig. 4.4(a), as the chosen coordinates are L and c, all branches coincide for small L (corresponding to large D) and destabilize at the same values

$L_{\min}, c$. For large L however, the branches do not coincide, the $N=500$, $R=1$ branch continues to much higher L as the other branches, which destabilize earlier.

In Fig. 4.4(b), the chosen coordinates are D and N/T. Thus the two branches that have $R = 1$ coincide at low D and lose stability at the same point to very good approximation. All branches show very similar behavior, but are shifted and stretched (in this logscale display).

Note that for large networks (represented by $N = 500$ in these Figures), the maximum 'virtual' speed c of a wave on a ring network is given by the maximum speed a wave train in a continuous system can achieve. However, increasing L on a fixed network (by decreasing D) will, beyond a certain point, lead to a decrease of c because of the discrete effects discussed in Sec. 4.2.2. In contrast to that, the pace N/T will always increase, if D increases, attaining the maximum value for stable traveling waves at the destabilization point $D_{\max}$. As $D_{\max} = N^2/L_{\min}^2 q(R)$ and ring networks with arbitrarily large N can be considered, there is neither a general upper limit for the maximum pace nor for $D_{\max}$.

The dispersion relations for networks shown in Fig. 4.4 are noticeable because the branch of unstable traveling waves meets with the branch of stable traveling waves twice, thus generating a closed dispersion relation curve for traveling waves on ring networks. The point at low D (high L respectively), where these branches meet, is a saddle-node bifurcation point (of periodic solutions). This is the point of propagation failure in the discrete limit discussed in Sec. 4.2.2. The destabilization at high D happens by a torus bifurcation which has its counterpart in the torus bifurcation of traveling waves on a continuous spatial system with periodic boundary conditions (Fig. 4.2(d)). Beyond this torus bifurcation, a series of secondary instabilities, as described in Sec. 4.1.2, finally leaves just one eigenvalue in the right half plane, which becomes negative again in the low-D saddle-node bifurcation. Note that the coordinates of Fig. 4.4(a) and 4.2(a) as well as Fig. 4.4(b) and 4.2(b), have been chosen to be comparable.

Chapter 5

Excitation waves on tree networks

It is clear that the spreading of excitation depends on the network architecture. In this chapter, we focus on the influence of the node degree on the propagation of excitation waves. For this reason it is to avoid that the wave can reenter the node after propagating through it. These two requirements suggest regular tree networks as a model system because in those, no closed paths exist and every node has the same degree (see Sec. 2.3.2).

In order to study excitation waves on tree networks, we will first use direct numerical simulation of the dynamics on tree networks. We find that the larger the degree is, the slower the propagation speed becomes. Above a certain critical degree, propagation fails, and no excitation waves exist on the tree network. The structure of tree networks together with the structure of the solution allows us to exploit a symmetry in the system and radically simplify the topology. From a tree network we will construct a directed weighted chain network that can be used instead of the regular tree network for this type of solution.

In the limit of high coupling strengths, we construct an approximating continuous reaction-diffusion system. This is employed to study wave propagation and propagation failure using the profile equations and a variant of the kinematical theory [36]. Both methods correctly predict the critical degree and to some extent the dependence of the velocity on the degree.

In the limit of low coupling strengths, we use direct numerical continuation of the equivalent directed weighted chain network to calculate the critical degree. The obtained critical degree agrees well with the value from numerical

simulation. Furthermore, we are able to use an analytic approximation to understand the mechanism of propagation failure in the low coupling strength case. This analytical method correctly predicts the dependence of the critical degree on the coupling strength which interestingly shows a maximum value at a certain optimal coupling strength.

In addition, we are able to apply our results to excitation spreading in a random network architecture. The critical degree from the studies on tree networks correctly predicts the nodes at which excitation stops on an Erdős-Rényi random network.

The chapter is structured as follows: In Sec. 5.1, we present the model and the general numerical findings. Using the symmetries of model and solution, we reduce the equations of the regular tree network to those on a directed weighted chain network. In Sec. 5.2, we discuss the high coupling strength continuum regime. In Sec. 5.2.1, we set up the profile equations and the boundary value problem that is used to evaluate stability. In Sec. 5.2.2, we use the framework of the kinematical theory to analytically assess the destabilization point. In Sec. 5.3 we treat the low coupling strength discrete regime case. We use direct continuation in Sec. 5.3.1 and the active point approximation in Sec. 5.3.2. In Sec. 5.3.3, we apply our findings to the case of Erdős-Rényi random networks.

The results presented in this chapter have been published in Ref. [96].

5.1 Model

We consider a regular tree network that is constructed such that from the chosen root node, every leaf node has the same distance. Recall from Sec. 2.3.2 that the number $k-1$, where k is the degree of the non-leaf nodes is called the *branching ratio*. When we speak of the node degree k on a tree network, we mean the degree of the non-leaf nodes unless otherwise noted.

On every node of this tree network, we consider a FitzHugh-Nagumo system Eqs. (3.2) (see also Chapter 3 and references therein). The coupling of these units is determined by the tree topology and given by the difference in activator concentrations multiplied by a global coupling strength $D > 0$. Thus, the

system reads

$$\dot{u}_i = u_i - \frac{u_i^3}{3} - v_i + D\sum_{j=1}^{N} \mathcal{A}_{ij}\,(u_j - u_i) \tag{5.1a}$$

$$\dot{v}_i = \varepsilon(u_i - \beta)\,, \qquad i \in \{1, ..., N\}\,, \tag{5.1b}$$

where ε and β are chosen such that we are in the excitable regime (cf. Sec. 3.2) and $\mathcal{A}_{ij}$ is the adjacency matrix of a regular tree as discussed above. The numbering of the nodes is such that the root node has index 1.

We denote the steady state of the local dynamics, i.e. Eqs. (3.2) by (u_0, v_0). As discussed in Sec. 3.3, the homogeneous state $(u_i, v_i) = (u_0, v_0)$, $i \in \{1, ..., N\}$ is stable.

5.1.1 Observations

As a first step, we integrate Eqs. (5.1) numerically, where at $t = 0$, $(u_i, v_i) = (u_0, v_0)$ for all nodes except the root node, which is put in an excited state $(u_{\text{root}} = 2, , v_{\text{root}} = v_0)$. This way, an excitation that spreads from the root node outwards into the periphery of the tree network can be generated. In Fig. 5.1 snapshots from such numerical simulations are shown, the colorcode corresponds to the value of u_i. In Fig. 5.1(a), the considered tree has degree $k = 3$ and the excitation spreads from the root to the periphery. The same holds for Fig. 5.1(b), where $k = 4$ and the propagation to the periphery is a little slowed down. For the tree network with $k = 5$, shown in Fig. 5.1(c), the excitation stops at the neighbors of the root node and does not continue to propagate further outwards. Note that due to the different propagation speeds in Figs. 5.1(a),(b),(c), the times of the snapshots have been chosen differently in order to have the excitation of the shells more clearly in the picture.

We observe the same pattern for different D and ε (figures not shown here). Propagation outwards slows down when k is increased and above a certain critical k_{cr} wave propagation will fail. In contrast to bistable systems on regular tree networks [23, 97], we do not observe pinning of excitation waves or the reversal of the propagation direction.

The value of the critical degree k_{cr} above which propagation fails depends on the coupling strength D as well as on timescale separation and threshold

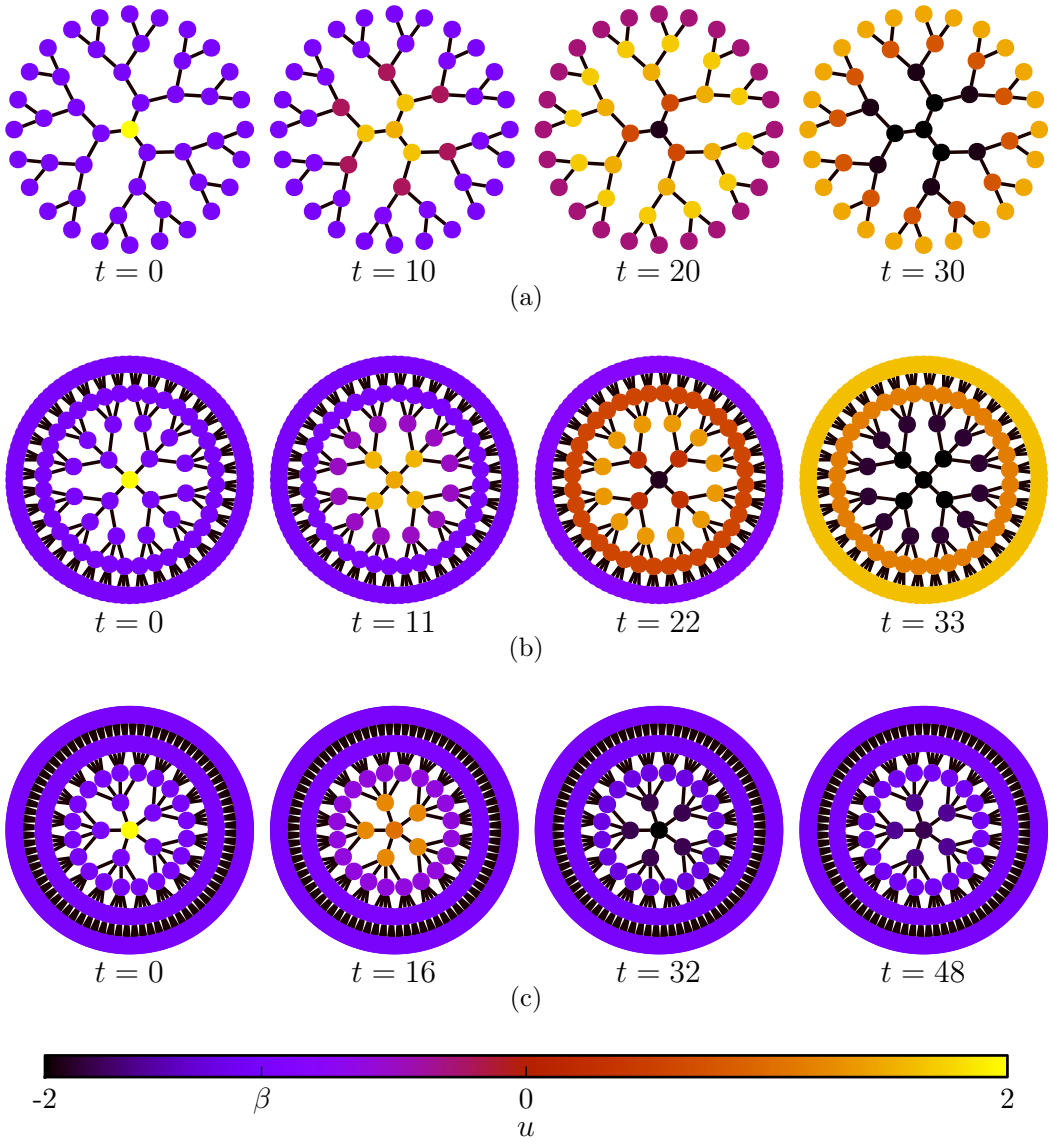

Figure 5.1: Excitation waves on tree networks. Snapshots for results of numerical simulation of Eqs. (5.1) on a regular tree network (only activator level is shown as colorcode). Initially, all nodes are in the rest state, $u_i(0) = \beta$, $i = 2, ..., N$, except the chosen root node, which has $u_0(0) = 2$. (a) $k = 3$ (except leaf nodes), (b) $k = 4$ (except leaf nodes), (c) $k = 5$ (except leaf nodes). Other parameters: $D = 0.07$, $\varepsilon = 0.04$, $\beta = -1.1$.

parameters ε and β, respectively. In the following, we will focus on the dependence of the propagation speed on k and on the dependence of k_{cr} on ε in different regimes of the coupling strength and the dependence on D when D is low.

5.1.2 Reduction to chain of shells

Direct simulation of the dynamics on a tree network has two main disadvantages. Firstly, in a tree network with branching factor $k-1$, there are $(k-1)^r$ nodes at distance r to the root node, the number of nodes grows exponentially fast with the distance to the root. Thus, simulating a tree topology with many levels directly would be computationally very expensive. Secondly, the parameter k is an integer, which makes it challenging to study its influence because a smooth increase is not possible.

When starting the excitation from the root node, as in Fig. 5.1, every neighbor of the root node receives exactly the same input (because there are no connections between these nodes directly) and thus follows exactly the same dynamics. By the same argument, we find that every node at a distance r to the root node follows exactly the same dynamics. We say that nodes with the same distance to the root node belong to the same *shell*. Using the directionality provided by choosing a root node, we see that every node (other than the root node) is coupled to one node towards the root and couples to $k-1$ nodes away from the root (except leaf nodes). Thus, we can collapse the topology of the tree network to the topoplogy of a chain of shells, weighting links towards the root by 1 and links away from the root by $k-1$. Such an equivalent (weighted and directed) chain network is shown in Fig. 5.2. The dynamics on this chain of shells is given by

$$\dot{u}_r = u_r - \frac{u_r^3}{3} - v_r + D\left(u_{r-1} + (k-1)u_{r+1} - k u_r\right) \tag{5.2a}$$

$$\dot{v}_r = \varepsilon(u_r - \beta)\,, \qquad r \in \{1, ..., L\}\,, \tag{5.2b}$$

where r is indexing the shell. L is the number of shells to be considered. For the root node ($r = 1$), the coupling term is given by $D\left(k u_2 - k u_1\right)$ whereas for leaf nodes ($r = L$) it is $D\left(u_{L-1} - u_L\right)$,

Using Eqs. (5.2), we can study the dynamics for many levels of a tree network at low computational cost. Moreover, in these equations, k does not need

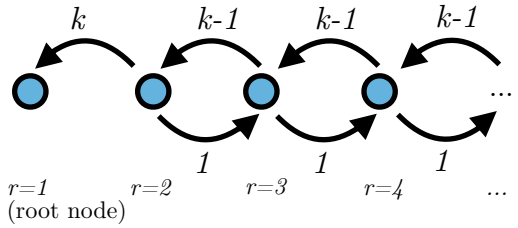

Figure 5.2: Schematic of directed weighted chain network of shells Eqs. (5.2) used to model wave propagation on a regular tree network Eqs. (5.1).

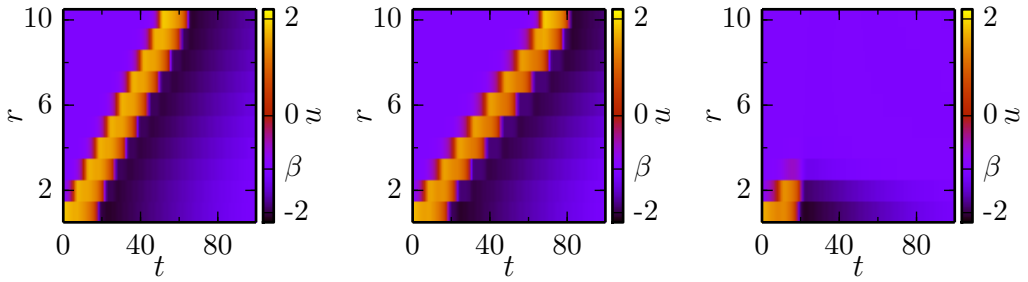

Figure 5.3: Excitation waves on tree networks Eqs. (5.1). Space-time plot for the equivalent network of shells Eqs. (5.2). $r =$ index of shell ($r = 1, 2, 3, ...$). (a) $k=3$, (b) $k=4$, (c) $k=5$. Other parameters: $D=0.07$, $\varepsilon=0.04$, $\beta=-1.1$

to take integer values anymore. This makes Eqs. (5.2) suitable for (numerical) solution continuation used, e.g. in Sec. 5.3.1. In Fig. 5.3, we show numerically obtained solutions of Eqs. (5.2) for the same parameters as in Fig. 5.1. The space-time plots of Fig. 5.3 show the same results as Fig. 5.1, slowing down of propagation for $k = 4$ (Fig. 5.3(a)) as compared to $k = 3$ (Fig. 5.3(b)) and propagation failure for $k = 5$ (Fig. 5.3(c)).

In the next sections, we will discuss the behavior of traveling wave solutions in the high D and low D regime in detail.

5.2 High coupling strength – continuum regime

In the following, we use the equivalent directed weighted chain network of shells Eqs. (5.2). For the regime of high coupling strengths D, we assume a very large number of shells (> 1000).

If the coupling strength is high, the states of neighboring nodes vary only very little, thus we approximate u_{r+1} and u_{r-1} by the Taylor expansions of a function $u(r) = u_r$ near r:

$$u_{r-1} \approx u(r) - u'(r) + \frac{1}{2}u''(r) \tag{5.3a}$$

$$u_{r+1} \approx u(r) + u'(r) + \frac{1}{2}u''(r)\,, \tag{5.3b}$$

where $u'(r)$ denotes the derivative with respect to r.

Using these substitutions, we approximate Eqs. (5.2) in the limit of large coupling strengths D by

$$\dot{u}(t,r) = u - \frac{u^3}{3} - v + \frac{Dk}{2}u'' + D(k-2)u' \tag{5.4a}$$

$$\dot{v}(t,r) = \varepsilon(u - \beta)\,, \tag{5.4b}$$

which is a reaction-diffusion system with an additional first-order derivative (drift) term. For $k = 2$ in which the tree network would be a chain network, the additional derivative term vanishes. Thus this term models the effect of the branching in a tree. Note that it is not possible to rescale the spatial coordinate such that $D = 1$ in this case because D appears in front of a second as well as a first spatial derivative. Therefore, these pick up different factors when rescaling space.

5.2.1 Profile equations

Under the assumption that an excitation wave in Eqs. (5.4) moves at constant speed c, we introduce the comoving reference frame $\xi = r - ct$. We use $\dot{u}(t,r) = -cu'(\xi)$ and $u'(t,r) = u'(\xi)$ and reduce the system Eqs. (5.4) to the system of ordinary differential equations

$$-\left[c + D(k-2)\right]u' = u - \frac{u^3}{3} - v + \frac{Dk}{2}u'' \tag{5.5a}$$

$$-cv' = \varepsilon(u - \beta)\,, \tag{5.5b}$$

where $u(\xi)$, $v(\xi)$ now are the profile functions (see Sec. 4.1) and u', v' denotes the derivative with respect to ξ. This is completely analogous to the procedure outlined in Sec. 4.1.1.

We can write Eqs. (5.5) as a first order system

$$u' = w \tag{5.6a}$$

$$v' = -\frac{\varepsilon}{c}(u - \beta) \tag{5.6b}$$

$$w' = -\frac{2}{Dk}\left\{u - \frac{u^3}{3} - v + [c + D(k-2)]\, w\right\} . \tag{5.6c}$$

The homogeneous steady state on a tree network appears as a steady state in Eqs. (5.6). Excitation waves on an infinitely extended tree network with large coupling strength D will appear as a homoclinic solution to this steady state of Eqs. (5.6).

Using Eqs. (5.6), we will perform a numerical continuation of periodic orbits with very large period T with respect to the parameter k. These solutions approximate the homoclinic solution of the solitary excitation wave on the tree network very well as explained in Sec. 4.1.1. As a starting solution, we can use a numerically obtained excitation wave on an ordinary chain ($k = 2$).

As described in Sec. 4.1.2, stability properties of the excitation waves cannot be inferred from a linearization of Eqs. (5.6) around the wave profiles. Instead we have to use the technique described in Sec. 4.1.2, which amounts to solving a slight modification of the boundary value problem given by Eqs. (4.6)

$$\delta u' = \delta w \tag{5.7a}$$

$$\delta v' = \frac{1}{c}\left(\lambda \delta v - \varepsilon \delta u\right) \tag{5.7b}$$

$$\delta w' = \lambda \delta u - \left[(1 - u^2)\delta u - \delta v\right] - [c + D(k-2)]\, \delta w \tag{5.7c}$$

$$\delta u(T) = \mathrm{e}^{i2\pi\nu} \delta u(0) \tag{5.7d}$$

$$\delta v(T) = \mathrm{e}^{i2\pi\nu} \delta v(0) \tag{5.7e}$$

$$\delta w(T) = \mathrm{e}^{i2\pi\nu} \delta w(0)\,, \tag{5.7f}$$

where u in Eq. (5.7c) is the activator profile function for the wave solution, for which the stability is to be determined and T is its period.

By this branch continuation and spectral calculations, we obtain the dependence $c(k)$ for fixed D, ε and β shown in Fig. 5.4 and the information whether a certain wave profile describes a stable or an unstable traveling wave. We observe the same qualitative dependence as in the simulations for low coupling strengths Figs. 5.1 and 5.3, a decrease of the propagation velocity of the stable

branch with increasing k and a maximum k above which no stable propagation occurs. From the analysis of the essential spectrum, we find that the mechanism for propagation failure in the regime of high coupling strengths is a saddle-node bifurcation at which a branch of stable propagating waves collides with a branch of unstable ones. The spectrum for selected solutions on the stable as well as on the unstable branch is shown in Figs. 5.4(b)-(f). This spectra clearly show one part of the essential spectrum crossing the imaginary axis at solution marked by a ●. The u-profiles for the corresponding solutions are shown in Fig. 5.4(g), the excited part of these becoming narrower as one wanders along the branch from stable to unstable.

5.2.2 Kinematical theory

As shown by Nikos Kouvaris in Ref. [96], a modification of the kinematical theory [36] can be applied to wave propagation is Eqs. (5.4). Starting with the equations in the comoving frame (5.5), we introduce

$$\varepsilon^* := \varepsilon \left[1 + \frac{D(k-2)}{c} \right] . \tag{5.8}$$

Then, Eqs. (5.5) become

$$-\left[c + D(k-2)\right] u' = u - \frac{u^3}{3} - v + \frac{Dk}{2} u'' \tag{5.9a}$$

$$-\left[c + D(k-2)\right] v' = \varepsilon^* (u - \beta) . \tag{5.9b}$$

Thus, the velocity $\tilde{c}$ of these equations in dependence on the new parameter ε^* is given by

$$\tilde{c}(\varepsilon^*) = c + D(k-2) . \tag{5.10}$$

In simulations and continuation, we find that for small ε, c in dependence on ε can be approximated linearly by $c(\varepsilon) = c_0(1 - \chi\varepsilon)$, where c_0 and χ are parameters that do not depend on ε and are obtained by fitting. By assuming that the same dependence (with the same c_0 and χ) holds for $\tilde{c}(\varepsilon^*)$, we arrive at

$$\tilde{c}(\varepsilon^*) = c + D(k-2) = c_0(1 - \chi\varepsilon^*) . \tag{5.11}$$

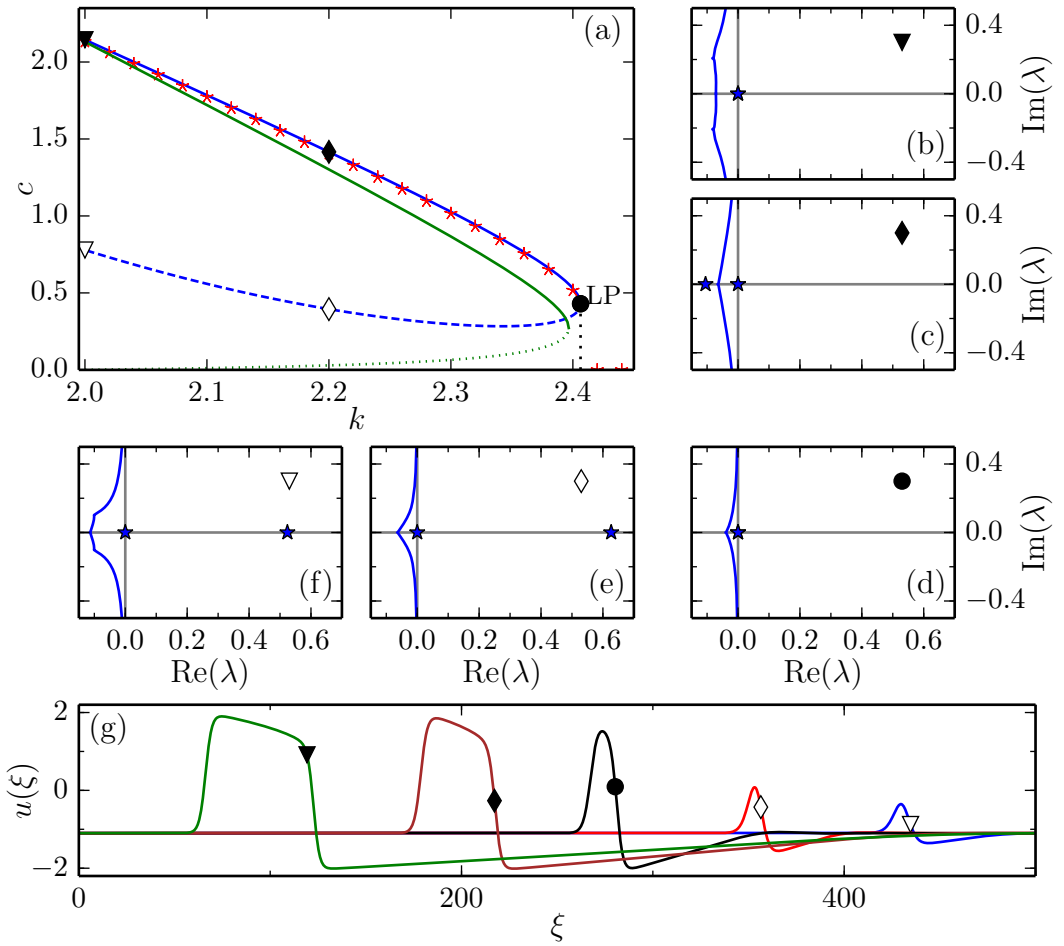

Figure 5.4: Waves on tree networks in the limit of large D. (a) Propagation speed c vs. k. Numerically obtained solutions of Eqs. (5.2) (red asterisks). Kinematical theory solution, fast (green solid) and slow (green dotted) branch. Stable (blue solid) and unstable (blue dashed) solution branches obtained by numerical continuation of Eqs. (5.5). Marked are stable/unstable solutions obtained by continuation at $k = 2$ (▼/▽) and $k = 2.2$ (♦/◊) and the limit-point solution at $k \approx 2.406$ (●). (b) Essential spectrum for stable wave profile at $k = 2$ (▼), (c) for stable solution at $k = 2.2$ (♦), (d) for limit point solution at $k \approx 2.406$ (●), (e) for unstable solution at $k = 2.2$ (◊) and (f) for unstable solution at $k = 2.0$ (▽). Components of the essential spectrum which are very small are marked with a star in order to be visible at this scale. (g) $u(\xi)$ for all solutions marked in (a). Only the part of the profile that deviates significantly from the rest state is shown. For all shown solutions $\xi \in [0, 1075)$ but only the part, where u deviates significalntly from the resting state ($\xi \in [0, 480]$) is shown. Other parameters: $D = 4.0$, $\varepsilon = 0.02$, $\beta = -1.1$. Parameters for the kinematical theory: $c_0 = 2.178$, $\chi = 1.074$.

Substituting the definition of ε^* Eq. (5.8), we get

$$c + D(k-2) = c_0 \left(1 - \chi\varepsilon \left[1 + \frac{D(k-2)}{c}\right]\right) ,$$

which gives us the quadratic equation for c

$$0 = c^2 + c\left[D(k-2) - c_0 + \chi\varepsilon c_0\right] + \chi\varepsilon c_0 D(k-2) ,$$

with the solutions

$$\begin{aligned} c = \frac{1}{2}\Bigg\{ & D(k-2) - c_0(1-\chi\varepsilon) \\ & \pm \sqrt{\left[D(k-2) - c_0(1-\chi\varepsilon)\right]^2 - 4\chi\varepsilon c_0 D(k-2)} \Bigg\} . \end{aligned} \tag{5.12}$$

The two branches of c are shown in green in Fig. 5.4(a). They merge, when

$$\left[D(k-2) - c_0(1-\chi\varepsilon)\right]^2 = 4\chi\varepsilon c_0 D(k-2) , \tag{5.13}$$

which gives

$$k_{\text{crit}} = 2 + \frac{c_0(1-\sqrt{\varepsilon\chi})^2}{D} \qquad c_{\text{crit}} = c_0(\varepsilon\chi - \sqrt{\varepsilon\chi}) \tag{5.14}$$

as the critical value for k and the velocity at this critical value. For the values of Fig. 5.4, $c_0 = 2.178$, $\chi = 1.0174$ and thus $k_{\text{crit}} = 2.397$, $c_{\text{crit}} = 0.272$. The solution of Eq. (5.13) with a plus in front of the squareroot is not of interest because $c(k)$ becomes negative in that case.

Comparing the two branches obtained by the kinematical theory (green lines) with those obtained numerically (red asterisks) in Fig. 5.4, we see that the kinematical theory is very accurate in predicting k_{crit} but less accurate for the velocity c_{crit} at the critical point. The main reason for the deviation towards larger k is that the assumption of linearity in Eq. (5.11) is only valid for small ε resp. ε^*. When k is increased, ε^* increases as well and as D is assumed to be large, ε^* soon is not small enough anymore to assume a linear dependence $\tilde{c}(\varepsilon^*)$.

5.3 Low coupling strength – discrete regime

For low coupling strengths D, it takes more time until the excitation of the next shell is triggered by its predecessor shell. Thus, propagation becomes

slower and the wave will be confined to a smaller number of nodes. For very low coupling strengths D, the transition regions of a traveling wave solution of Eqs. (5.2) occupy only a few nodes. Thus, similarly as in Sec. 4.2.2, the discrete nature of Eqs. (5.2) becomes important.

5.3.1 Direct continuation

As the entire part of the wave that deviates significantly from the rest state is located within a small number of shells, L in Eqs. (5.2) needs not to be large to investigate excitation wave propagation in tree networks in the limit of low D. This low number L of shells makes direct numerical continuation of solutions of Eqs. (5.2) numerically affordable.

We introduce artificial periodic boundary conditions on Eqs. (5.2), identifying shell $L+1$ with shell 1. The resulting system is a ring network in which each node is coupled with weight $k-1$ to its neighbour in clockwise direction and with weight 1 to its neighbour in counterclockwise direction. On this ring, excitation waves appear as periodic solutions with a certain period T. The velocity can by calculated by $c = L/T$. Locally, the nodes of such a ring resemble the shells of a tree network. Globally, however, the ring cannot be mapped to a tree. By locally, we mean that the wave solutions are constrained to a small part of the ring such that they do not interact with themselves. In other words, the fraction of nodes in the resting state is always large enough to clearly separate the beginning and the end of an excitation wave.

Because for the nodes in the resting state and with neighbors in the resting state, the coupling term vanishes, we expect to observe the same dynamics as in the shells of a tree network if we are in a range of parameters where the wave-like solutions are well-localized in the above sense. This is corroborated by Fig. 5.5(a). Locations of solutions obtained by direct simulation of Eqs. (5.2) and branches of stable solutions obtained by numerical continuation of Eqs. (5.2) with the mentioned artificial periodic boundary conditions show excellent agreement.

The direct numerical continuation of excitation waves on tree networks as periodic orbits makes it possible to calculate k_{crit} exactly, to investigate its dependence on ε and D and to calculate the unstable traveling waves that coexist with the stable ones. In Fig. 5.5(a) (velocity vs. k), branches for

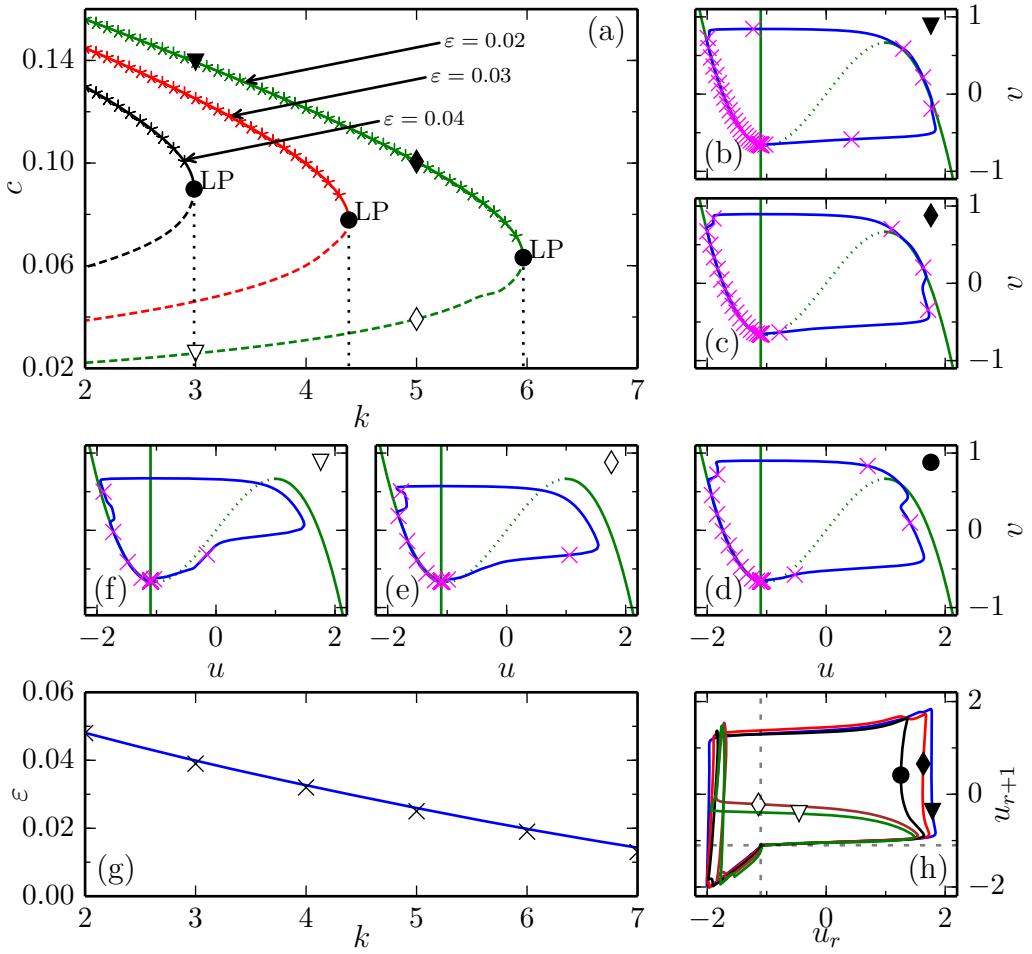

Figure 5.5: Waves on tree networks in the regime of low D. Solutions of Eqs. (5.2). (a) Branches of stable (solid lines) and unstable (dashed lines) waves obtained from numerical continuation. Solutions from simulation (asterisks). c vs. k for $\varepsilon = 0.02$ (green), 0.03 (red) and 0.04 (black). For $\varepsilon = 0.02$ marked are: stable/unstable solutions at $k = 3$ (▼/▽) and $k = 5$ (♦/◊) as well as the limit point solution at $k \approx 5.966$ (●). (b) Phase portrait for stable solution with $\varepsilon = 0.02$, $k = 3$ (▼). Path that each node takes in the u-v plane (blue solid), nullclines (green) and snapshot with state of each node at one instant of time (magenta crosses) (c) Same as (b) for stable solution with $\varepsilon = 0.02$, $k = 5$ (♦). (d) Same as (b) for limit point solution at $\varepsilon = 0.02$, $k \approx 5.966$ (●). (e) Same as (b) for unstable solution with $\varepsilon = 0.02$, $k = 5$ (◊). (f) Same as (b) for unstable solution with $\varepsilon = 0.02$, $k = 3$ (▽). (g) Location of limit points(LP, saddle-node bifurcation). k vs. ε from continuation (blue line) and simulation (black crosses). (h) Lissajous plot u_r vs. u_{r+1} for the solutions marked in (a). Other parameters: $\beta = -1.1$, $D = 0.04$, and for the continuation $L = 50$.

stable (solid) and unstable (dashed) traveling waves are shown for different ε (red,green,blue). Increasing k always leads to decreasing velocity of the stable traveling wave until the branch merges with the branch of unstable ones in a saddle-node bifurcation at k_{crit}. The same behavior is observed, when the timescale separation constant ε is increased instead of k. Thus for smaller ε, k_{crit} becomes larger as is shown in Fig. 5.5(g). The reason for this behavior is that a smaller ε leads to an increase of the time that a shell is excited because during excitation, the dynamics is governed by Eq. (5.2b). With this increased excitation time, a shell can trigger an excitation in shells of more nodes (larger k).

We also observe the influence of the branching ratio $k-1$ on the shape of the solutions. In Figs. 5.5(b)-(f), two stable, two unstable and the limit point solution for $\varepsilon = 0.02$ are shown in the (u, v) plane. In Fig. 5.6(a)-(e), the corresponding timeseries of the activator at one shell u_r and its successor u_{r+1} are shown. The asymmetrically weighted coupling (weight 1 to the previous and $k-1$ to the next shell) of Eqs. (5.2) leads to the evolution of two 'dips'. One at large values of u and small values of v and one at small values of u and large values of v.

The reason is that in Eq. (5.2a), the coupling term for a shell r, whose current state is already governed by the slow timescale of Eq. (5.2b), can change with the fast timescale, when shell $r+1$ moves on the fast manifold from the rest state to the excited state. This is visualized by the magenta crosses (giving the individual u_i, v_i at one instant of time) in Fig. 5.5(b)-(f). Because the state of shell $r+1$ enters the coupling term of shell r with weight $k-1$, whereas the state of shell $r-1$ enters with weight 1, the 'force' exerted by the coupling term 'pulls' the state of shell r into the direction of the resting state, when shell $r+1$ is still close to the resting state. It does so more strongly with increasing k. The second dip is caused by the same effect, when shell $r+1$ transitions back into the resting state from the excited state. This can also be seen in the Lissajous plot Fig. 5.5(h), where u_r is displayed against u_{r+1}. The curves in this plot are almost parallel to the coordinate axes, thus showing that the change with the fast timescale happens separately for each shell.

The activator level of shell $r+1$ is shown in Figs. 5.6(a)-(e) as a green dotted line and the activator state of shell r as a blue solid line. For the stable

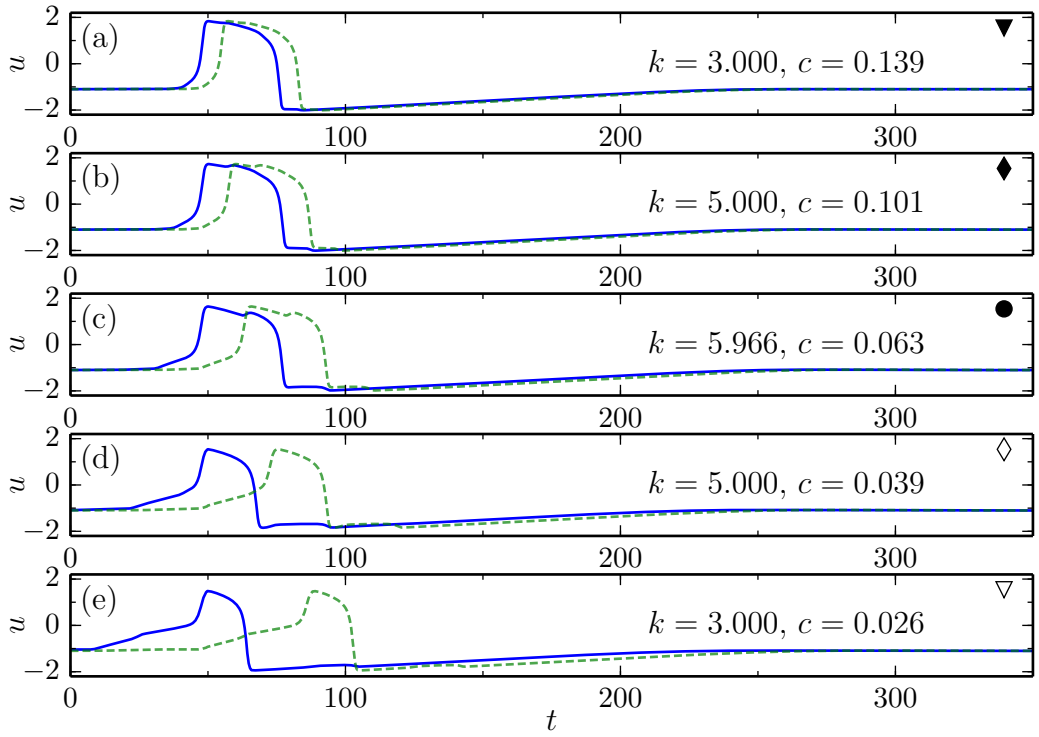

Figure 5.6: Waves on tree networks in the regime of low D. (a) u_r (blue solid) and u_{r+1} (green dashed) vs. t for stable solution at $k = 5$ (▼ in Fig. 5.5(a)), (b) for stable solution with $k = 5$ (⧫ in Fig. 5.5(a)), (c) for limit point solution at $k \approx 5.966$ (● in Fig. 5.5(a)), (d) for unstable solution with $k = 5$ (◊ in Fig. 5.5(a)) and (e) for unstable solution with $k = 3$ (▽ in Fig. 5.5(a)). Other parameters: $\varepsilon = 0.02$, $\beta = -1.1$, $D = 0.04$, and $L = 50$. In all pictures (a)-(e), the timeseries has been cut to show only $t \in [0, 350]$. All timeseries are longer (period in the continuation $T = L/c$, with artificial periodic boundary conditions).

solutions and the limit point solution Figs. 5.6(a),(b),(c) the first dip not only becomes more pronounced with increasing k, it also happens more retarded. This is understandable because in the coupling term of shell $r+1$, shell r enters with weight 1 whereas shell $r+1$ enters the coupling term of shell r with weight $k-1$. Therefore, the excited activator value of shell r becomes lower, when k is increased, which can be seen by comparing the maximum values of u_r of these solutions (marked ▼, ⧫ and •) in Fig. 5.5(h). Because of the reduced excitation height, it takes longer to trigger the excitation in the next shell, which can be seen in Figs. 5.6(a)-(e). This also explains the decrease of the

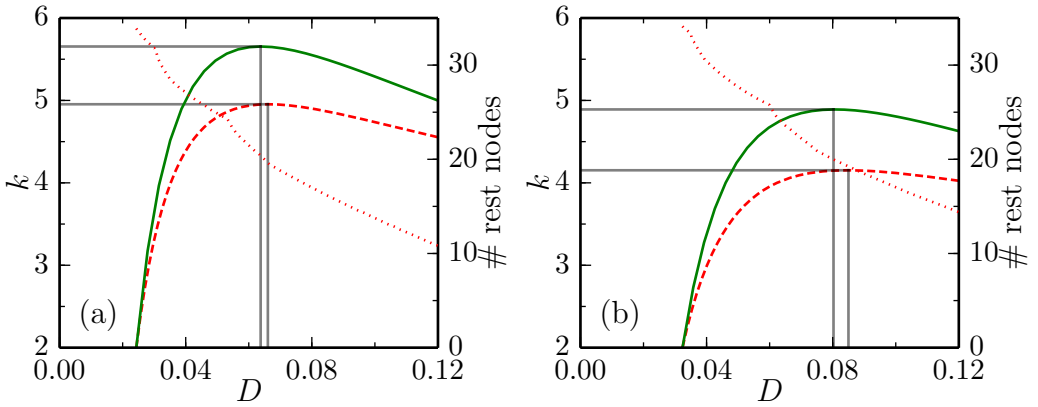

Figure 5.7: $k_{\mathrm{crit}}(D)$ obtained from continuation (red dashed), by active point approximation of Sec. 5.3.2 (green solid) and number of shells within a radius of 10^{-4} to the steady state (u_0, v_0) for the continuation solution (red dotted). The values D and k at the maxima of the obtained curves are indicated by vertical and horizontal gray lines. (a) $\varepsilon = 0.03$, (b) $\varepsilon = 0.04$. Other parameters: $\beta = -1.1$.

velocity c with increasing k.

For the unstable solutions in Figs. 5.6(d),(e), both transitions of shell $r+1$ happen when shell r is already decaying to the resting state. This difference to the stable solutions and to the limit point solution can very clearly be seen in Figs. 5.6(a)-(e) and in Fig. 5.5(h).

5.3.2 Dependence on coupling strength and active point approximation

In a tree network, the minimum value of k is 2 (excluding leaf nodes). Thus, in Eqs. (5.2) $k \geq 2$. As discussed in Sec. 4.2.2, in ring networks there exists a minimum value D_{min} below which no wave propagation is possible. This value D_{min} is also valid for chains as discussed in Sec. 4.2.2 and a chain is the same as a tree network with $k = 2$. Thus at D_{min}, $k_{\mathrm{crit}} = 2$ for a given ε. For large D, the kinematical theory of Sec. 5.2.2 tells us by Eq. (5.14) that k_{crit} decreases with increasing D. Therefore, at some value D_{opt}, k_{crit} must attain a maximum value.

In Fig. 5.7 the numerical continuation results for $k_{\mathrm{crit}}(D)$ at $\varepsilon = 0.04$ and $\varepsilon =$

0.03 are shown, clearly displaying a maximum value of k_{crit}. The continuation of the limit point solution at k_{crit} of Eqs. (5.2) for Fig. 5.7 has been done with $L = 50$ and the number of nodes in the rest state has been monitored to assure that the leading front does not interact with the tail of the wave because of the artificially introduced boundary conditions. k_{crit} is only shown for values of D with at least 10 nodes being within a radius of 10^{-4} to the rest state. Thus, we try to ensure that enough nodes are in the resting state and the artificial periodic boundary condition do not have an influence on the solution. The number of 10 nodes and the distance of 10^{-4} have been chosen heuristically.

We can use a modification of the active point approximation from [33] to calculate $k_{\text{crit}}(D)$ analytically and get more insight into the mechanism. This approximation uses the fact that for low D, the transitions to excitation are temporally well separated (saltatory propagation). Activator u and inhibitor v for one shell (the 'active point') are modeled. For the coupling term appearing in the activator equation of the active point, the values of activator at shells $r-1$ and $r+1$ are needed. As shell $r-1$ has just undergone excitation, its activator value changes with the slow timescale and thus is given through adiabatic elimination as a function of its inhibitor value which is assumed to conincide with that of shell r. We denote this function by $u^-(v)$. A similar reasoning holds for shell $r+1$ whose activator value is approximated by a function $u^+(v)$. Thus the equations for the active point are

$$\dot{u} = u - \frac{u^3}{3} - v + D(u^-(v) + (k-1)u^+(v) - ku) \tag{5.15a}$$

$$\dot{v} = \varepsilon(u - \beta)\,. \tag{5.15b}$$

We approximate $u^+(v)$ and $u^-(v)$ by the stable solutions of the fast subsystem of Eqs. (5.15) (see Sec. 3.2.1). A first ansatz for this would be

$$\begin{aligned} 0 &= u - \frac{u^3}{3} - v \\ &=: f(u) - v\,, \end{aligned} \tag{5.16}$$

as in Ref. [33]. As the inhibitor value of the active point is close to the rest value, we will have three solutions to this equation. We term those solutions $z_1(v) < z_2(v) < z_3(v)$, with z_1 and z_3 being stable.

For modeling the activator value of shell $r+1$ which is still at rest, this is sufficient and we use $u^+(v) = z_1(v)$. This is not sufficient for modeling

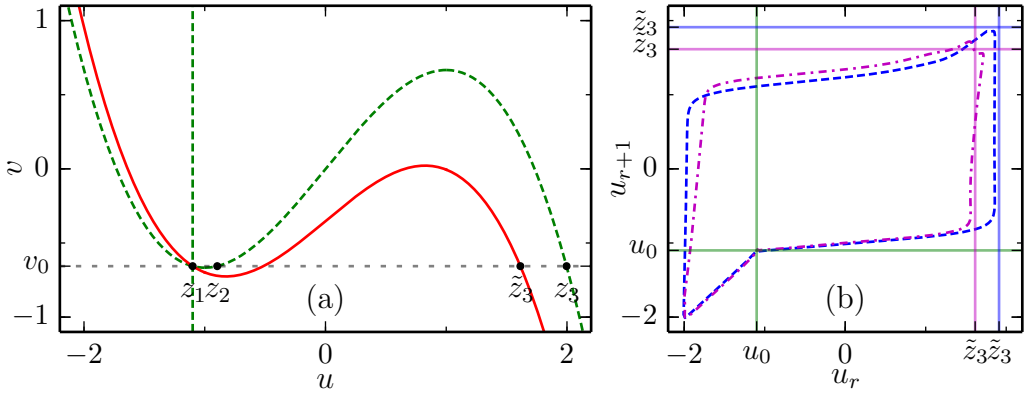

Figure 5.8: Excited values used in the active point approximation. (a) Graph of $v = f(u)$ (green dashed) and $v = \phi(u, D, k)$ (red solid), with $k = 5$ and steady state value v_0 (gray dashed). The intersection points give the values $z_1(v_0)$, $z_2(v_0)$, $\tilde{z}_3(v_0)$ and $z_3(v_0)$ respectively. (b) Lissajous plot for a traveling wave solution obtained from continuation. u_r vs. u_{r+1} for $k = 2$ (blue dashed) and $k = 5$ (magenta dash-dotted). The values $\tilde{z}_3(v_0)$ are marked for $k = 5$ (magenta lines) and $k = 2$ (blue lines). Other parameters: $D = 0.08$, $\varepsilon = 0.02$, $\beta = -1.1$.

the excited value $u^-(v)$, however, because for $k > 2$, the stronger coupling to shell r, which is still close to rest, reduces the excitation value $u^-(v)$, as explained above. For calculating $u^-(v)$, we modify the above ansatz by also taking into account the coupling term of shell $r-1$. Within this coupling term, we approximate the activator value of shell $r-2$ by that of shell $r-1$ and the activator value of shell r by the homogeneous steady state value u_0. Thus, the modified ansatz is

$$\begin{aligned} 0 &= u - \frac{u^3}{3} + D\left(u + (k-1)u_0 - ku\right) \\ &=: \phi(u, D, k) - v\,, \end{aligned} \tag{5.17}$$

with solutions $\tilde{z}_1(v) < \tilde{z}_2(v) < \tilde{z}_3(v)$.

In Fig. 5.8(a) we visualize the construction of the modified approximation to the excitation value. The function $f(u)$ is shown as green dashed lines, whereas the modification $\phi(u, D, k)$ is shown as red solid lines (for the exemplary values $D = 0.08$, $k = 5$. The intersections with the rest value v_0 yield the approximations for the excited values and are annotated. In Fig. 5.8(b), we

compare the solutions provided by Eqs. (5.16) and (5.17) with the excitation values from the numerical simulations using a Lissajous plot. One clearly sees that the modified version Eq. (5.17) predicts the effective excitation value for $k = 5$ much more accurately (solid magenta lines). The unmodified prediction would be located at the position of the blue solid lines independently of k.

The fast subsystem of Eqs. (5.15) is given by Eq. (5.15a) with v as a parameter. The parameter v decides whether that equation has one, two or three steady states. A single steady state (which is automatically stable in this case) means that the active point can become excited and the leading front and thus the wave will propagate, three fixed points (two stable, one unstable) mean that the leading front is pinned and thus the wave fails to propagate, cf. [98, 23]. The value v_{c-} at which there is a saddle-node bifurcation gives the level of inhibitor that separates the realm of one fixed point from that with three. v_{c-} can be calculated (together with the activator value u^*, at which the additional two fixed points coalesce) by defining

$$h(u, v) := f(u) - v + D(\tilde{z}_3(v) + (k-1)z_1(v) - ku) \tag{5.18a}$$

$$h_u(u, v) = f'(u) - Dku \tag{5.18b}$$

and solving

$$h(u^*, v_{c-}) = 0 \tag{5.19a}$$

$$\partial_u h(u^*, v_{c-}) = 0\,. \tag{5.19b}$$

Now, as in [33], we identify two characteristic times for the motion of the active point governed by Eqs. (5.15). t_1 is the time between the successive jumps of two neighboring shells. t_2 is the time it takes for the active point to rise from the initial activator concentration v_0 to the value v_{c-} which would result in pinning of the front. When $t_1 < t_2$, there is not enough time between two successive jumps to allow the inhibitor to raise above the pinning value so that the front is not pinned and thus the pulse can propagate through the tree. When $t_2 < t_1$, the rise of the inhibitor to its pinning value can take place between two jumps so that the front would be pinned and as a consequence, the propagation of the pulse through the tree is not possible.

To approximate t_1 we calculate the saddle-node normal form of $\dot{u} = h(u, v)$

(the fast subsystem of the active point).

$$\dot{x} = a(v - v_{c-}) + bx^2 \qquad x := u - u^* \tag{5.20a}$$

$$a = D\left(\frac{1}{\phi'\left(\tilde{z}_3(v_{c-})\right)} + \frac{k-1}{f'\left(z_1(v_{c-})\right)}\right) - 1 \qquad b = \frac{f''(u^*)}{2}\,, \tag{5.20b}$$

where we have used $0 = d/dv(f(z(v)) - v) = f'(z(v))dz/dv - 1$ and thus $dz/dv = 1/f'(z(v))$ (likewise for ϕ instead f).

The general solution of this differential equation for x is

$$x(t) = \sqrt{\frac{a}{b}(v - v_{c-})}\tan\left(\sqrt{ab(v - v_{c-})}(t - t_0)\right), \tag{5.21}$$

which diverges for $t - t_0 = \pm\frac{\pi}{2\sqrt{ab(v-v_{c-})}}$. We take the difference between these two values as the approximation for the time between two successive jumps as in [99]

$$t_1 \approx \frac{\pi}{\sqrt{ab(v_0 - v_{c-})}}\,. \tag{5.22}$$

The time the inhibitor v needs to raise from v_0 to the pinning value v_{c-} is calculated by integrating the slow subsystem of Eqs. (5.15).

$$t_2 \approx \int_{v_0}^{v_{c-}} \frac{\mathrm{d}v}{\varepsilon(\bar{u} - \beta)},$$

where $\bar{u} \in (z_1(v_0), z_2(v_0))$ is an effective value for the activator during this process, which will be fitted later on.

To calculate the critical degree k_{crit}, we set $t_1 = t_2$ and solve for k (which is hidden in Eq. (5.22) in the coefficient a and in v_{c-}. As the equation obtained by setting $t_1 = t_2$ involves several roots of third order polynomials itself (namely $\tilde{z}_3$ and v_{c-}), this cannot easily been done analytically. However, numerically this is possible and the attained results for the critical degree (in dependence on D) are shown in Fig. 5.7. For these curves, $\bar{u}$ has been adapted such that at D_{min}, the critical degree $k_{\mathrm{crit}} = 2$.

The comparison of Fig. 5.7(a), where $k_{\mathrm{crit}}(D)$ is shown for $\varepsilon = 0.03$ and Fig. 5.7(b), where $k_{\mathrm{crit}}(D)$ is shown for $\varepsilon = 0.04$ clearly indicates an improvement in the prediction of D_{opt} for lower ε, seen by the better agreement of the location of the maxima. This is clear, as splitting Eqs. (5.15) into fast and slow subsystem involves the limit $\varepsilon \to 0$.

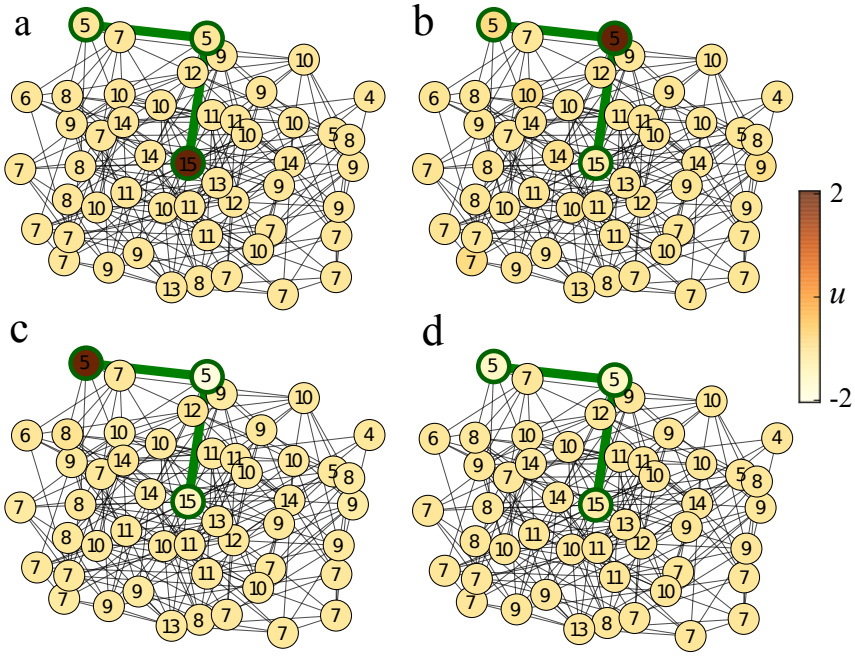

Figure 5.9: Excitation spreading on an Erdős-Rényi random network. Sequence of snapshots (a) Initially, all nodes are at rest, hub node is excited. (b),(c) Excitation spreads to those nodes with $k < k_{\mathrm{crit}}$. (d) Excitation stops before nodes with degree $k > k_{\mathrm{crit}}$. The path of propagation is shown in green and the nodes are labelled with their degree. Parameters: $N = 50$, $\langle k \rangle = 10$, $\varepsilon = 0.02$, $D = 0.04$. Critical degree resulting from those parameters $k_{\mathrm{crit}} = 5.966$. Picture taken from [96].

5.3.3 Application to random networks

The results obtained so far in Sec. 5.3 can also be used for the early stages of excitation spreading on random graphs. As explained in Sec. 2.3.3, large random networks with fixed mean degree $\langle k \rangle$ resemble tree networks locally.

We consider an Erdős-Rényi random network where initially, all nodes are put into the rest state except one node which is put into an excited state. At a early stage of the evolution, the spreading excitation occupies only a few nodes. Thus, the local resemblance to tree networks can be used, meaning that an eventual excitation in a node is most likely triggered by only one excited node. On the other hand, the excitation has to be passed to the rest of the neighboring nodes which are still at rest and the number of which depends on the degree.

We take k_{crit} from the calculation on tree networks to predict the degree of those node at which the excitation stops in an Erdős-Rényi network. In Fig. 5.9 we show simulation results for an Erdős-Rényi network with $N = 50$, $\langle k \rangle = 10$ and parameters of the dynamics $D = 0.04$, $\varepsilon = 0.02$, $\beta = -1.1$. Those parameters give $k_{\mathrm{crit}} = 5.966$ and as we see in Fig. 5.9, the excitation does not reach nodes with a higher degree.

Chapter 6

Excitation waves on minimal small-world networks

In Chapter 5, we studied wave propagation on regular tree networks by mapping those to a modified chain network. This modification turned the chain network into a directed network and the symmetry between two propagation directions was lost. The modified (directed and weighted) network, however, still possessed a shift symmetry (when considering periodic boundary conditions to be precise).

In this chapter, we will study a different modification of the coupling structure of a (undirected, unweighted) ring network. In some sense, this modification is even more genuine to network organized systems, meaning that an analogue continuum system as in Sec. 5.2 for regular trees or in Sec. 4.2.1 for regular rings cannot easily be derived. This modification consists of a single (undirected) additional link, which connects one single pair of nodes in the ring at a certain distance. Including this modification does not break the reversal (clockwise $\leftrightarrow$ counter-clockwise) symmetry of the network but it does break the shift symmetry, because just a single pair of nodes is involved.

The regular ring network with one additional link can be seen as a minimal version of a Newman-Watts small world network (see Sec. 2.3.4). The collective effect of many additional links in a Newman-Watts small-world model on wave propagation is studied in Chapter 7. In the current chapter, we focus on the case of just one additional link in order to study systematically and in detail the effect a shortcut can have on wave propagation. Since the distance of

the additional link is a parameter in the generation of the network, there is no randomness involved in constructing the network and a special attention can be put on the many possible resulting spatio-temporal patterns and the parameter regions in which they occur. A systematic variation analysis becomes possible.

The chapter is structured as follows: In Sec. 6.1 we introduce the model and discuss its symmetries. In Sec. 6.2 we will in detail go through the many different spatio-temporal behaviors that this system shows, explaining the mechanisms and illustrating each type of behavior by Figures of typical timeseries. The examples chosen for this section are loosely in the order of increasing global coupling strength, they are all based on the same ring network, only differing in the coupling strength and the distance of the additional link. In Sec. 6.3 we will present a summarizing Figure which captures all spatio-temporal behavior discussed before. In this Figure the different regions and borders between regions are well visible and explainable. We will investigate the dependence of the position and occurence of the different patterns in this plot on the network size and the coupling range. It is very helpful to treat low (Sec. 6.3.1), high (6.3.2) and intermediate coupling strengths (6.3.3) separately. In Sec. 6.4 we will do some analytical calculations helping the understanding of some transitions in the behavior of this system. The results of this chapter are contained in [100].

6.1 Model and symmetries

We consider an undirected, unweighted ring network of N nodes and coupling range R (see sec. 2.3.1), which is modified by inserting one additional link between one pair of nodes that are a distance $d \in \{R+1, R+2, ..., N/2\}$ apart. Thus, the resulting adjacency matrix is given by that for the ring (Eq. (2.11)) plus the term for the additional link:

$$A_{ij} = \sum_{\mu=1}^{R} (\delta_{i,j+\mu} + \delta_{i,j-\mu}) + \delta_{i,1}\delta_{j,d+1} + \delta_{i,d+1}\delta_{j,1} \ , \tag{6.1}$$

where all indices are to be understood modulo N and $\delta_{i,j}$ is the Kronecker symbol. The additional link in Eq. (6.1) connects nodes 1 and $d+1$ but – by shifting the nodes' labels – any pair of nodes at a distance d can appear as the endpoints of this link.

A scheme of such a network is given in Fig. 6.1 for $N = 25$, $R = 2$ and $d = 8$. Note that reversing the order of the nodes and subsequently shifting the node indices by d maps the network to itself. Moreover, a network with an additional link between nodes 1 and $d \leq N/2 + 1$ can be tranformed to a network with an additional link from node 1 to node $\tilde{d} = N - d > N/2 + 1$ using only the shift symmetry operation. This bijection between networks with distance of additional link d and $\tilde{d}$ is the reason for restricting $d \in \{R{+}1, R{+}2, ..., N/2{+}1\}$.

The dynamics we are studying is again the FitzHugh-Nagumo dynamics (Chap. 3) together with the coupling paradigm provided by Eq. (2.7). Plugging in the coupling matrix Eq. (6.1) the dynamics are given by

$$\dot{u}_i = u_i - \frac{u_i^3}{3} - v_i + D\left[\sum_{\mu=1}^{R}(u_{i+\mu} + u_{i-\mu} - 2u_i) + (\delta_{i,1} - \delta_{i,d+1})(u_{d+1} - u_1)\right] \tag{6.2a}$$

$$\dot{v}_i = \varepsilon(u_i - \beta)\,, \tag{6.2b}$$

again with all indices to be understood modulo N and δ_{ij} being the Kronecker symbol. The parameters β and ε of the dynamics are chosen such that the system is in the excitable regime. We choose them to be $\varepsilon = 0.04$ and $\beta = -1.1$ throughout this chapter. As in Chapter 5, the argument of Sec. 3.3 holds and no Turing instability is present. Thus, the homogeneous steady state $u_i = \beta =: u_0$, $v_i = \beta - \beta^3/3 =: v_0$ is stable.

Apart from the stable homogeneous steady state traveling waves similar to those in Sec. 4.2 are present and the spatio-temporal patterns they generate under the perturbation of the additional link are the subject of Sec. 6.2. Note that generally, any unidirectionally traveling wave solution breaks the symmetry $i \to d - i \bmod N$ (reversing indices and shifting by d) and thus allows us to distinguish the 'first' and 'second' end of the additional link.

Even without the reversal symmetry of the network discussed above, the bijection between networks with additional link distance d and $\tilde{d}$ is still present. In Sec. 6.2.5 we will present a mechanism breaking this symmetry $d \leftrightarrow \tilde{d}$ such that spatio-temporal patterns for networks with link distance d and $\tilde{d}$ are different. We will also present a second mechanism in Secs. 6.2.6 that again reinstalls the symmetry between spatio-temporal patterns for d and $\tilde{d}$.

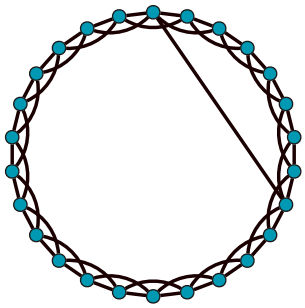

Figure 6.1: Scheme of a network with $N = 26$, $R = 2$, $d = 8$.

6.2 Spatio-temporal patterns

In this section, we systematically go through the emerging patterns, varying d and D. On the regular ring without the additional link, successive mutual excitation of the nodes leads to the emergence of a stable traveling wave. By choosing the initial conditions carefully, a single direction of propagation can be chosen. We choose the initial conditions such that a single excitation wave traveling in direction of ascending node indices is generated.

Depending on the global coupling strength D in Eqs. (6.2), the propagation speed of the wave, as well as the width differ, cf. Sec. 4.2. As discussed in that section, for each combination of N and R, there is a maximal coupling strength, given by $D_{\max} = \frac{N^2}{q(R)L_{\min}^2}$, where $q(R) = R(R+1)(2R+1)/6$. $L_{\min}$ is the minimal domain size allowing stable wave propagation in the limiting reaction-diffusion system, see Sec. 4.2.1 and 4.1.1. $L_{\min}$ only depends on the parameters ε and β and, for our choice of these parameters $\varepsilon = 0.04$ and $\beta = -1.1$, $L_{\min} \approx 30.756$. At this maximal coupling strength, the branch of stable traveling waves is destabilized by a torus bifurcation.

Due to the discrete nature of the system, there is also a minimum value $D_{\min}$ of the coupling strength that only depends on R, ε and β but not on the system size N. At this value, the branch of stable traveling waves meets the branch of unstable traveling waves in a saddle-node bifurcation. This has been discussed in Sec. 4.2.2.

Based on network (6.1), we will examine the effects of one additional link on the traveling wave of the regular ring, thereby varying the coupling strength D between $D_{\min}$ and $D_{\max}$. d will be varied between $R+1$ and $N-(R+1)$. Values above $N/2+1$ result in different spatio-temporal patterns only in a

R	$D_{\min}$	D_1	D_{2-}	D_2
1	0.0324	0.0339	0.0359	
2	0.0233	0.0235	0.0481	
3	0.0169	0.0170	0.0238	0.5890

Table 6.1: Approximate transition values $D_{\min}$, D_1 and D_2 (and D_{2-}) for different coupling ranges R. Parameters: $\varepsilon = 0.04$, $\beta = -1.1$.

certain range of the coupling strength D. Above a certain D, a mechanism we termed *shortcut blocking* is active for all distances d and the spatio-temporal patterns are (to very good approximation) the same.

As initial conditions, we choose the snapshot of a stable traveling wave on the regular ring at the respective coupling strength D with the peak before the first end of the additional link. We then numerically integrate the initial value problem for the system including the additional link. We use a Runge-Kutta Fehlberg 4(5) scheme with adaptive stepsize. Note that the correspondence between networks with d and $\tilde{d}$ can be viewed as the correspondence between the initial wavepeak located before the first and before the second end of the additional link in a network with distance d.

A traveling wave solution on the network without the additional link is a periodic solution that has a well-defined period $T_0(D)$. In the following, we discuss changes of this periodic solution for networks including the additional link. In short, we observe either (a) an ongoing spatio-temporal activity or (b) relaxation into the stable homogeneous fixed point (propagation failure). In almost all cases where ongoing spatio-temporal activity emerges, we were able to measure the period of the emerging solution T_d, where d is the distance which the additional link spans. To quantify the spatio-temporal behavior of these solutions we measure the relative period defined by

$$\vartheta_d(D) := T_d(D)/T_0(D)\,. \tag{6.3}$$

We will present examples for typical spatio-temporal patterns that we observed. For all the examples, we consider $N = 150$ and $R = 2$ which yields $D_{\max} \approx 4.75$ and $D_{\min} \approx 0.0233$. The examples for different spatio-temporal behavior will be presented more or less in an order of ascending D, starting with low values of D. In the plots of these timeseries we shift the indices of

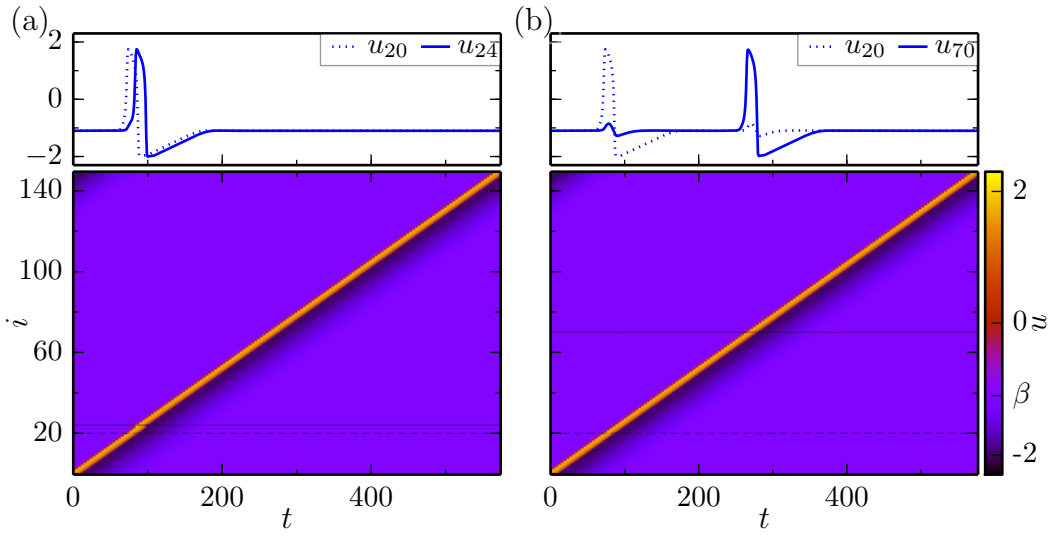

Figure 6.2: Color-coded activator level $u_i(t)$ as space-time plot and time-series of activator and inhibitor levels at both ends of the additional link, marked by horizontal lines in the space-time plot. Timespan is one period of a traveling wave solution of Eqs. (6.2) for (a) $D = 0.03$, $d = 4$, resulting period $T_4(0.03) = 574.0$ ($\vartheta_4(0.03) = 0.996$) and (b) $D = 0.03$, $d = 50$, resulting period $T_{50}(0.03) = 577.2$ ($\vartheta_{50}(0.03) = 1.001$). Other parameters: $N = 150$, $R = 2$, $\beta = -1.1$, $\varepsilon = 0.04$.

the network such that the additional link's endpoints are not placed right at the edge of the space-time. Next we will discuss the observed scenarios and then combine our findings in a plot of $\vartheta_d(D)$ (Fig. 6.9).

6.2.1 Unperturbed wave

If the additional link covers a distance that is only slightly larger than the coupling range of the regular ring, i.e. $d \gtrsim R$, it has no significant influence on the traveling wave. An example for this case is shown in Fig. 6.2(a) for a coupling strength $D = 0.03$ and link distance $d = 4$. The additional link has the effect that the excitation is passed somewhat more quickly between its end nodes. Because this is happening only in a small portion of the ring and the additional link has no influence on wave propagation elsewhere, this effect has no significant influence on the relative period. For the unperturbed wave we measured $T_0(0.03) = 576.2$ and for $d = 4$, $T_4(0.03) = 574.0$, resulting in

$\vartheta_4(0.03) = 0.996$.

As another example, we consider the solution for the network with an additional link with $d = 50$ between nodes 20 and 70 and $D = 0.03$ in Fig. 6.2(b). In the timeseries of u_{20} and u_{70}, we see that the wave triggers a small subthreshold excitation at the respective other node. The additional coupling to a node far away and therefore at rest (for this small value of D), somewhat slows down the transition to excitation and thus increases the period a little. $T_0(0.03) = 576.2$ and $T_{50}(0.03) = 577.2$ so that $\vartheta_{50}(0.03) = 1.001$. Again, the effect on the relative period is so small that –compared to other effects the additional link can have– we consider this as an unperturbed wave propagation.

6.2.2 Propagation failure I — low coupling strength, direct failure

At very low coupling strengths, the propagation takes place in a saltatory way (see Sec. 4.2.2) and the excited part of the wave (u significantly larger than u_0) occupies only a few nodes. Thus, when the wave arrives at the first end of the additional link, the second end will always point to a node in –or very close to– the rest state. The saltatory type of propagation and the small wave width present at coupling strengths this low can be seen in Fig. 6.3.

When the coupling strength D is below a certain value $D_1(R)$, this additional coupling term to a node at rest will lead to propagation failure. The chain of events is as follows: The node at the first end of the additional link is prevented to reach full excitation height. The following node will be transitioning to excitation a little retarded. This continues and the times between the excitation peaks of the subsequent node becomes larger until, a few nodes after the first link endpoint, propagation fails.

This mechanism is depicted in Fig. 6.3(a) for $D = 0.0234$ and $d = 10$. It has also been described in the context of coupling strengths below $D_{\min}$ in Ref. [34]. In our case however, the coupling strength is above $D_{\min}$ but the perturbation exerted by passing a node with a link to a node at rest triggers the same chain of events. We determined the values of $D_1(R)$ by numerical simulation for $R = 1, 2, 3$. They are listed in Table 6.1.

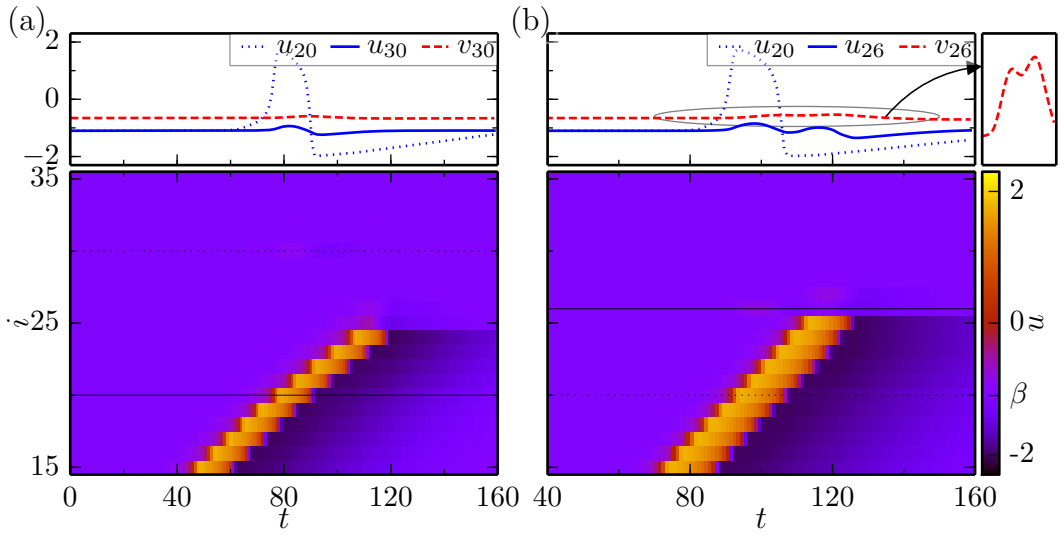

Figure 6.3: Color-coded activator level $u_i(t)$ as space-time plot and timeseries of activator and inhibitor levels at both ends of the additional link, marked by horizontal lines in the space-time plot. Timespan is one period of a traveling wave solution of Eqs. (6.2) for (a) $D = 0.0234$, $d = 10$, resulting in direct failure and (b) $D = 0.03$, $d = 6$, resulting in inhibitor-mediated failure. In the very upper right, a blow-up of v_{30} for the encircled region is shown. Other parameters as in Fig. 6.2.

6.2.3 Propagation failure II — low coupling strength, inhibitor-mediated failure

When the coupling strength D exceeds $D_1(R)$ but is no larger than a second threshold value $D_2(R)$, propagation failure can still occur. In this case the mechanism is different and failure does not occur at any distance d that the additional link spans.

When the wave passes the node at the first end of the additional link, the high activator level will cause an excitation at the other end of it. For D below $D_2(R)$ (determined numerically and listed in Table 6.1), this excitation stays sub-threshold and does not lead to an excitation of a secondary wave. Nevertheless, the sub-threshold excitation does lead to a rise in inhibitor level at the node at the second end of the additional link. If the distance, the link spans is small enough such that the wave arrives at the other end, when the inhibitor is still elevated, the wave will terminate. This mechanism is shown

in Fig. 6.3(b) for $D = 0.03$ and $d = 6$. If the distance is larger, the inhibitor level will have relaxed enough to let the wave pass, in this case the additional link exerts no significant influence (cf. Sec. 6.2.1 and Fig. 6.2(b)). Note that in the examples of Figs. 6.2(a),(b) and Fig. 6.3(b), the coupling strength D is the same and the outcome only depends on the distance d.

The condition $D < D_2(R)$ is just a necessary condition for inhibitor-mediated failure to be present. The node at which the additional link ends has $2R$ links to its neighbors on the ring which are in the unexcited state, counteracting any excitation triggered through the additional link. Thus, when R is too large, the sub-threshold excitation can be too weak to leave the inhibitor level raised sufficiently for propagation failure. We observed that the end of the region of inhibitor-mediated failure and the beginning of the region of secondary wave pair generation fall together for $R = 1$ and $R = 2$. For higher R, the region of inhibitor-mediated failure ends before the region of secondary wave pair generation begins. For $R = 3$ we termed the coupling strength that marks the end of the region of inhibitor-mediated failure D_{2-}. This value is listed separately in Table 6.1.

6.2.4 Period decreasing

A coupling strength exceeding the threshold value $D_2(R)$ allows the triggering of a super-threshold excitation via the additional link. In principle, such an excitation always leads to the generation of a pair of excitation waves traveling in opposite directions at the second end of the link. One wave of this pair travels in the opposite direction, towards the original wave and at some point both collide and annihilate each other. The other part of this pair continues traveling along the network until it again reaches the node at the first end of the link and the pattern repeats.

Because the duration of the pattern is determined by the time it takes that half of the secondary wave pair which travels in the same direction as the original wave to reach the first link end, starting from the second, the wave effectively skips the part between first and second end, taking a shortcut through the additional link. In the part that the wave skipped, the two counterpropagating pulses annihilate. Thus, this pattern leads to a decrease of the effective size of the regular ring by approximately d. As a consequence,

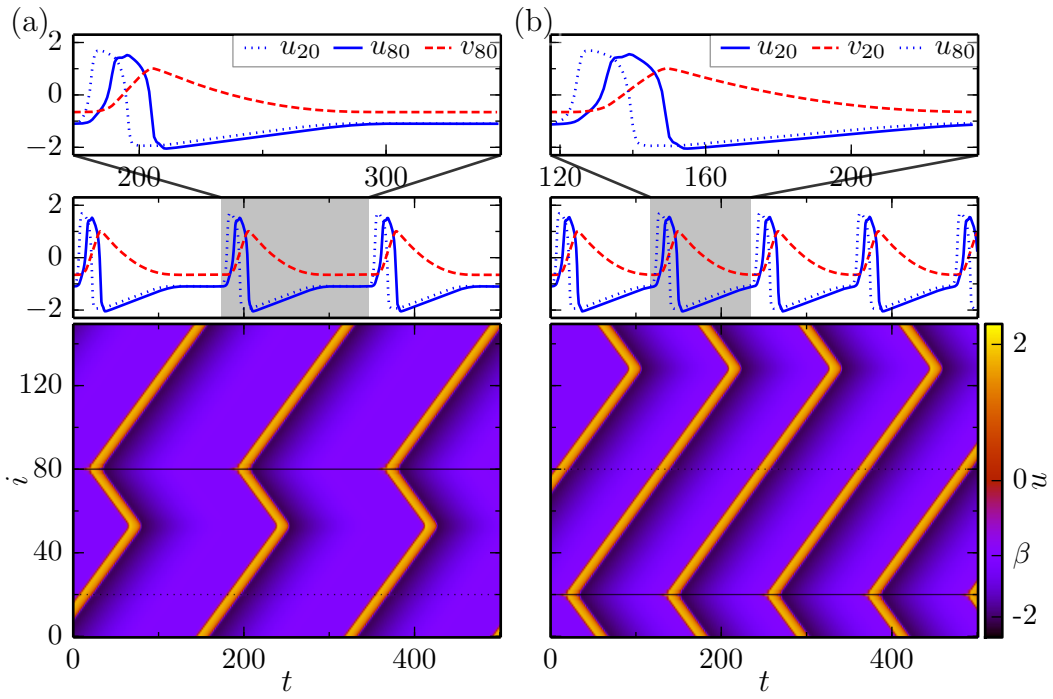

Figure 6.4: Color-coded activator level $u_i(t)$ as space-time plot and timeseries of activator and inhibitor levels at both ends of the additional link, marked by horizontal lines in the space-time plot. (a) $D = 0.08$, $d = 60$, initial wave peak placed in the large part of the ring, leading to annihilation in the small part of the ring, resulting period $T_{60}(0.08) = 173.24$ ($\vartheta_{60}(0.08) = 0.64$) and (b) $D = 0.08$, $d = 60$, initial wave peak placed in the small part of the ring, leading to annihilation in the large part of the ring, resulting period $T_{90}(0.08) = 117.41$ ($\vartheta_{90}(0.08) = 0.43$). ($T_{90}$ instead of T_{60} because of the convention adopted in Sec. 6.2.4.) Top panels show one period, middle and bottom panels show same absolute timespan for both (a) and (b). Other parameters as in Fig. 6.2.

the larger d becomes, the smaller becomes $\vartheta_d(D)$ and approximately we have $\vartheta_d(D) \approx 1 - d/N$. The actual $\vartheta_d(D)$ will be a little larger because it takes a little longer to trigger the excitation in the node at the second end of the shortcut, as (a) a wave pair is triggered and thus more nodes are needed to be brought to excitaion and (b) the excitation in the remote node is triggered by only one link whereas that in the neighboring nodes on the ring is triggered through two links (because $R = 2$).

In Fig. 6.4(a), period decreasing is shown at $D = 0.08$ and $d = 60$. With

those values, $1 - d/N = 1 - \frac{60}{150} = 0.6$. The measured period is $T_{60}(0.08) = 173.24$ and thus $\vartheta_{60}(0.08) = 0.64$.

6.2.5 Bistability and symmetry breaking

Linked to the phenomenon of period decreasing is the breaking of the bijection symmetry between networks with distance d and $\tilde{d} = N - d$.

When different initial conditions from the ones mentioned above are chosen in a network with distance d, namely when the peak of the wave is placed before the second end of the additional link, the part where the counterpropagating waves annihilate comprises $N - d$ nodes instead of d thus making the part that the wave effectively skips larger and thus $\vartheta_d(D) \approx 1 - \frac{N-d}{d} = \frac{d}{N} < 1 - \frac{d}{N}$.

An example for this behavior is shown in Fig. 6.4(b). In that example, we chose $d = 60$, $\kappa = 0.08$ and chose the initial conditions with the wavepeak before the second link end. By the approximation above, we expect $\frac{d}{N} = \frac{60}{150} = 0.4$ as a value for the relative period. As mentioned at the beginning of Sec. 6.2, this can also be viewed as a network with distance $\tilde{d}$ ($\tilde{d} = 150 - 60 = 90$ in this case) with the wavepeak before the first end of the shortcut. From now on we adopt the convention that in this situation we will use that distance of d and $\tilde{d}$ for which the wavepeak is placed before the first end of the additional link. With $\vartheta_{90}(0.08) = 0.43$ ($T_{90}(0.08) = 117.41$), the numerically measured value for the relative period is again a bit larger than the approximated one for the same reasons explained in Sec. 6.2.4.

6.2.6 Shortcut blocking

After undergoing an excitation, a node is left with increased inhibitor level. The node's state is then governed by the slow dynamics of the inhibitor Eq. (4.7b) and it gradually relaxes back to the steady state value. All nodes that are in this state, slowly relaxing back to the steady state form the so-called refractory tail of the wave.

When the inhibitor level at the other end of the additional link exceeds a certain critical value, the triggering of a super-threshold excitation through the additional link is not possible. Thus the generation of secondary wave pairs can be prevented by the refractory tail when it extends back to the

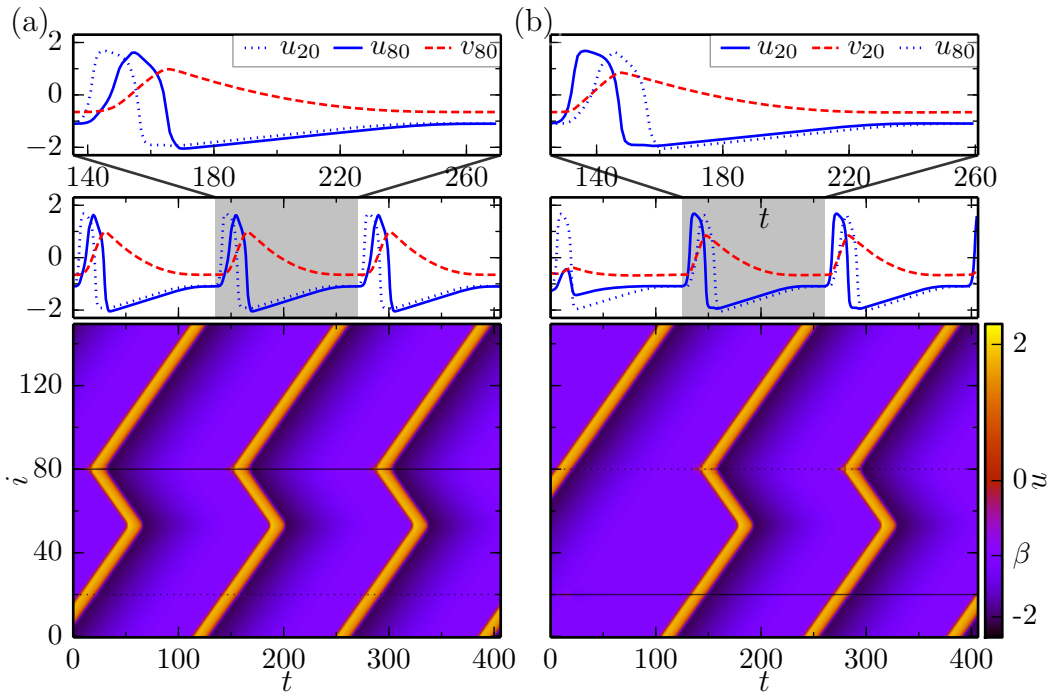

Figure 6.5: Color-coded activator level $u_i(t)$ as space-time plot and timeseries of activator and inhibitor levels at both ends of the additional link, marked by horizontal lines in the space-time plot. (a) $D = 0.12$, $d = 60$, initial wave peak placed in the large part of the ring and (b) $D = 0.12$, $d = 60$, initial wave peak placed in the small part of the ring. Differently from the situation in Fig. 6.4, the secondary wave pair is always triggered at the same end of the additional link, after transients are gone. Both solutions have the same period $T_{60}(0.12) = 135.42$ ($\vartheta_{60}(0.12) = 0.65$). Top panels show one period of each solution, middle and bottom panels show same absolute timespan for both (a) and (b). Other parameters as in Fig. 6.2.

other end of the additional link. We call this phenomenon *shortcut blocking*. Because during relaxation in the tail of the wave, the critical inhibitor level is undercut at a well defined point, the distance between this point and the leading front of the wave provides a maximum distance for shortcut blocking. For an analytic calculation to determine the critical value of the inhibitor and the critical distance see Sec. 6.4.1.

When shortcut blocking occurs for the link distance d but not for the link distance $N - d$, the resulting pattern will be the same in both cases (after transients are gone). Thus, the bistability between the two distances is lifted

and therefore the symmetry is recovered. An example for this behavior is given in Fig. 6.5.

Evaluating all link distances (up to $N-R$), one can see this phenomenon at a fixed value of D as a sudden transition of $\vartheta_d(D)$ in d. Say that for a distance d, shortcut blocking takes place and for $d+1$ no shortcut blocking takes place. Thus

$$\vartheta_d(D) = \vartheta_{N-d}(D)$$
$$\vartheta_{d+1}(D) > \vartheta_{N-(d+1)}(D)\,.$$

Then, when increasing the distance from $N-(d+1)$ to $N-d$, the relative period will change from $\vartheta_{N-(d+1)}(D) \approx (d+1)/N$ to $\vartheta_{N-d} = \vartheta_d(D) \approx 1-d/N$.

Note also, that the refractory tail becomes larger as D increases and thus the transition happens at lower values of d (because the refractory tail has to bridge $N-d$ nodes). Therefore, the point of transition can be regarded as a measure of the size of the wave. It can directly be read off in Fig. 6.9, where the relative period for all link distances (up to $N-R$) is evaluated.

For values of D, higher than a certain threshold, at which the critical distance for shortcut blocking is $N/2$, period decreasing can not happen anymore. However, other interesting phenomena start to occur.

6.2.7 Period multiplication, complex behavior

For some network configurations (N, R) there can be complex behavior for certain values of d and D. The relative period suddenly transitions to integer multiples of its previous value when d or D is changed. This means that the spatio-temporal pattern will repeat only after multiple passages of the wave through a fixed node.

We have exemplarily chosen a period-2 and a period-5 solution in Fig. 6.6 to illustrate this type of behavior. This behavior always takes place for coupling strengths D such that the wave size with respect to shortcut blocking is larger than $N/2$. Thus, wave pair generation at the first end of the additional link (when $d < N/2$) will always be blocked.

These solutions can be regarded as an interplay between shortcut blocking of the second link end and secondary wave pair generation. We found that the inhibitor level at the second end of the additional link –especially at the times

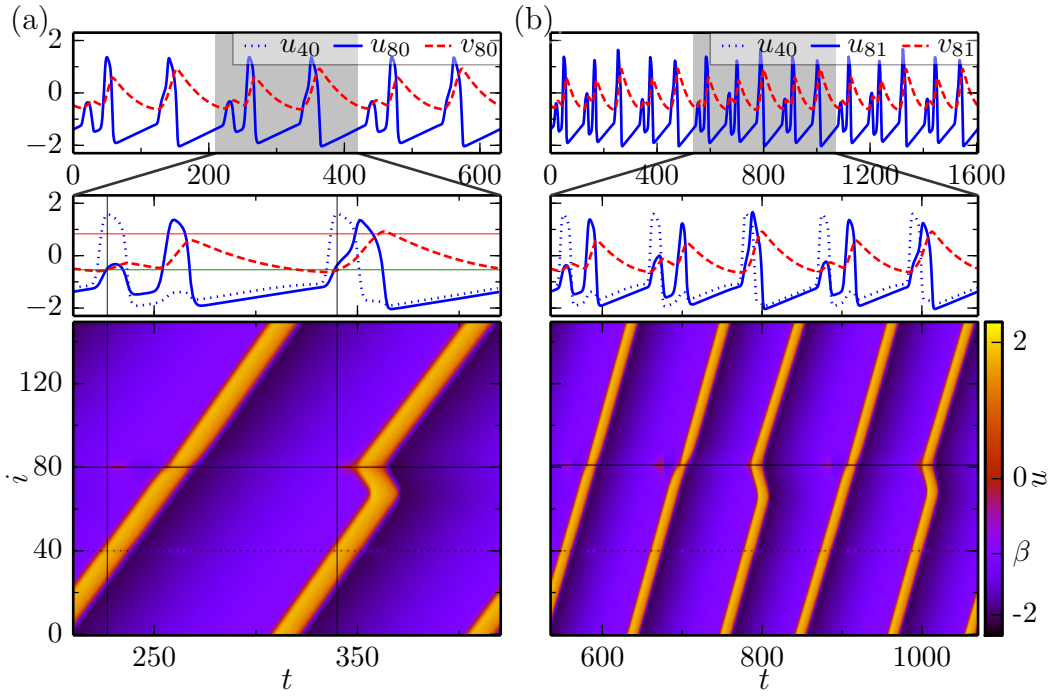

Figure 6.6: Color-coded activator level $u_i(t)$ as space-time plot and timeseries of activator and inhibitor levels at both ends of the additional link, marked by horizontal lines in the space-time plot. (a) $D = 0.37$, $d = 40$, with resulting period-2 solution, $T_{40}(0.37) = 210.2$ ($\vartheta_{40}(0.37) = 1.92$) and (b) $D = 0.37$, $d = 41$, with resulting period-5 solution, $T_{41}(0.37) = 535.2$ ($\vartheta_{41}(0.37) = 4.89$). Top panels show three full periods, middle and bottom panels show one period. In the middle panel of (a) are marked by lines: Times of peak values of u_{40} (gray), v_{80} at the first of these times (green), usual maximum inhibitor level when the wave passes through a node regularly (red). Detailed description in Sec. 6.2.7. Other parameters as in Fig. 6.2.

when the activator at the first end reaches the maximum value– plays a key role in understanding the behavior.

In the period-2 example of Fig. 6.6(a), the sequence of events is as follows: (a) Shortcut blocking, no secondary wave pair but a sub-threshold excitation is triggered at second end of the additional link. (b) The wave regularly arrives at the second end of the link, the peak is a little smaller compared to other nodes because the inhibitor level is still a little raised from the subthreshold-excitation. (c) For that reason, the inhibitor here does not rise as much as it would normally during wave passage. (d) The wave again arrives at the

first end of the shortcut. Because the inhibitor level at the second end has not reached the usual maximum level when the wave passed through and has deayed since, shortcut blocking does not happen this time. (e) A secondary wave pair is triggered at the second end of the node. Now the inhibitor level at this end of the additional link rises even a little above the usual maximum level. The reason is that the triggering of the secondary wave pair took place through only one link as compared to two local links ($R = 2$), so $\dot{v} > 0$ for a longer time than usually (at the second link end). (f) One half of the pair cancels out with the original wave, the other keeps on traveling until it reaches the first end of the additional link again and the pattern repeats.

A similar but more complicated chain of events leads to the period-5 behavior also shown in Fig. 6.6(b). Other periods (3,4,6,...) have also been observed in our simulations.

6.2.8 Propagation failure III — intermediate coupling strength, complex mechanisms

In those parameter ranges of d and D where we observed period multiplication behavior, regions of propagation failure are always close. The chain of events leading to propagation failure in this parameter regime however is more complex than that of Secs. 6.2.2 and 6.2.3.

In the region of period multiplication, the coupling strength is such that the wave size with respect to shortcut blocking is larger than $N/2$. Thus, the first end of the additional link is always blocked and the failure always happens at the second end.

Similar to the case of inhibitor-mediated failure for very small coupling strengths (Sec. 6.2.3) and period multiplication (Sec. 6.2.7), the inhibitor level at the second end of the additional link plays a key role. For propagation failure in this parameter region, the wave will make several passages with chain of events similar as in Sec. 6.2.7. The pattern however will not repeat, because at one point, the inhibitor concentration at the second link end rises to a level that not only the triggering of a secondary wave pair but even the passing through of the wave when it reaches there regularly is prevented. Thus, wave propagation terminates at the second link end and the entire system relaxes

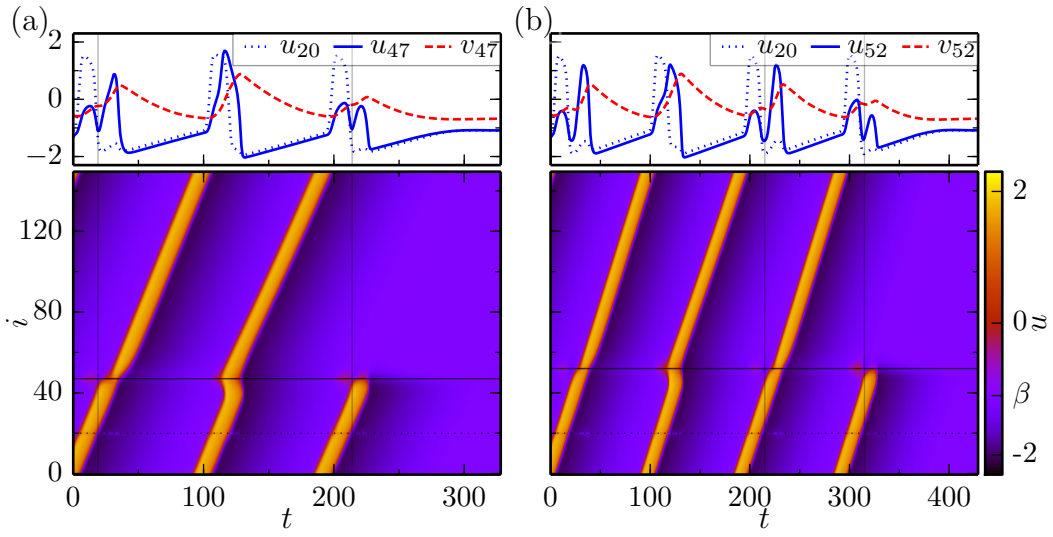

Figure 6.7: Color-coded activator level $u_i(t)$ as space-time plot and time-series of activator and inhibitor levels at both ends of the additional link, marked by horizontal lines in the space-time plot. (a) $D = 0.5$, $d = 27$. (b) $D = 0.5$, $d = 32$. In (a) and (b), vertical lines mark selected timepoints at which u_{20} has reached a minimum after a full excitation. (see Sec. 6.2.8 for further explanations.) Both solutions are examples for complex mechanisms of propagation failure at an intermediate value of the coupling strength D. cf. Sec. 6.2.8 for more details. Other parameters as in Fig. 6.2.

into the stable homogeneous state.

In Fig. 6.7(a), $D = 0.5$ and $d = 27$. There, two passages of the wave through the node of the second link end are completed and the third time the wave arrives there, it terminates. The difference in inhibitor level causing the different outcomes is minute and not to be seen directly in Fig. 6.7(a). To quantify this, we measured the inhibitor level at the node of the second link end ($i = 47$) at those timepoints when the activator level at the first link end has reached its minimum after a full excitation. We did this for both full excitations that trigger a sub-threshold excitation at the second link end, terming these timepoints t_1 and t_2. Both timepoints are marked by vertical lines in Fig. 6.7(a). The inhibitor values at the second link end at these timepoints are $v_{47}(t_1) = -0.23$ and $v_{47}(t_2) = -0.19$, showing the second value to be indeed a little higher than the first one.

In Fig. 6.7(b), $D = 0.5$ and $d = 32$. In this case, it takes two sub-threshold

excitations after one super-threshold excitation at the second link until the inhibitor reaches a critical value to quench propagation at this point. Again we measured the inhibitor values at the node of the second link end ($i = 52$) at the same timepoint as above for the last two full excitations (t_1 and t_2) at the first link, which trigger a sub-threshold excitation at the second link end. The results are $v_{52}(t_1) = -0.344$ and $v_{52}(t_2) = -0.174$, also showing the second value to be larger.

We summarize by stating that also this mechanism of propagation failure is inhibitor-mediated. However, the chain of events leading to an inhibitor level sufficient for propagation failure is usually more complicated than in the simple case of Sec. 6.2.3.

6.2.9 Propagation failure IV

If the coupling strength D gets close to the maximum value $D_{\max} \approx 4.75$, we will find propagation failure for the majority of values of d. In this regime we find two mechanisms of propagation failure similar to the case of very low D but for different reasons.

Firstly, shortcut blocking is active in this region of the coupling strength D, therefore no secondary wave pairs are excited at all. If the coupling strength is very high, the excited part of the wave occupies many nodes. For the inhibitor, there is not enough time/space to relax completely to the rest value as in the case of low coupling strengths. Thus, during wave propagation, the inhibitor level is above the rest value everywhere on the ring, making the wave more vulnerable.

Inhibitor-mediated failure at high coupling strengths D is shown in Fig. 6.8(a). There, by a sub-threshold excitation triggered through the additional link, the inhibitor level at the second link end becomes more elevated. It cannot decay enough before the wave arrives and thus, wave propagation terminates at this point. Similar to the low-D case, this mechanism is dependent on the distance d of the additional link because a longer distance leads to more time between the sub-threshold excitation and the arrival of the wave at the second link end.

When D comes even closer to the maximum value, the backcoupling to an unexcited node is enough to suppress propagation. An example for this type of propagation failure is shown in Fig. 6.8(b). The wave will fail to propagate

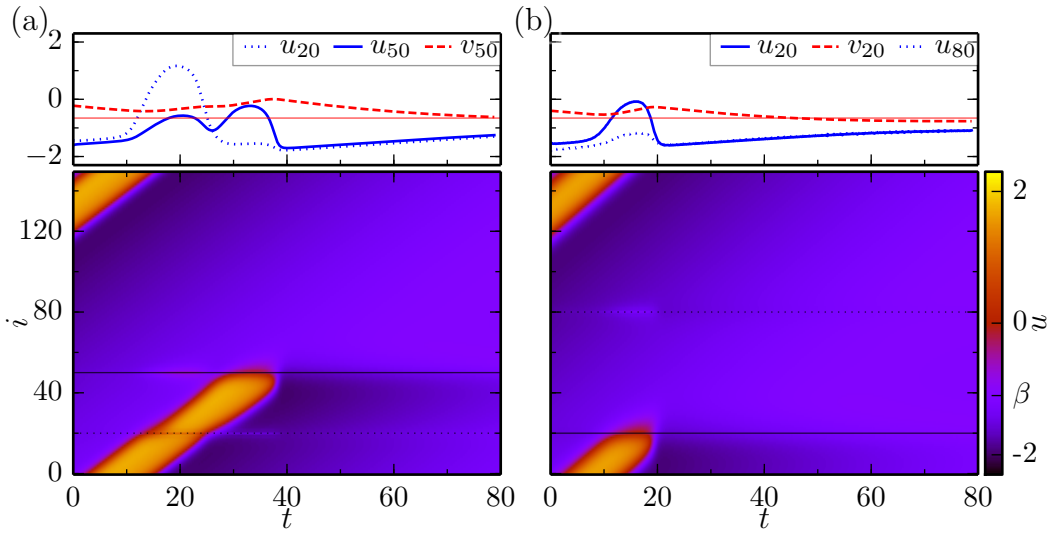

Figure 6.8: Color-coded activator level $u_i(t)$ as space-time plot and timeseries of activator and inhibitor levels at both ends of the additional link, marked by horizontal lines in the space-time plot. (a) $D = 1.5$, $d = 30$ and (b) $D = 3.0$, $d = 60$. Both solutions are examples for quenched propagation at high values of the coupling strength D. Inhibitor-mediated failure is present in (a), direct failure in (b). Marked with a thin solid red line in the top panel of (a) and (b) is the steady state value of the inhibitor. Other parameters as in Fig. 6.2.

at the first end of the additional link that is reached by the wave. Here, no dependence on d is present except that it needs to be larger than the width of the excited part of the wave. Note that the inhibitor value at the first link end seems to go below its steady state value in Fig. 6.8(b). This is because the stable homogeneous state is a focus and thus the steady state value of both activator and inhibitor will be under- and overshot during the relaxation process.

We also observed solutions that show quenched propagation by an intermediate form of these two mechanisms. Moreover, in inhibitor-mediated failure in this regime of D there are also solutions with suppressed propagation in which the inhibitor level at the second end of the link builds up over several periods of the wave until the propagation is quenched.

6.3 Phase diagrams and scaling laws

As already mentioned in Sec. 6.2, the solutions on the minimal small-world network either decay to the stable homogeneous state or show ongoing spatio-temporal activity with a well defined period $T_d(D)$. In Sec. 6.2 we defined the relative period as $\vartheta_d(D) \equiv T_d(D)/T_0(D)$, where $T_0(D)$ is the period that a traveling pulse on the regular ring shows for coupling strength D. From the relative period we can directly infer the influence that the additional link with a distance d has. In order to capture all observed spatio-temporal behavior in one quantity, we assign the value -1 to the relative period, when wave propagation is quenched, or mark the plot of $\vartheta_d(D)$ with a special color at these points.

A density plot of $\vartheta_d(D)$ for fixed N and R summarizes the occurence of the spatio-temporal phenomena described in Sec. 6.2 very clearly. For $N = 150$ and $R = 2$, such a plot is shown in Fig. 6.9. In this plot, regions of propagation failure are marked black. The parameter values (d, D) of the examples discussed in Sec. 6.2 are marked by roman numbers. The parameter regions for all phenomena can be identified in this plot, we discuss them shortly. (a) Unperturbed wave propagation occurs where this density plot is blue, indicating a value $\vartheta_d(D) \approx 1$. In some regions the transition from unperturbed to other behavior is abrupt in other regions it is smooth. (b) Direct failure occurs for a very narrow region between $D_{\min} = 0.0233$ and $D_1 = 0.0235$ (see Table 6.1). It is seen in Fig. 6.9 as a very thin black stripe at the lower border. (c) Indirect failure is seen as the horn-like black structures at the lower boundary. They are almost perfectly mirror symmetric to each other. The cause of the slight asymmetry is that for large d, the second link end is located within the tail of the wave and therefore the activator value at this link end is a little lower than the rest value, thus exerting a stronger backcoupling to the first link end leading to direct failure. (d) The value D_2 above which the generation of secondary wave pairs takes place appears as the sudden transition from the unperturbed region at low D to the region that increasingly becomes red with increasing D. The red regions around $d \approx 40$ and $d \approx 110$ that undercut this value of D_2 slightly can be understood as follows: In the tail of the wave, the coupling term can be neglected for the relaxation process. The stable steady

state of the local dynamics is a focus and thus, during the relaxation process, the inhibitor undershoots its rest value at some points. If d is such that the triggering of an excitation through the additional link coincides with this undershoot at the second link end, a secondary wave pair can be generated despite D being below D_2. (e) Period decrease and shortcut blocking is seen as the region that increasingly becomes red with increasing d between $D \approx 0.05$ and $D \approx 0.2$. (f) Shortcut blocking manifests itself by a sudden transition of $\vartheta_d(D)$, appearing as a transition from deep red to more blueish red in the lower right half of Fig. 6.9. (g) Period multiplication and complicated mechanisms of propagation failure appear as the green, purple orange and black regions at intermediate values of D. (h) Inhibitor mediated failure at high coupling strengths is present in the black regions that seem to grow out of the large black region at the top. (i) This in turn marks the region of direct failure at high coupling strengths.

Apart from some slight asymetries discussed above, this diagram is almost perfectly mirror symmetric with respect to d. From now on we use the term 'phase diagram' for a density plot of $\vartheta_d(D)$ at fixed values of N and R. Note that the diagram Fig. 6.9 extends over $d \in \{k+1, ..., N-(k+1)\}$. Thus, by the shift symmetry discussed in Sec. 6.1, the asymmetry between d and $\tilde{d} = N - d$ can be reagarded as due to different initial conditions for the same d.

Next, we are interested in the influence of N and R on the behavior of the system. To this end we examine the appearance of phase diagrams at different values for N and R. We can identify three coarse regions of the coupling strength D in the phase diagram that have different scaling properties with respect to N and R.

6.3.1 Low coupling strength

When the coupling strength D is very small, the propagation takes place in a saltatory way, meaning that the maximum number of nodes that are transitioning from rest to excited one instance of time is one. In this regime of D –provided that N is large enough– we observe no dispersion effects, where the wave reaches nodes again before they have relaxed into the steady state.

The main effects of the additional link in this regime are direct failure and

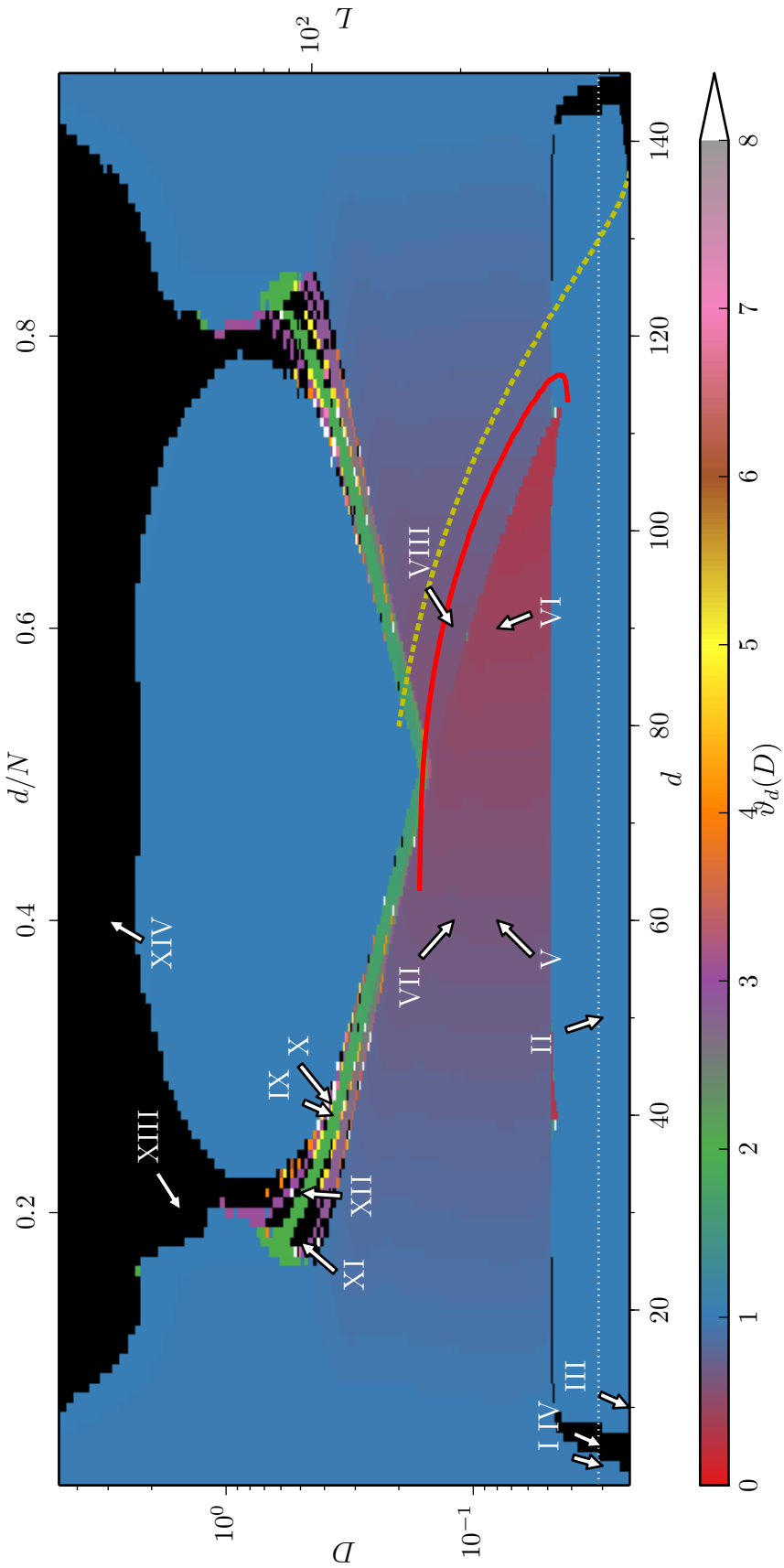

Figure 6.9: Color-coded $\vartheta_d(D)$ in the (d, D) plane. Right and upper axis show L and d/N as units of measurement. Black regions indicate propagation failure. Yellow dashed line shows analytic approximation to wavewidth without corrections, red solid line shows analytic approximation to wavewidth including corrections (cf. Sec. 6.4.1). The white dotted line gives the analytically estimated value for D_2 (cf.Sec. 6.4.2). For the points marked by an arrow, timeseries are shown: I,II: Fig. 6.2(a,b), III,IV: Fig. 6.3(a,b), V,VI: Fig. 6.4(a,b), VII,VIII: Fig. 6.5(a,b), IX,X: Fig. 6.6(a,b), XI,XII: Fig. 6.7(a,b), XIII,XIV: Fig. 6.8(a,b). Other parameters as in Fig. 6.2.

inhibitor-mediated failure (cf. Secs. 6.2.2 and 6.2.3, Fig. 6.3 and points III and IV in Fig. 6.9). These effects are purely local in the sense that the size N of the network has no influence on the values of d and D where these phenomena occur. The values $D_{\min}$ below which no wave propagation even on the regular ring is possible, D_1 below which any distance $d > 0$ of the additional link leads to (direct) failure and D_2 below which certain link distances d lead to (inhibitor mediated) failure and above which the generation of secondary wave pairs becomes possible are shown in Table 6.1.

The coupling range R does have an influence on the values $D_{\min}$, D_1 and D_2. Currently we do not have a good understanding of this influence and must content ourselves with measuring these values numerically.

In Fig. 6.10, we show six phase diagrams for increasing values of N and a fixed value of $R = 2$. The scaling behavior at low values of the coupling strength D can be verified by observing that the D and d values of the regions of inhibitor-mediated failure (Sec. 6.2.3) in the lower left of each panel stay the same to very good approximation.

6.3.2 High coupling strength

At high values of the coupling strength D, the propagation takes place in a continuous fashion, meaning that at one instance of time, many nodes are in the transition phase to (and from) the excited state. Moreover, for the highest values of D, dispersion effects are playing a role, as e.g. described in Sec. 6.2.9.

For this reason it is advantageous to take the viewpoint of the continuum limit discussed in Sec. 4.2.1, Eqs. (4.10). In this limit, the system on the regular ring, (Eq. (6.2) without the term of the additional link) becomes a continuous reaction-diffusion system with periodic boundary conditions and domain size $L = N/\sqrt{q(R)D}$, where $q(R) = 1/6R(R+1)(2R+1)$ as explained in Sec. 4.2.1. By viewing a finite regular ring as the discretization of such a reaction-diffusion system, we can use d/N instead of d and L instead of the coupling strength D as quantities to compare networks with different N and R at high coupling strengths.

Comparing the L and d/N values of the region of inhibitor mediated failure at high D, we observe that these stay approximately constant. The L and d/N values (shown on right and upper axis) for the left border of the direct failure

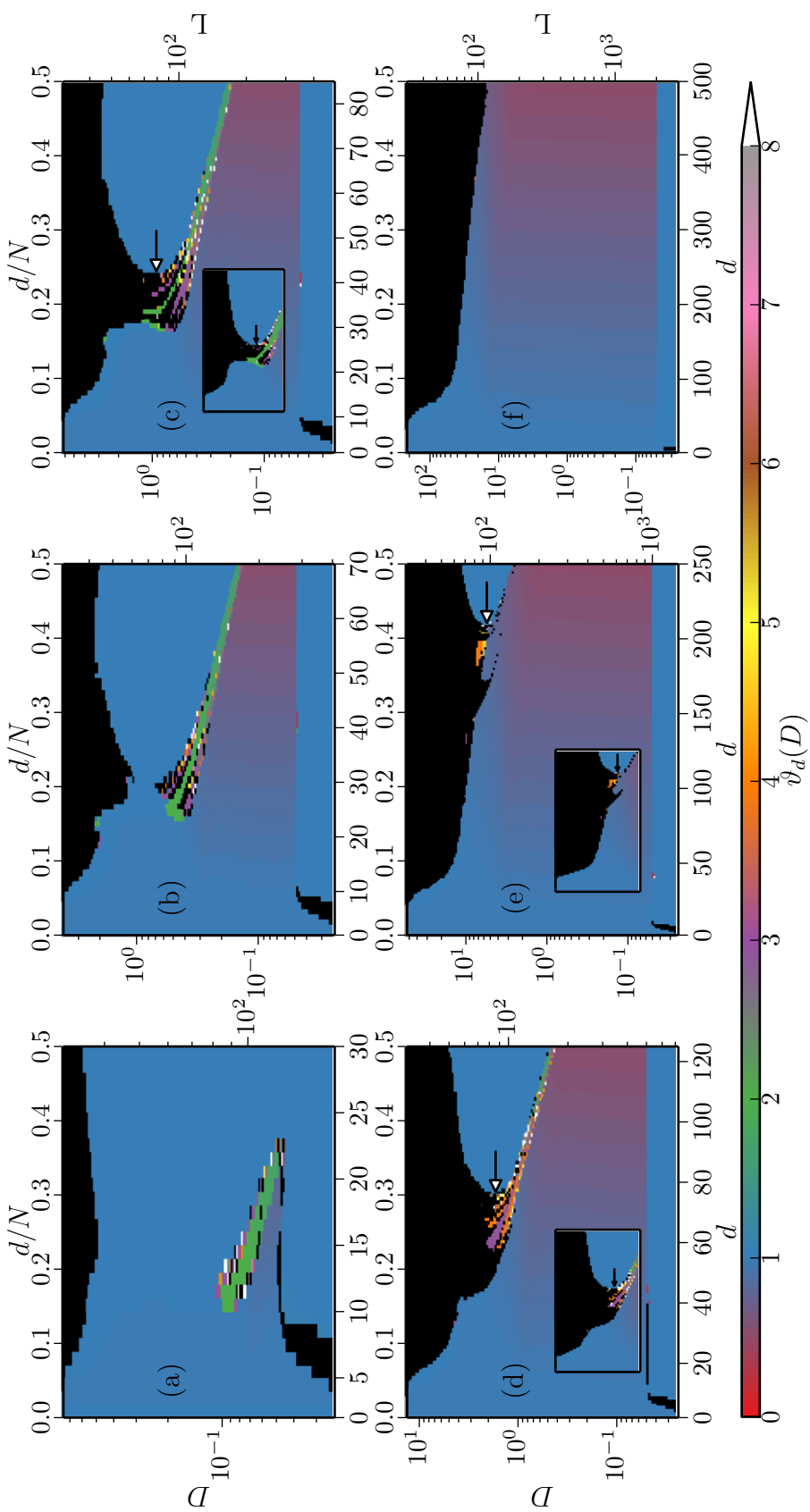

Figure 6.10: Typical evolution of phase diagrams with increasing N. Color-coded $\vartheta_d(D)$ in the (d, D) plane. (a) $N = 60$, $R = 2$, (b) $N = 140$, $R = 2$, (c) $N = 170$, $R = 2$ (inset $N = 510$, $R = 3$), (d) $N = 250$, $R = 2$ (inset $N = 700$, $R = 3$), (e) $N = 500$, $R = 2$ (inset $N = 1400$, $R = 3$), (f) $N = 1000$, $R = 2$. Right and upper axes show L and d/N as units of measurement. Black regions indicate propagation failure. Other Parameters: $\beta = -1.1$, $\varepsilon = 0.04$.

region also stay (approximately) constant as well as the maximum value of L that is attained at all. This is consistent with the expected scaling behavior at high D.

6.3.3 Intermediate coupling strength

In the region between the two limiting regimes just discussed, the appearance of the phase diagrams changes drastically when N (or R) is changed. Most of the complex behavior explained in Sec. 6.2, like e.g. period multiplying takes place in this intermediate region of the coupling strength.

The mechanisms behind these phenomena can be regarded as a well balanced interplay between (i) the discrete network nature of the system, (ii) the transition to the continuous regime and (iii) beginning dispersion effects. The discrete network nature of the system allows triggering of secondary wave pairs through the additional long-range link. Due to the transition to the continuous regime, where many nodes are excited at the same time, (a) the node at one end of the additional link is perturbed longer and thus more strongly when excitation passes the other end and (b) excitation is not lost easily when one single node is perturbed through the additional link. Beginning dispersion effects cause the inhibitor level to still be elevated at the other end of the shortcut from the previous wave passage.

The network size N has an impact on two out of this list of three and thus must clearly influence the appearance of the phase diagram. This is demonstrated in Fig. 6.10. In Fig. 6.10(f), $N = 1000$ and period multiplying is not observed anymore. For even larger N the appeareance of the phase diagram does not change significantly any more. Thus, for fixed nearest neighbor number R we have a family of phase diagrams parameterized by the size of the network N.

The nearest neighbor number R changes the balance between the influence of the local links (those that are present in the regular ring) and the additional link of the minimal small-world model. Increasing R effectively lowers the weight of the additional link, by attaching more local links to every node. Also, by the definition of L, Eq. (4.10c), increasing R has the same effect as increasing D. Thus it influences all three items (i)-(iii) of above list and this way has an impact on the phase diagrams as well as N.

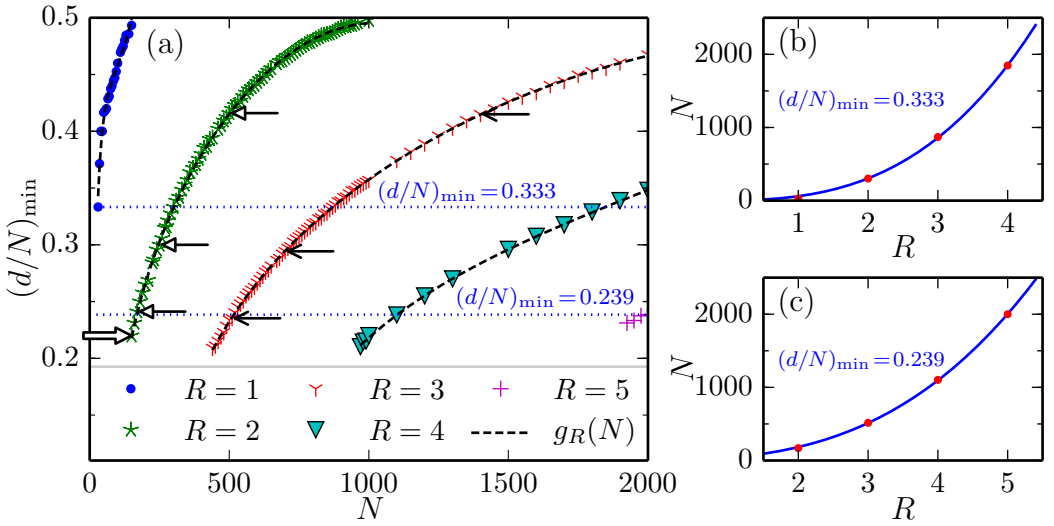

Figure 6.11: Scaling behavior of intermediate region of phase-diagrams. (a) Value $(d/N)_{\min}$ at characteristic point introduced in Sec. 6.3.3 and marked in Fig. 6.10(c-e) vs. N for $R = 1, 2, 3, 4, 5$. Dashed line for fitted curves. (b) N values for $(d/N)_{\min} = 0.333$ vs. R, measured data points (red dots) and fit to const$\cdot q(R)$ (blue line). (c) Same as (b) for $(d/N)_{\min} = 0.239$. Arrows in (a) mark data points for Fig. 6.10(c)-(e) (white tip), insets of Fig. 6.10(c)-(e) (black tip) and Fig. 6.9 (white tip and stem).

Next, we discuss how the influence of R and N on the phase diagrams relate to each other. Given a phase diagram for (N, R), it is possible to find higher values $(\tilde{N}, \tilde{R})$ at which the phase diagram looks very similar. In order to quantify this, we choose a characteristic point which is present in the 'middle phase' of the evolution of phase diagrams. We consider the border between propagation failure to lower values of d and sustained wave propagation without influence of the additional link to higher values of d at intermediate to high coupling strengths. At some value of D, this border attains a minimum value of $d_{\min}$ or $(d/N)_{\min}$, respectively. This point is marked by an arrow in Figs. 6.10(c)-(e).

Choosing a fixed $R = 1, 2, 3, 4, 5$, we confirm the existence and (numerically) determine the position $(d/N)_{\min}$ of this point with increasing N. The obtained values are shown in Fig. 6.11. The measured data $(d/N)_{\min}$ in dependence on N can be fit to a function $g_R(N) = a_R N^2 + b_R N + c_R + d_R N^{-1}$ to very good approximation. So far we do not have a good explanation or motivation for

this particular form of the fitting function.

In a second step, we choose a fixed value for $(d/N)_{\min}$ and use the inverse of the fitting functions $g_R(N)$ to obtain the value of N at which this desired value of $(d/N)_{\min}$ is attained for a certain R. This leaves us with (N, R) tuples $(N_1, 1), ..., (N_5, 5)$ for which the phase diagrams show the same value of $(d/N)_{\min}$. Moreover, these phase diagrams with the same value of $(d/N)_{\min}$ also show other similar features at similar locations (measured in L and d/N), though the diagrams are not completely identical. The insets in Figs. 6.10(c)-(e) show the phase diagrams for networks with the same $(d/N)_{\min}$ but different N and $R = 3$ for illustration. The corresponding data points in Fig. 6.11 are marked by an arrow, as is the data point for Fig. 6.9.

At the values $(d/N)_{\min}$ we examined, we find that the points $(N_1, 1), ..., (N_5, 5)$ lie on a curve described by $N/q(R) = \text{const}$. This is shown exemplarily for $(d/N)_{\min} = 0.333$ and $(d/N)_{\min} = 0.239$ in Figs. 6.11(b),(c).

This behavior is interesting because in the limit $N \to \infty$, $D \to \infty$ with L from Eq. (4.10c), the domain length L of the limiting continuous system $\dot{u} = u - \frac{u^3}{3} - v + u''$, $\dot{v} = \varepsilon(u - \beta), (u, v)(t, 0) = (u, v)(t, L)$ and with it all other length scales depends on $N/\sqrt{q(R)}$ instead of $N/q(R)$. As explained above, the behavior in the intermediate region can be viewed as an interplay between discrete and continuous effects, thus it is surprising that in the complicated intermediate region, such a simple scaling law can be found at all.

6.4 Analytic approximations

To round off this chapter, we present two analytical calculations for the regime of low coupling strenghts. With the first we approximate the critical distance for shortcut blocking in dependence of D. In the second, we estimate the threshold value D_2 above which the generation of secondary wave pairs via the additional link takes place. Both calculations use the active point approximation that has also been used in Sec. 5.3.2.

6.4.1 Critical distance for shortcut blocking

The triggering of a secondary wave pair through the additional link can be prevented by the inhibitor level at this node being too high from the last

passage of the wave. We do an approximation of the critical distance d_{crit} up to which triggering of a secondary wave pair is prevented.

We consider Eqs. (6.2) at the node at which the secondary wave pair would be triggered through the additional link. In the limit of $\varepsilon \to 0$, the transition to the excited state of this node is described by the fast subsystem of Eqs. (6.2). This is just Eq. (6.2b) with v acting as a parameter. This node receives input from its $2R$ neighbors on the regular ring and from the excited node at the other end of the additional link. The neighboring nodes of this node as well as the neighboring nodes of the node at the other end of the additional link are approximately in the same state respectively so that the coupling term in their equation vanishes and their u-values can be described by the (stable) fixed points of $\dot{u} = u - u^3/3 - v$. We term those fixed points $z_1(v) < z_2(v) < z_3(v)$, where z_1 and z_3 are stable. Thus the approximating bistable system for the node under consideration is

$$\dot{u} = u - \frac{u^3}{3} - v + D\left(z_3(v_0) + 2Rz_1(v) - (2R+1)u\right), \tag{6.4}$$

with $v_0 = \beta - \beta^3/3$ being the inhibitor (homogeneous) steady state value of Eq. (6.2).

For $v_0 \leq v < v_{\text{crit}}$, Eq. (6.4) possesses only one stable fixed point which is the excited value. Another stable and one unstable fixed point appear in a saddle-node bifurcation at $v = v_{\text{crit}}$ so that for $v > v_{\text{crit}}$, the node can remain at rest. The location of the saddle-node bifurcation is determined by the solution (u^*, v_{crit}) of

$$0 = u - \frac{u^3}{3} - v + D\left(z_3(v_0) + 2Rz_1(v) - (2R+1)u\right) \tag{6.5a}$$

$$0 = 1 - D(2R+1) - u^2. \tag{6.5b}$$

From the second equation we infer that this approximation can only be used up to $D = 1/(2R+1)$. The reason why this approximation breaks down for larger D is that the coupling term in the unexcited neighboring nodes becomes stronger with increasing D and thus their state cannot be approximated by $z_1(v)$ any more.

In a second step, we approximate the time t_{crit} it takes until a node reaches this critical inhibitor level after becoming excited. In this approximation, we neglect the time that the transitions to and from the excited state take, only

taking into account the time it spends on the slow manifold (u-nullcline) of Eqs. 6.2. While on the slow mainfold, a node has approximately the same u value as its neighbors and we can again neglect the coupling term. Doing the transformation $t \to \tilde{t} = t/\varepsilon$, taking the limit $\varepsilon \to 0$, from Eqs. (6.2) we get

$$\begin{aligned} \dot{u} &= 0 = u - \frac{u^3}{3} - v \\ \dot{v} &= u - \beta, \end{aligned}$$

plugging the algebraic constraint of the first equation into the second gives

$$\dot{u} = \frac{u - \beta}{1 - u^2}, \tag{6.6}$$

where all derivatives are with respect to $\tilde{t}$. From this equation we can get t_{crit} by integrating

$$t_{\text{crit}} = \varepsilon^{-1} \left(\int_{z_3(v_0)}^{1} + \int_{-2}^{z_1(v_{\text{crit}})} \right) \frac{1 - u^2}{u - \beta} \mathrm{d}u, \tag{6.7}$$

where the boundaries of the integral are the u-values on the u-nullcline that the system jumps to and from in the limit $\varepsilon \to 0$.

With that, $d_{\text{crit}}/N = t_{\text{crit}}/T_0$, where we get T_0 from the simulations for $d = 0$. The calculated value for $1 - d_{\text{crit}}/N$ is shown as a yellow dashed line in Fig. 6.9.

The main reason for the deviation is that close to the saddle-node bifurcation of Eq. (6.4), it takes a finite time until u has reached full excitation. The node that triggers the excitation through the additional link however is only excited for a finite time which need not be sufficient to lead to a full excitation of u.

We take this into account by calculating the saddle-node normal form $\dot{x} = a(v - v_{\text{crit}}) + bx^2$, with $x \equiv u - u^*$ for Eq. (6.4) with

$$a = 1 + \frac{2kD}{1 - z_1(v_{\text{crit}})^2}\,, \qquad\qquad b = -u^*$$

Close to the bifurcation point, the time t_{exc} until excitation can be estimated by the time x needs to go from $-\infty$ to $+\infty$.

$$t_{\text{exc}} = \frac{\pi}{\sqrt{ab(v - v_{\text{crit}})}}\,.$$

Setting this equal to the time the excitation lasts that is, first integral in Eq. (6.7), we obtain

$$v = v_{\text{crit}} + \frac{1}{ab}\left(\frac{\varepsilon\pi}{\int_{z_3(v_0)}^{1}\frac{1-u^2}{u-\beta}\mathrm{d}u}\right)^2 .$$

In Fig. 6.9, $1 - d_{\text{crit}}/N$ for the solution of this equation is plotted as a red solid line.

As in Sec. 5.3.2, the resulting equation itself for the critical inhibitor level contains several roots of third order polynomials and thus cannot be treated analytically. The obtained curves in Fig. 6.9 have been calculated numerically.

6.4.2 Critical coupling strength for secondary wave pair generation

We can use a very similar technique to estimate D_2. This coupling strength marks the value, below which no secondary wave pairs can be triggered through the additional link. Instead of treating v as the bifurcation parameter in Eq. (6.4), we use D, fixing $v = v_0$. However the value D^* for the saddle-node bifurcation, attained by this calculation is much too small. As before, the main reason is the finite time, the excited node can exert its influence through the additional link. Following the steps of Sec. 6.4.1, we obtain the estimation

$$D_2^{\text{est}} = D^* + \frac{1}{ab}\left(\frac{\varepsilon\pi}{\int_{z_3(v_0)}^{1}\frac{1-u^2}{u-\beta}\mathrm{d}u}\right)^2 ,$$

where now

$$a = 2R\beta + z_3(v_0) - (2R+1)u^* , \qquad b = -u^* .$$

For $R = 2$, $D_2^{\text{est}} \approx 0.031$, which is still too small (cf. Table 6.1). This value is marked by a dotted white line in Fig. 6.9.

The deviation of the approximated values for D_2 and d_{crit} are in the same direction. Possible reasons include the following: (i) ε is not exactly zero and thus, the excitation does not happen instantaneously. Thus, the inhibitor level at the node that is about to become excited will rise to some extent An only partially excited node at the other end of the additional link leads to a sub-threshold excitation. This in turn makes a larger global coupling

strength necessary to trigger a full excitation. (ii) The backcoupling through the additional link makes the excitation of the node that triggers the secondary wave pair smaller.

Chapter 7

Effects of small-world topologies on wave propagation

In this chapter we present the last variation of the basic theme presented in Chapter 4. We will investigate the effect that small-world modifications of the topology of a ring network have on excitation wave propagation. Instead of adding one link and varying the distance of this link as in Chapter 6, we will investigate the collective effects that many added links have on wave propagation.

Already a small number of additional links offer an overwhelming number of possibilities to be placed on the ring. Thus, we will only treat the number of additional links as the parameter we will focus on and formulate our results as an average over many realizations with the same number of additional links.

Similar to Chapters 4, 5, and 6, the system behaves differently for small and for large coupling strengths. In general, we find that increasing the number of additional small-world links impedes the propagation of excitation waves in the network.

The chapter is structured as follows: In Sec. 7.1, we shortly introduce the model used in this Chapter as well as the numerical procedure employed. Moreover we share some general observations from the numerical simulations. In Sec. 7.1.1, we investigate in more detail the transition to propagation failure in the regime of low coupling strengths. We are able to apply some of the results of Chapter 6 for the low D regime here. In Sec. 7.1.2 we focus on the transition to propagation failure in the regime of high coupling strength.

Our special attention in that section lies on the scaling behavior of the transition to propagation failure with respect to system size and coupling range. In Sec. 7.1.3 we briefly report on the observed values for an optimal coupling strength that allows propagation of excitation waves at the highest possible number of additional links. In Sec. 7.2, we construct a continuum approximation for excitation wave propagation on Newman-Watts small-world network models. Using this approximation, we predict the critical number of additional links for high coupling strengths. The results of this chapter are contained in [101].

7.1 Model and observations

The networks investigated in this chapter are the Newman-Watts small-world networks of Sec. 2.3.4. As the local dynamics on the nodes of these networks we use again the FitzHugh-Nagumo dynamics, with diffusive coupling in the activator variable. Thus, the dynamical system reads

$$\dot{u}_i = u_i - \frac{u_i^3}{3} - v_i + D\sum_{j=1}^{N} \mathcal{A}_{ij}\,(u_j - u_i) \tag{7.1a}$$

$$\dot{v}_i = \varepsilon(u_i - \beta) \qquad i \in \{1, ..., N\}\,, \tag{7.1b}$$

with fixed parameters $\varepsilon = 0.04$ and $\beta = -1.1$ such that the local dynamics are in the excitable regime. $\mathcal{A}_{ij}$ is the adjacency matrix of the Newman-Watts small-world network model.

For investigating the collective effects of many added long-range links, we proceed similar to Chapter 6. We start with a ring with N nodes and a coupling range R, and choose initial conditions such that a singular traveling wave is generated on the ring without any additional links. We take a snapshot of this traveling wave as initial conditions for the system on a small-world network generated from this ring network with the number of additional links being n. We then further integrate the system on the small-world network numerically, using a Runge-Kutta Fehlberg4(5) scheme with adaptive stepsize. As in Chapters 5 and 6, the homogenous steady state is stable and thus, the system can either display continuing activity or it can decay back to the stable homogeneous state. Differently from Chapter 6, we monitor only whether the solution

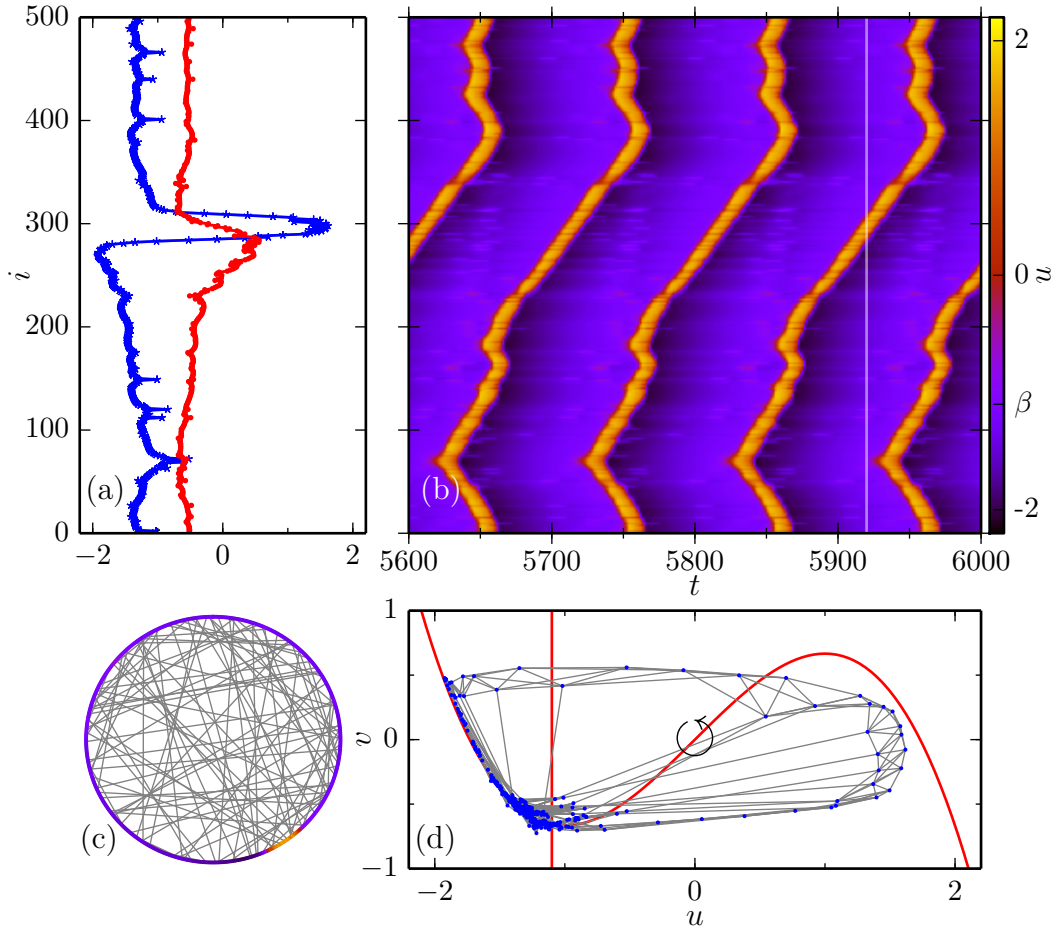

Figure 7.1: Traveling wave solution on a Newman-Watts small-world network with $N = 500$, $R = 3$, $n = 102$. The coupling strength $D = 0.4$. (a) Snapshot of the solution, u_i (blue asterisks), v_i (red dots) vs. node index i. (b) Color-coded activator level $u_i(t)$ as space-time plot with time of snapshot marked by vertical line. (c) Image of the network realization. Nodes are color coded according to their activator level at snapshot time. Indices ascending counter-clockwise with $i = 1$ at the top. (d) Snapshot of the solution as phase portrait. State of each node in the (u, v) plane (blue dots), including all links of the network (gray lines) and nullclines (red). Other parameters: $\varepsilon = 0.04$, $\beta = -1.1$.

for a certain small-world network shows sustained activity or propagation fails.

We want to stress that the number of additional links alone does not determine, whether a Newman-Watts small-world network supports sustained wave

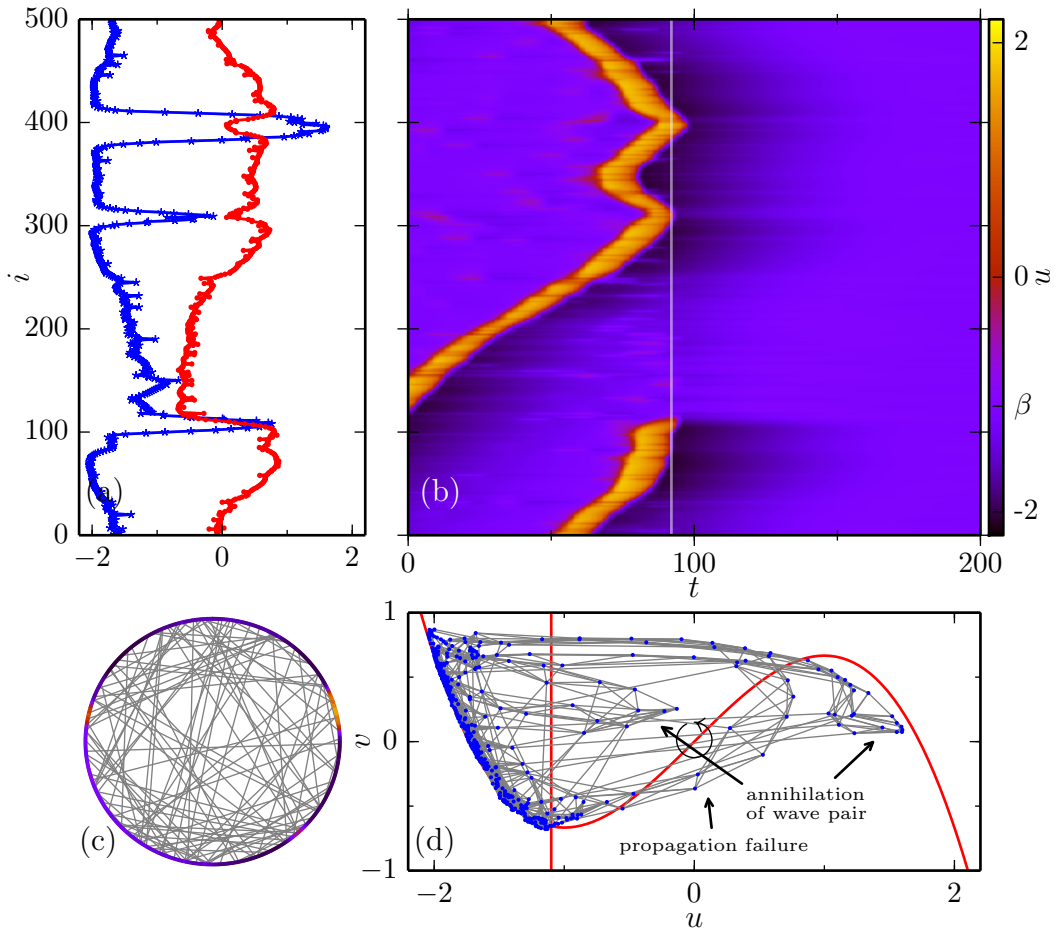

Figure 7.2: Same as Fig. 7.1 with a different realization of the network.

activity or not. Examples are shown in Figs. 7.1, and 7.2 for $N = 500$, $R = 3$. In both cases, all parameters including the number of additional links $n = 102$ and the coupling strength $D = 0.4$ are identical. The difference is the particular realization that has been used. The realization used in Fig. 7.1 permits sustained wave activity, the one in Fig. 7.2 does not. Note that this pattern is similar to the multiple-pulse generation pattern found in spatially continuous FitzHugh-Nagumo systems with nonlocal long-range couplings [11].

It is not only the particular realization of a Newman-Watts small-world network that determines whether we find sustained wave activity or not. The same realization can also lead to different outcomes, when the coupling strength D differs. This is demonstrated in Figs. 7.3 and 7.4, where $n = 11$. The coupling strength in Fig. 7.3 is set to $D = 1.1$, whereas in Fig. 7.4 it is $D = 1.2$, lead-

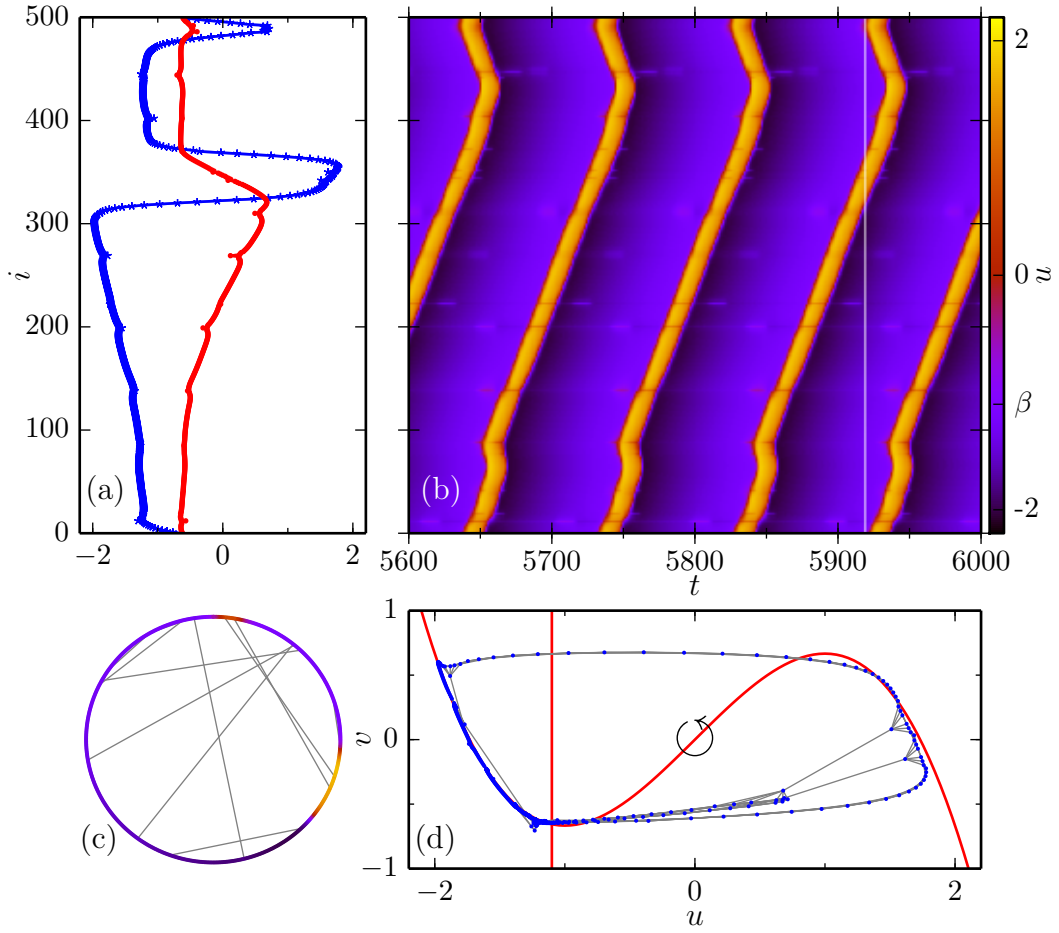

Figure 7.3: Same as Fig. 7.1 with $N = 500$, $R = 3$, $n = 11$ and $D = 1.1$

ing to sustained wave activity in the former and to propagation failure in the latter.

In Figs. 7.2 and 7.4 it can also be seen, that propagation failure is never caused by collision with another counterpropagating wave. We have only observed pairwise generation of secondary waves, see e.g. (white) vertical line in Fig. 7.1(b). As the mutual annihiliation of counterpropagating waves also takes place only pairwise (see vertical line in Fig. 7.2(b)), this mechanism cannot change the number of simultaneously occuring waves from even to odd or vice versa and therefore cannot cause propagation failure. The example in Fig. 7.2 is selected such that at the time of the snapshot, mutual annihilation of wave pairs and propagation failure occur simultaneously. In Fig. 7.2(c), the nodes' states at the time of the snapshot are displayed and those group of

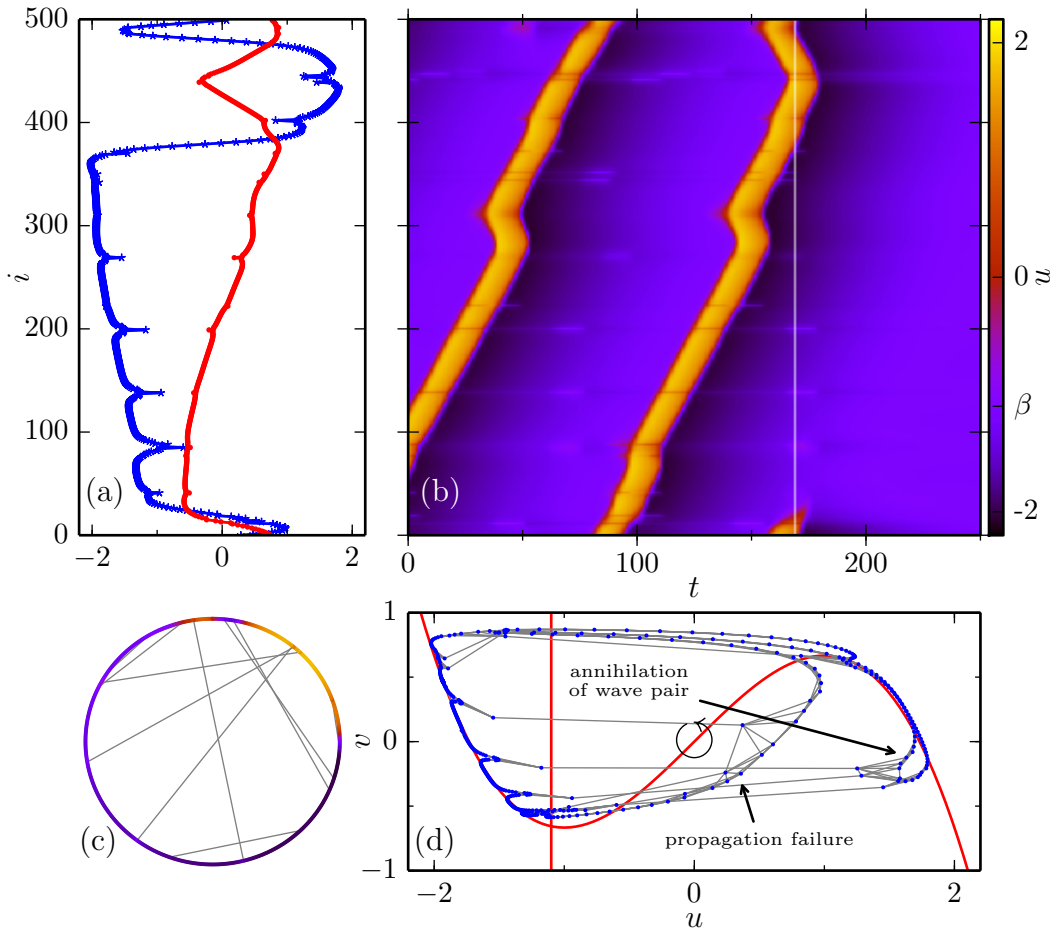

Figure 7.4: Same as Fig. 7.3, same network realization but $D = 1.2$.

nodes which undergo propagation failure or annihiliation of a wave pair are marked with arrows in Fig. 7.2(d) and 7.4(d). It can be seen in that plot as well as in Fig. 7.4(c) that in decaying to the left branch of the u-nullcline, the group of nodes undergoing propagation failure sweeps over a large section of the middle part of the u-nullcline. The group of nodes that experience the mutual annihilation of a wave pair in contrast cross the middle part of the u-nullcline at a small corridor.

In general it is not possible to pinpoint the exact mechanism that causes propagation failure when multiple additional links are present. When many additional links have one end connected within a small region, the backcoupling effect of these can be so strong that this leads to propagation failure. This behavior is shown in Fig. 7.7 (which will be explained in detail in Sec. 7.1.1). Also,

several additional links ending in a region can lead to a higher inhibitor level, which prevents further propagation. This behavior can be seen in Fig. 7.4(c), where the group of nodes that undergo propagation failure ends on the left part of the u-nullcline with a significantly raised inhibitor level. Those nodes that show elevated inhibitor level are connected to that group of nodes where two counterpropagating waves collide. Thus in this case, a counterpropagating wave pair triggers subthreshold excitations at some part of the ring which leave the inhibitor level raised so much that propagation failure occurs. In that example things are even more complex because the secondary wave pair involved in this case of propagation failure is only generated at the second passage of the wave.

In order to describe the collective effect in dependence on the number of additional links n, we consider the ensemble of all Newman-Watts small-world networks parametrized by network size N, coupling range R, and number of additional links n. We define $f_{\text{sust}}(n, D; N, R)$ as the fraction of realizations of a Newman-Watts small-world network that support sustained wave activity of Eqs. (7.1) with coupling strength D. From now on f_{sust} is the quantity we will be concerned with for the remainder of this chapter.

We determine f_{sust} numerically by considering an ensemble of 200 Newman-Watts small-world networks for every combination (N, R, n). For each examined value of the coupling strength D, we integrate the dynamics with initial conditions as explained above for every element of this ensemble. The fraction of realizations in this ensemble that support sustained wave activity gives our estimate of $f_{\text{sust}}(n, D; N, R)$. The number of additional links is varied from $n = 1$ to $n = NR$. When $n = NR$ there are as many additional links as links on the original ring and we have not observed a single case in which there was sustained wave activity for such a high number of additional links. Thus there is no need to raise n any further. Also, in order to keep the computational effort feasible, we did not use every number n between 1 and NR. Instead we used about 50 values of n, distributed logarithmically between 1 and NR. This is also justified by the fact that for large n, the outcome for different but close n hardly differs. In the following, we omit N and R from the argument of f_{sust}, writing just $f_{\text{sust}}(n, D)$, as N and R will be clear from the context and fixed when varying n and D.

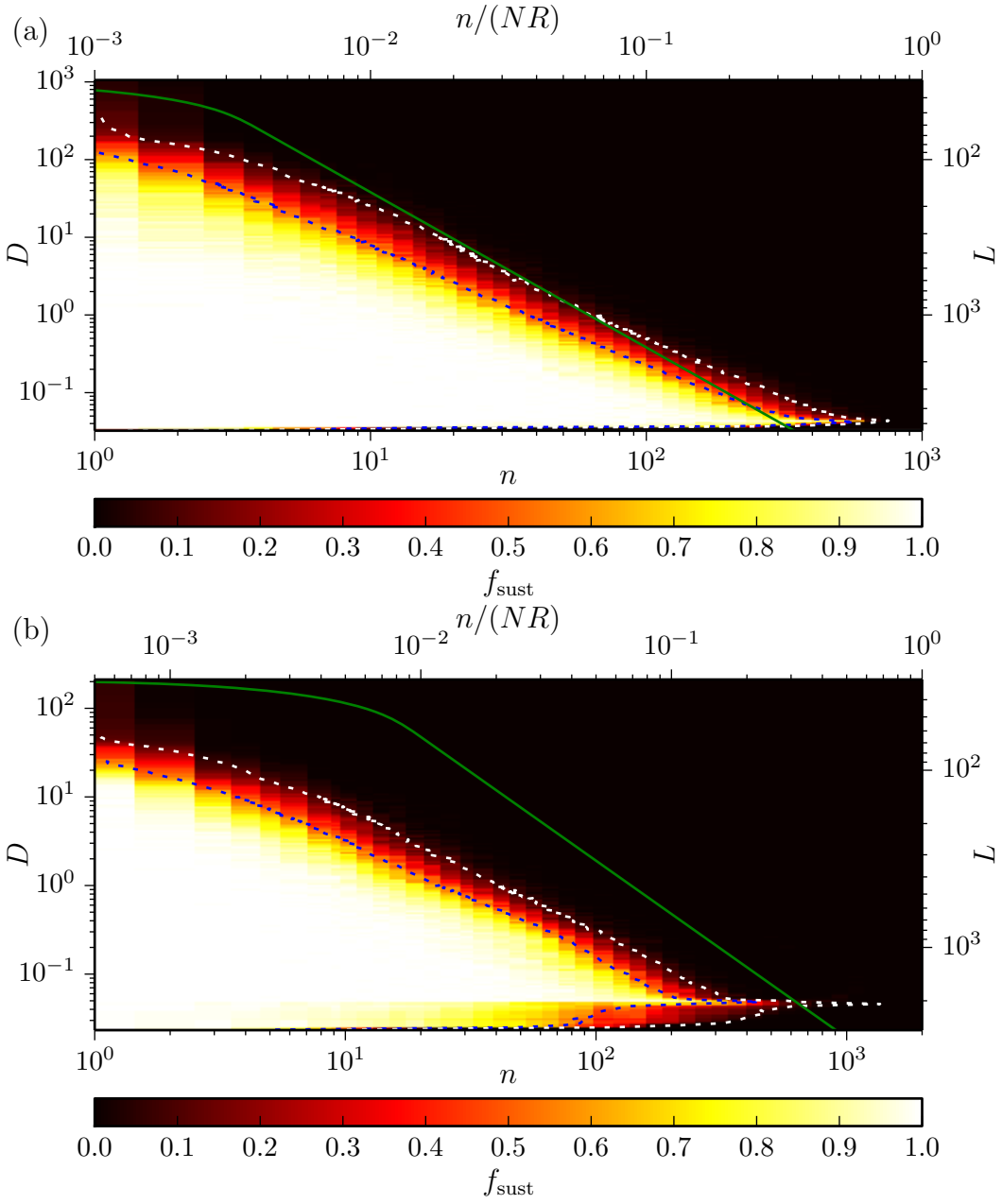

Figure 7.5: Heatmap of the fraction $f_{\mathrm{sust}}(n, D)$ of realizations of Newman-Watts small-world networks that support sustained wave activity. Bottom axis gives number of additional links n. Left axis gives coupling strength D. Right axis gives 'virtual' length L (see Sec. 7.1.2). Top axis gives fraction of additional links $n/(NR)$. White dotted line gives level curve $f_{\mathrm{sust}}(n, D) = 0.1$. Blue dotted line gives level curve $f_{\mathrm{sust}}(n, D) = 0.5$. Green line gives analytical approximation of Eq.7.4 (a) $N = 1000$, $R = 1$. (b) $N = 1000$, $R = 2$. Other parameters: $\varepsilon = 0.04$, $\beta = -1.1$.

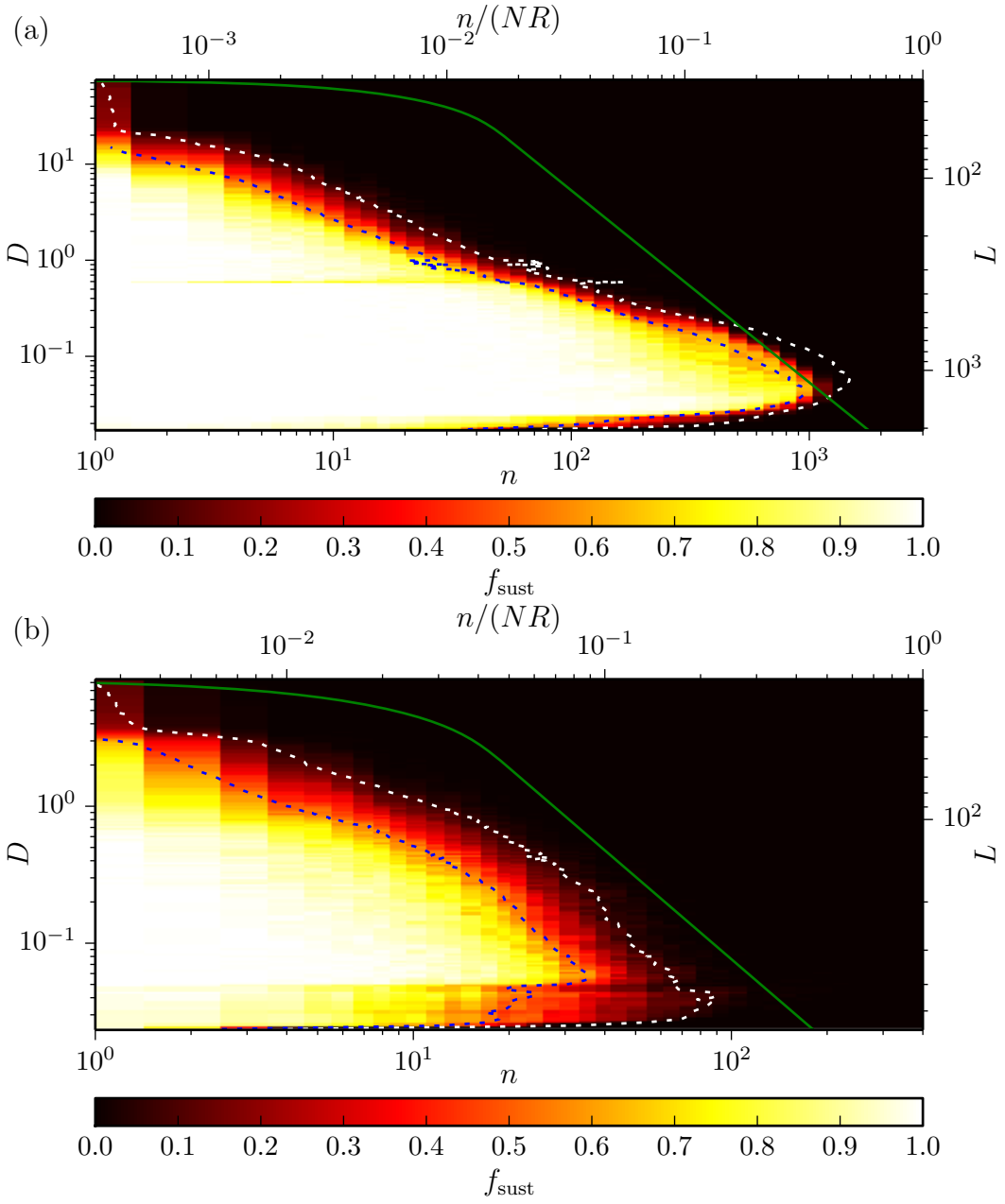

Figure 7.6: Same as Fig. 7.5. (a) $N = 1000$, $R = 3$. (b) $N = 200$, $R = 2$.

In general, we observe that for a given D, increasing the number n of additional links always leads to the decrease of f_{sust}. The transition from $f_{\mathrm{sust}} \approx 1$ to $f_{\mathrm{sust}} \approx 0$ usually happens in a small region of $\log(n)$. The point of transition, however, varies considerably on the coupling strength D. The findings will be discussed in greater detail in the following sections.

In Figs. 7.5 and 7.6, heatmaps of $f_{\mathrm{sust}}(n, D)$ are shown for different N and

R. To compare the behavior of $f_{\text{sust}}(n, D)$ for different N and R, we calculate level curves (n_α, D_α) for which $f_{\text{sust}}(n_\alpha, D_\alpha) = \alpha$. We do this for $\alpha = 0.5$ and $\alpha = 0.1$, network sizes 150 to 1000 and $R = 1, 2, 3$. To calculate these curves, we use the fact that for each D, there is just one transition from $f_{\text{sust}} \approx 1$ to $f_{\text{sust}} \approx 0$ in n and thus exactly one n_α. Therefore, the curve (n_α, D_α) can be viewed as a function $n_\alpha(D)$. So in order to calculate the points n_α for a fixed N, R, we fit a sigmoidal function to the numerical data for each fixed D. Then, $n_\alpha(D)$ is found by evaluating the inverse of the fitted sigmoidal function at the desired level α for each value of D. The reason for adopting this procedure is the noisyness of our data. The level curves are shown in Figs. 7.5 and 7.6 as white dotted ($\alpha = 0.1$) and blue dotted ($\alpha = 0.5$) lines. The $\alpha = 0.5$ level curves for all investigated combinations of N and R in one plot are shown in Fig. 7.13(a) on page 125. The rest of this plot will be explained later on.

In Chapters 4 and 6 we observed two limiting regimes, namely that of very low coupling strength D and that of high coupling strength D. To some extent, the results obtained for these limiting regions can be transferred to the system of this chapter.

7.1.1 Low coupling strength – discrete limit

In Chapter 4.2.2, we showed that there is a minimum value D_{min} of the coupling strength, below which no propagation is possible on a ring network. In Chapter 6, we found transition values D_1, D_2, and D_{2-} at which the effect that one additional link exerts on traveling wave solutions changes. Between D_{min} and D_1 we observed direct failure of the traveling wave, where the backcoupling of one additional link suffices to lead to propagation failure regardless of the distance it spans. Between D_1 and D_{2-} lies the region of inhibitor-mediated failure in which a sub-threshold excitation triggered through the additional link can leave the inhibitor sufficiently raised to stop the wave. Above a coupling strength of D_2, the generation of secondary wave pairs is possible. For $R = 1$ and $R = 2$, we found $D_{2-} = D_2$. Only for coupling ranges above 2, there is a region between D_{2-} and D_2 in which the subthreshold excitations triggered through the additional link are too weak to leave the inhibitor elevated enough for propagation failure.

All values D_{min}, D_1, D_2, and D_{2-} depend on the coupling range R but not

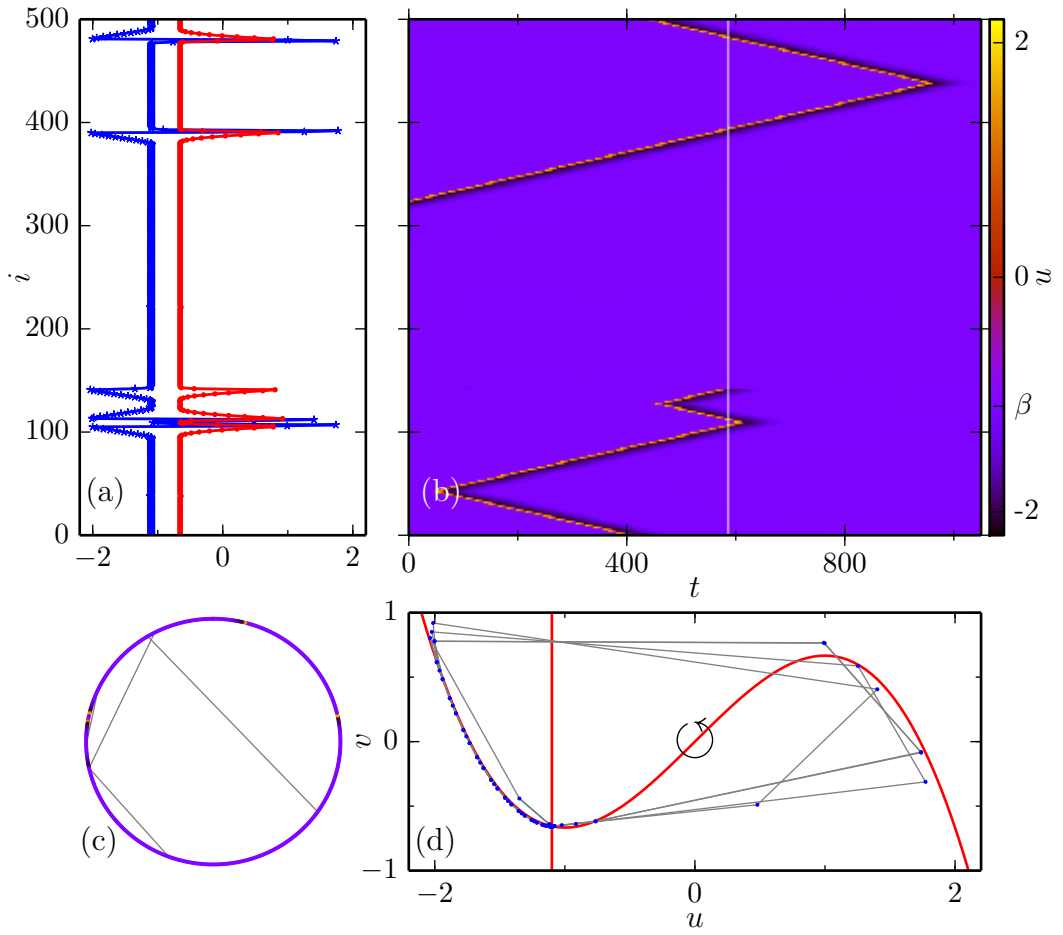

Figure 7.7: Same as Fig. 7.1 with $N = 500$, $R = 1$, $n = 4$ and $D = 0.0373$.

on the number of nodes N. They are found in Table 6.1 on page 81.

Now we describe the effects that n added links have on traveling waves in these regions of the coupling strength by investigating the fraction of realizations f_{sust} that allow sustained wave propagation. As explained in Sec. 6.2.2, in the region of direct failure, one link, regardless of the distance it spans, is enough to lead to propagation failure. Thus, in this region we expect f_{sust} to be constantly zero independently of the number n of additional links. In Figs. 7.8(a), 7.9(a), and 7.10(a), f_{sust} is displayed vs. D for different numbers n of additional links. In the region of direct failure (marked by red diagonal square hatching) the measured f_{sust} is constantly zero as expected.

Above a coupling strength D_1, a single additional link spanning a certain distance leads to inhibitor-mediated failure (cf. Sec. 6.2.3). Here we observe

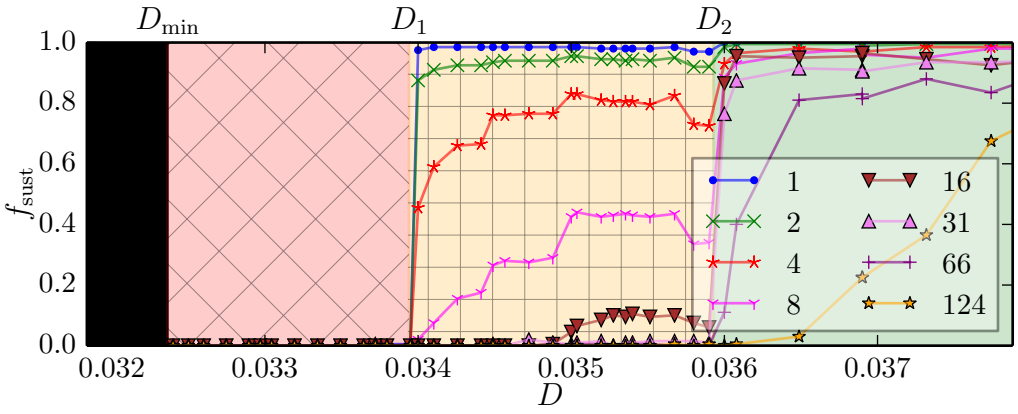

Figure 7.8: Fraction of network realizations which support sustained wave activity f_{sust} vs. D. Regime of very low coupling strengths. $N = 500$, $R = 1$. Legend gives number of additional links n. Background color and hatching indicate region of direct failure (red diagonal squares) inhibitor mediated failure (yellow squares) and possible generation of secondary wave pairs (green). Other parameters: $\varepsilon = 0.04$, $\beta = -1.1$.

f_{sust} not being constantly zero regardless of the number of additional links n. Above D_1, f_{sust} decreases with an increasing number of additional links n. In a realization of a Newman-Watts small-world network model, the additional links are distributed randomly across the ring. Thus, also the distances are distributed randomly with every distance having the same probability of occurring. Therefore, increasing the number of additional links makes it more likely that a value of the critical distance occurs in the network. Also, when crossing D_1 from below, f_{sust} will make a jump to a value close to one when n is small, because suddenly only certain distances of an additional link will lead to propagation failure. For small n only few realizations feature a link with such a critical distance.

We also note that for a fixed n, f_{sust} increases with increasing D. This is understandable by taking a look at the low D region of Fig. 6.9 (page 97). The values of the distance of one additional link that will lead to (inhibitor-mediated) failure are the horn-like black structure at the lower left in this Figure. This structure becomes narrower when D is increasing, meaning that fewer distances of one additional link will lead to inhibitor-mediated failure. Thus, with growing D, fewer realizations posses an additional link spanning a

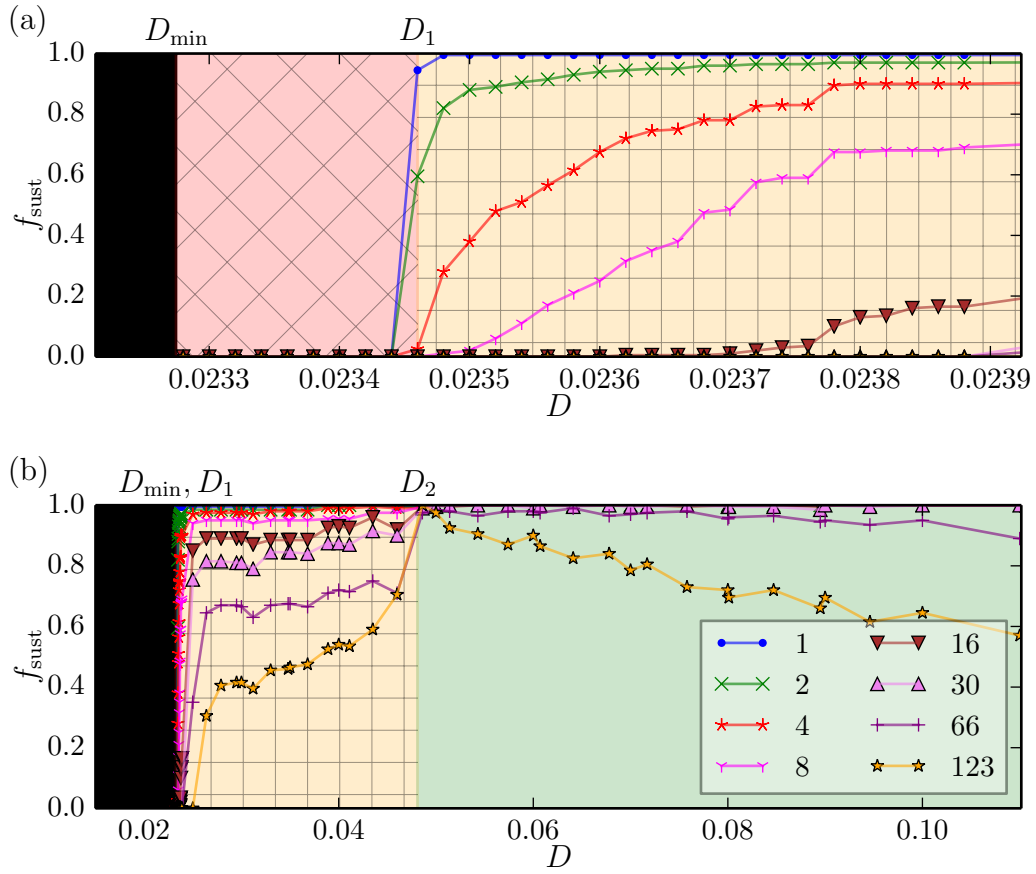

Figure 7.9: Same as Fig. 7.8 for $N = 1000$, $R = 2$. (a) and (b) show different intervals of D, so that each region of the coupling strength is visible well. Background color and hatching indicate region of direct failure (red diagonal squares) inhibitor mediated failure (yellow squares) and possible generation of secondary wave pairs (green).

critical distance. This behavior is independent of N as are the actual values of critical distances.

In Figs. 7.8, 7.9 and 7.10, the region of inhibitor-mediated failure is marked by yellow square hatching. The behavior in these regions is what is expected from above reasonings. Note that for $R = 3$, the region of inhibitor-mediated failure ends at a value $D_{2-} \neq D_2$. The region of possible secondary wave pair generation for $R = 3$ starts at $D_2 \approx 0.589$ which is not shown in Fig. 7.10(b).

To quantitatively describe the dependence of f_{sust} on n in the regime of inhibitor-mediated failure, we note the following: For a Newman-Watts small-world network with number of nodes N, coupling range R and n additional

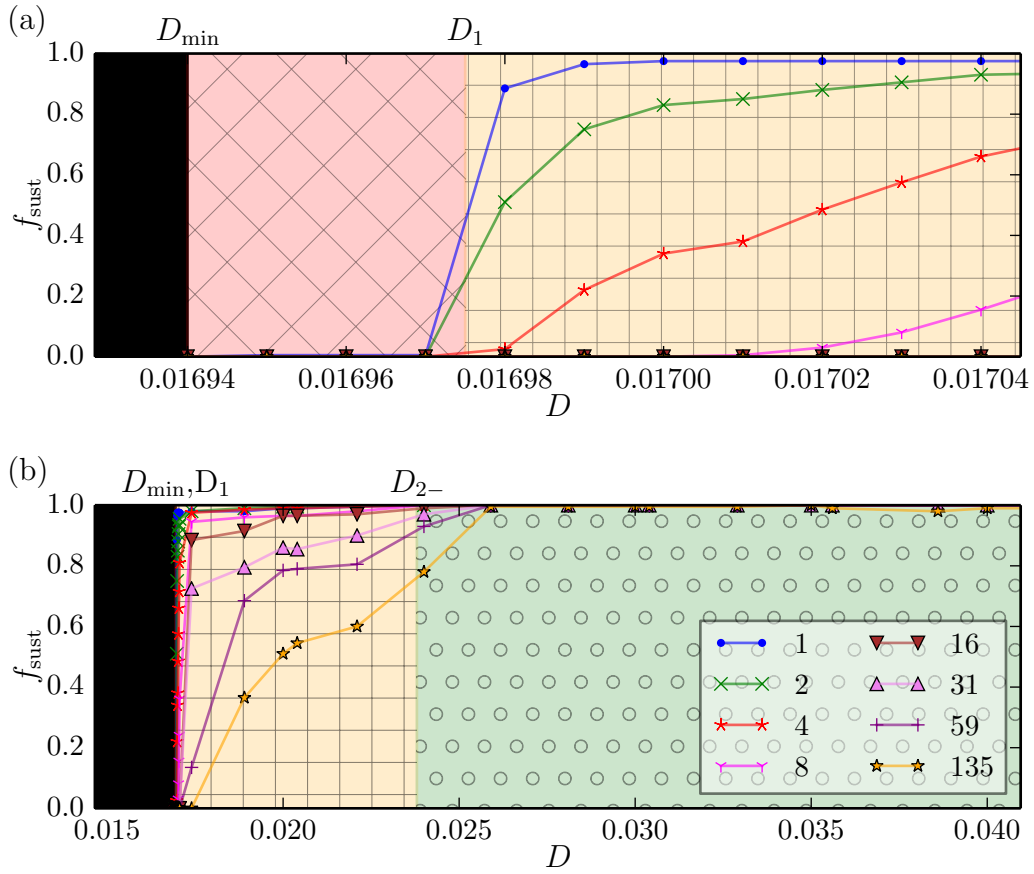

Figure 7.10: Same as Fig. 7.8 for $N = 1000$, $R = 3$. (a) and (b) show different intervals of D so that each region of the coupling strength is visible well. Background color and hatching indicate region of direct failure (red diagonal squares) inhibitor mediated failure (yellow squares) and region of neither inhibitor mediated failure nor generation of secondary wavepairs (green circles).

links, we denote the number of critical distances at a fixed coupling strength D by $\bar{d}$. The probability p that a randomly added link spans such a critical distance is given by

$$p = \frac{\bar{d}}{N - 2R - 1}\,.$$

The reason for the term in the denominator is that multiple links between a pair of nodes and links of a node to itself are forbidden. For a general Newman-Watts small-world network, it is more convenient to use the fraction of added links $n/(NR)$ instead of the absolute number n. The probability p_{crit}, that of n added links, at least one spans a critical distance can be calculated using

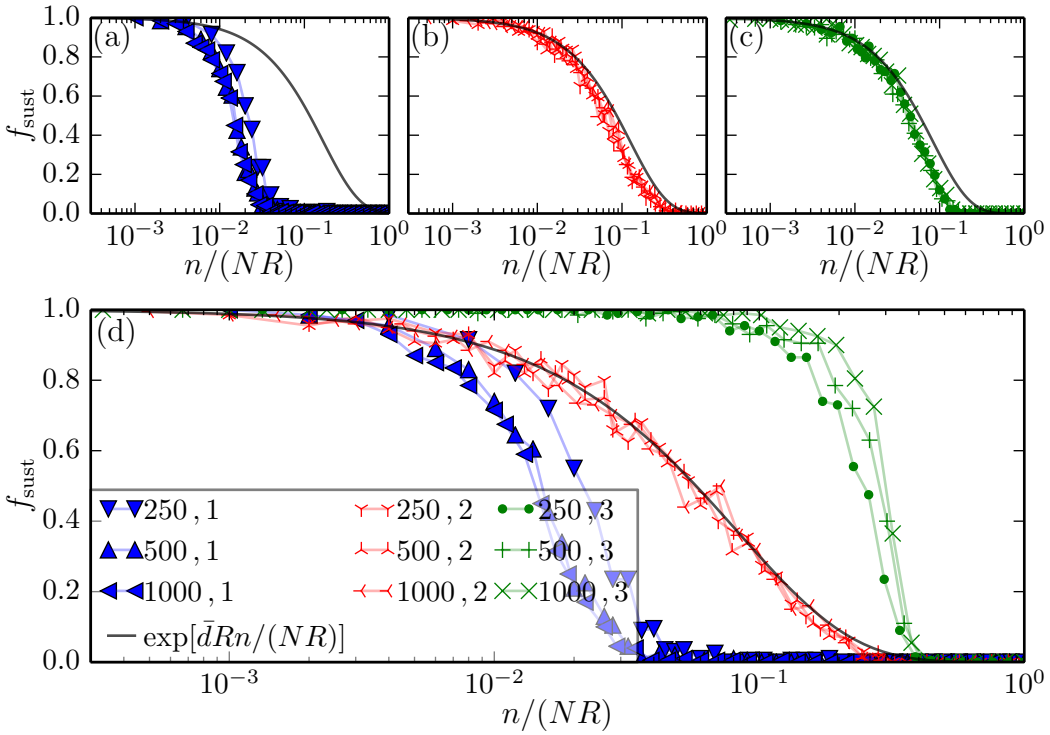

Figure 7.11: Fraction f_{sust} of realizations (with n additional long-range links) that support sustained activity of a traveling wave solution in the regime of inhibitor-mediated failure for different network sizes N. (a) $D = 0.035$ showing only networks with $R = 1$. (b) $D = 0.04$ showing only networks with $R = 2$. (c) $D = 0.02$ showing only networks with $R = 3$. (d) $D = 0.035$ showing networks with $R = 1, 2, 3$. Other parameters: $\varepsilon = 0.04$, $\beta = -1.1$.

the converse probability.

$$\begin{aligned} p_{\mathrm{crit}} &= \left(1 - \frac{\bar{d}}{N - 2R - 1}\right)^{n} \\ &= \left(1 - \frac{\bar{d}}{N - 2R - 1}\right)^{\left(\frac{n}{NR}\right)NR} \\ &\approx \exp\left\{-\bar{d}R\frac{n}{NR}\right\}, \end{aligned} \tag{7.2}$$

where the last approximation holds for large N.

As mentioned above, the range of distances for which inhibitor-mediated failure is present does only depend on the coupling strength D and on the coupling range R, and is independent of the network size N. Thus, in a plot of f_{sust} vs. $n/(NR)$, we expect networks with the same coupling range

R to show the exact same behavior in this region of the coupling strength. In Fig. 7.11 we have plotted f_{sust} vs. $n/(NR)$ for fixed coupling strengths well within the region of inhibitor-mediated failure. The measured curves for networks with the same coupling range R but different N coincide to very good approximation. For the values of Fig. 7.11(a), $R = 1$, $D = 0.035$, we have measured inhibitor-mediated failure for link distances $d = 3, 4, 5$ thus (taking into account the symmetry $d \leftrightarrow N - d$, cf. Sec. 6.1) $\bar{d} = 6$. The curve of p_{crit} for these values however gives a higher f_{sust} than observed (black curves). Presumably this is due to more complicated collective effects not taken into account for the simple calculation leading to Eq. (7.2). In Fig. 7.11(b), $R = 2$, $D = 0.04$. For these values we have found $\bar{d} = 4$ and p_{crit} for this value fits the observed behavior very well. So does the curve of p_{crit} in Fig. 7.11(c) for $R = 3$, $D = 0.02$, for which we measured $\bar{d} = 4$. In Fig. 7.11(d) f_{sust} for networks with $R = 1, 2, 3$ are shown together at a coupling strength $D = 0.035$. The curve of p_{crit} in that plot is for $\bar{d} = 6$ which is the value for $R = 2$ at this coupling strength. Note that $D = 0.035$ is above D_{2-} for $R = 3$ and so $\bar{d} = 0$, which would yield $p_{\text{crit}} = 1$. Thus we conclude that the decline of f_{sust} for $R = 3$ in Fig. 7.11(d) is solely due to more complicated collective effects.

One example for a higher order collective effect is shown in Fig. 7.7, where $N = 500$, $R = 1$, $n = 4$ and $D = 0.0373$. This value of the coupling strength is larger than D_2, and thus the generation of secondary wave pairs is possible. For these values a single link never leads to propagation failure. However in that example, two links end in node 142. When the traveling wave reaches this node at $t \approx 580$ (white vertical line in Fig. 7.7(b)), the other ends of both links point to an unexcited node and the joint backcoupling is enough to stop the wave. After that there is an even number of traveling waves left on the network and the system decays to the stable homogeneous state, when the last remaining wave pair has collided at $t \approx 880$.

To visualize that in the low-D regime, the collective effect of additional long-range links in a Newman-Watts small-world network on traveling waves does not depend on N we have collected all level curves $(n_{0.5}, D_{0.5})$ (defined by $f_{\text{sust}}(n_{0.5}, D_{0.5}) = 0.5$) for all investigated N and R in Figure 7.13(a). The level curves in that Figure have color assigned by their coupling range R and are plotted in the coordinates $n/(NR)$ vs. D. One clearly sees that lines with

the same R (i.e. the same color) lie on top of each other at small coupling strengths. Following these lines, starting at the lowest coupling strength $D_{0.5}$ and gradually increasing D, $n_{0.5}/(NR)$ increases quickly until it achieves a maximum value. After achieving this maximum value, $n_{0.5}/(NR)$ decreases and from a certain point, lines for different N start to diverge. Fig. 7.13(f) shows a blow up of the green marked region in Fig. 7.13(a). The remainder of this figure will be explained in the next section.

7.1.2 High coupling strength – continuum limit

Unlike in the case of low coupling strengths, in the regime of high coupling strengths D, we did not encounter any values of the coupling strength at which the behavior changes drastically for networks of different sizes N. Though propagation failure at high coupling strengths D can be caused by a single link, it is not possible to identify exact values of the coupling strength D or the 'virtual length' L (introduced by Eq. (4.13c) in Sec. 4.2.1 on page 47) at which the overall behavior caused by one link changes abruptly.

For small D, we found that networks with the same coupling range R and the same coupling strength D show the same behavior regardless of the network size N. We do not expect to find this behavior in the regime of large coupling strengths because in that case, as explained in Sec. 4.2.1, wave solutions on the regular ring network (without any additional links) are better described in terms of the virtual length L. But also the virtual length L does not provide a unifying description of the thresholds at high coupling strengths. In Fig. 7.12, we have compiled a collection of plots of f_{sust} employing both D and L as well as n and $n/(NR)$ for all investigated networks to illustrate the different thresholds. Figs. 7.12(a),(c) and (d) demonstrate that the coupling strength D is not well suited to unify the threshold curves at high coupling strengths. In Fig. 7.12(a), f_{sust} is plotted against $n/(NR)$ for a fixed value of the coupling strength $D = 10$. In Figs. 7.12(c) and (d), f_{sust} is plotted against D for a fixed value of additional links $n = 10$ (Fig. 7.12(c)) and for a fixed fraction of additional links $n/(NR) = 0.002$ (Fig. 7.12(d)). However, the virtual length L in combination with n or $n/(NR)$ is not well suited as a unifying parameter as one might suspect. This is demonstrated by Fig. 7.12(b), (e), and (f). In Fig. 7.12(b), f_{sust} is plotted vs. $n/(NR)$ for a fixed value of the virtual length

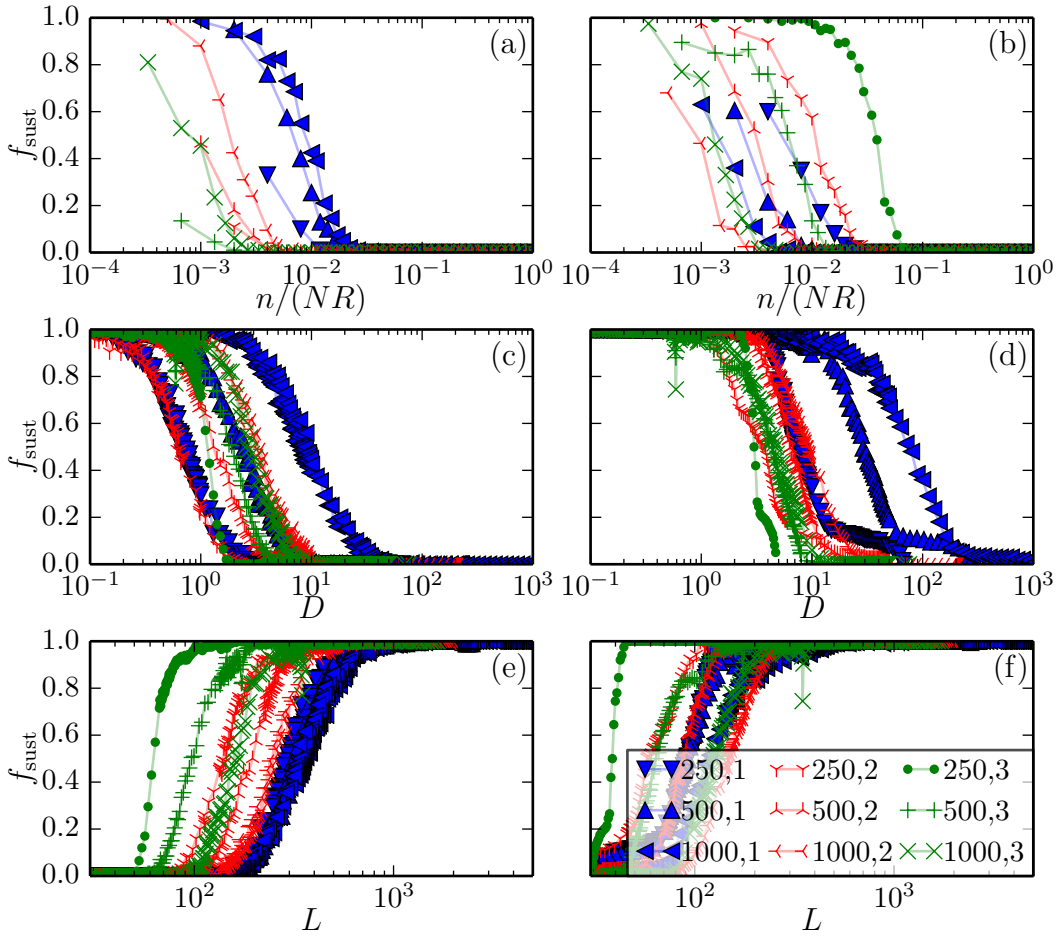

Figure 7.12: Transition from sustained wave activity to propagation failure in the high-D regime. (a) f_{sust} vs. $n/(NR)$ for $D = 10$. (b) f_{sust} vs. $n/(NR)$ for $L = 100$. (c) f_{sust} vs. D for $n = 10$. (d) f_{sust} vs. D for $n/(NR) = 0.002$. (e) f_{sust} vs. L for $n = 10$. (f) f_{sust} vs. L for $n/(NR) = 0.002$. In (c),(d),(e),(f), D (resp. L) values pertaining to the low-D regime are not shown for better readability. Other Parameters: $\varepsilon = 0.04$, $\beta = -1.1$.

$L = 100$. In Figs. 7.12(e) and (f), f_{sust} is plotted vs. L for the same fixed values of n and $n/(NR)$ as in Figs. 7.12(c) and (d).

To solve this problem and find out what quantities derived from D, n, N and R are well suited to provide a unifying description of the influence of additional links on wave propagation, we use the level curves $(n_{0.5}, D_{0.5})$. It is a simple matter to transform these curves to different coordinates. We have done so in Fig. 7.13(a) displaying the level curves (also called *threshold curves*

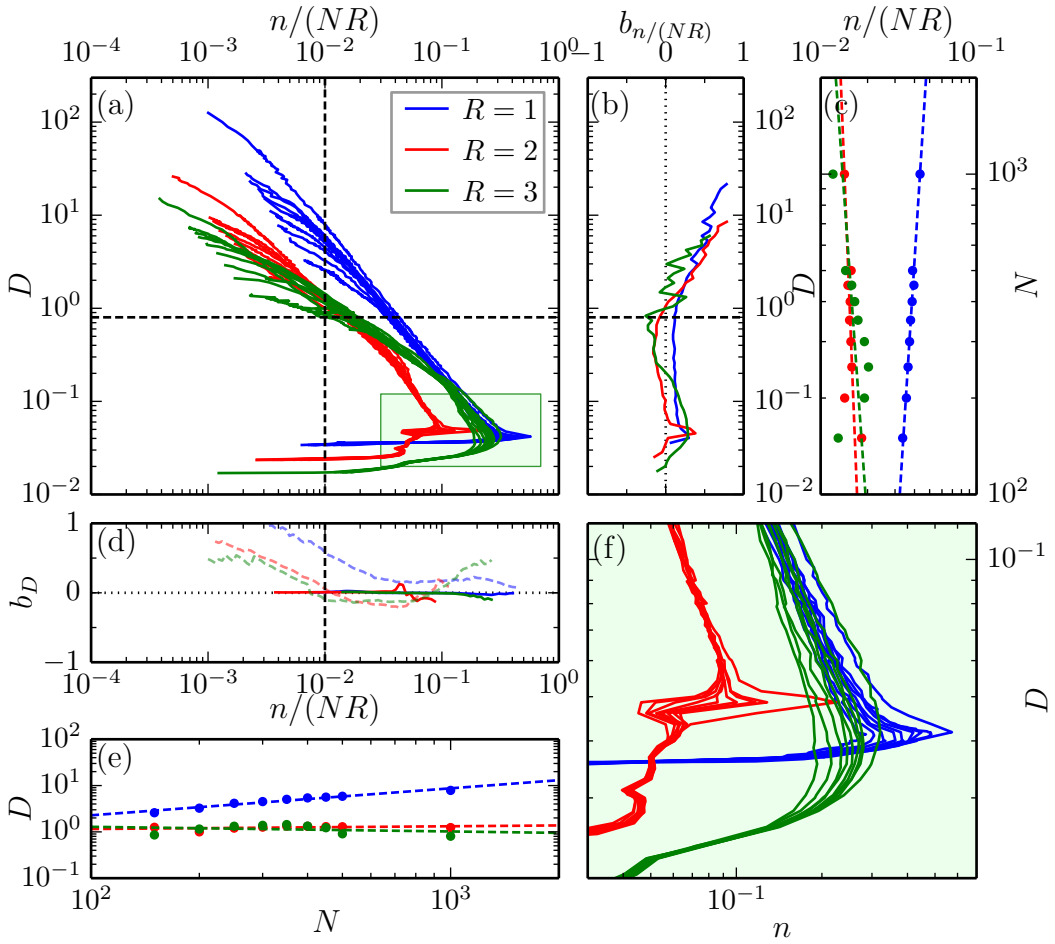

Figure 7.13: Scaling plot for D and n/NR. In all subplots, color indicates coupling range $R = 1$ (blue), $R = 2$ (red) and $R = 3$ (green). (a) Level curves $f_{\text{sust}}(n, D) = 0.5$ displayed in $n/(NR)$ vs. D for network sizes $N = 150, 200, 250, 300, 350, 400, 450, 500, 1000$ and coupling ranges $R = 1, 2, 3$. Network sizes are not indicated for readability, in each group of R, the maximum value of D increases with N. (b) N-scaling exponents for the fraction of additional links $b_{n/(NR)}$ vs. D. (c) $n_{0.5}/(NR)$ (dots) vs. N at $D = 0.8$ indicated by horizontal dashed line in (a) and (b) and linear fit to $n_{0.5}$ (dashed lines) for each R (slope gives $b_{n/(NR)}$). (d) N-scaling exponents for b_D vs. $n/(NR)$. low-D (solid lines) high D (dashed lines). (e) (high) $D_{0.5}$ (dots) vs. N at $n/(NR) = 10^{-2}$ indicated by vertical dashed line in (a) and (d). (f) blow-up of green marked region in (a). Other parameters $\varepsilon = 0.04$, $\beta = -1.1$.

from now on) in $n/(NR)$ vs. D (instead of n vs. D). In this depiction, as alreay mentioned in the previous section, the agreement of the threshold curves for the same R at low values of D indicates that the size N does not influence the location of the threshold at low coupling strengths. To find out how the size of the network influences the location of the threshold at high D, we 'cut' through the $(n/(NR), D)$ plane at a fixed value of $n/(NR)$, collecting the values $D_{0.5}$ of the intersections of this cut with the threshold lines (separately for each R). Next, we plot N against these values $D_{0.5}$ in a log-log plot. In other words, for given R and $n/(NR)$, we extract the pairs $(N, D_{0.5})$ for which $f_{\text{sust}}(D_{0.5}, n; N, R) = 0.5$. The (logarithm of the) obtained datapoints can be fit to a straight line to good approximation. We denote by b_D, the slope of this line for a fixed value of $n/(NR)$ (and R). Then, when using the coordinates DN^{-b_D} and $n/(NR)$ to plot the threshold lines, all of these with the same R will (almost) coincide at the chosen value $n/(NR)$. When changing the value $n/(NR)$ of the 'cut', the scaling exponent b_D can vary. A scaling exponent b_D that does not vary a lot indicates a general behavior in this region of $n/(NR)$. This procedure is visualized in Fig. 7.13(a) by visualizing the cut by a vertical dashed line. Note that a (vertical) line with fixed $n/(NR)$ shares two intersection points with each threshold curve, one at a high value of D and one at a low value of D. Fig. 7.13(e) by the log-log plot of the intersection points (at high D) including the linear fit. In all these plots, the procedure is applied separately for each R, labeling the outcomes for different R by color. In Fig. 7.13(d), the scaling exponents for $R = 1, 2, 3$ are plotted vs. $n/(NR)$. The scaling exponents for low-D are shown as solid lines whereas those for the high-D intersection points are shown as dashed lines. The scaling exponents b_D for the low-D intersections are constantly zero to very good approximation, thus confirming that in the low-D regime, N does not have an influence on the location of the threshold.

Of course, the same procedure can be employed using a fixed D instead of a fixed $n/(NR)$, yielding the scaling exponent $b_{n/(NR)}$. This is illustrated in Fig. 7.13(b) and (c). However, the obtained scaling exponents $b_{n/(NR)}$ show a strong dependence on D, thus indicating that D is not well suited for describing the threshold behavior in the high-D regime.

The picture changes drastically, when we take the coordinates L and n as

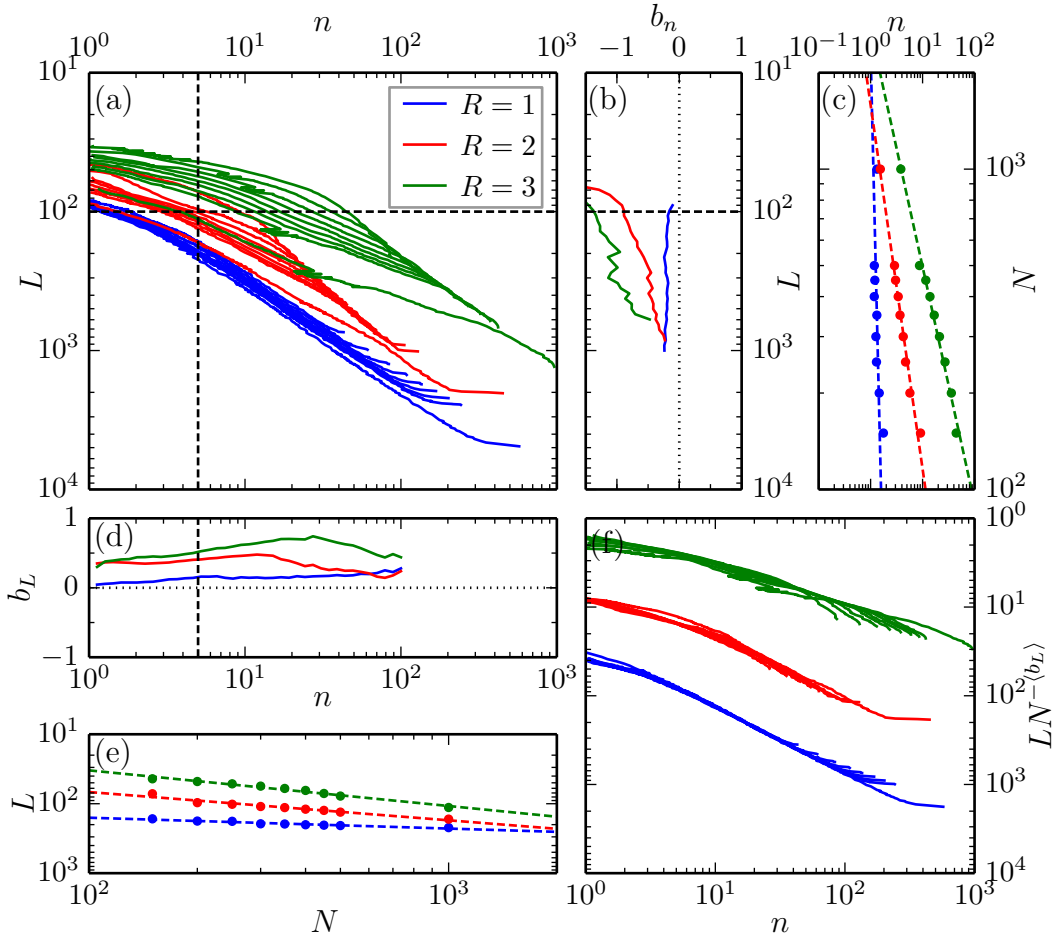

Figure 7.14: Scaling plot for L and n. In all subplots, color indicates coupling range $R = 1$ (blue), $R = 2$ (red) and $R = 3$ (green). (a) Level curves $f_{\text{sust}}(n, D) = 0.5$ displayed in n vs. L for network sizes $N = 150, 200, 250, 300, 350, 400, 450, 500, 1000$ and coupling ranges $R = 1, 2, 3$. Network sizes are not indicated for readability, in each group of R, N increases from top to bottom. Only the high-D part of the level curves is shown. (b) N-scaling exponents for the number of additional links b_n vs. L. (c) $n_{0.5}$ (dots) vs. N at $L = 100$ indicated by horizontal dashed line in (a) and (b) and linear fit to $n_{0.5}$ (dashed lines) for each R (slope gives b_n). (d) N-scaling exponents for b_L vs. n. (e) $L_{0.5}$ (dots) vs. N at $n = 5$ indicated by vertical dashed line in (a) and (d). (f) Level curves $f_{\text{sust}}(n, D) = 0.5$ displayed in n vs. $LN^{\langle b_L \rangle}$ Other parameters $\varepsilon = 0.04$, $\beta = -1.1$.

a starting point for this procedure. This is visualized in Fig. 7.14. For better readability, the low-D parts of all threshold lines are omitted in this Figure. In Fig. 7.14(c), the threshold points $n_{0.5}$ in dependence of N are plotted for a 'horizontal' cut at $L = 100$ and in Fig. 7.14(e), this is done for the threshold points $L_{0.5}$ in dependence of N for a 'vertical' cut at $n = 5$. The scaling parameter b_n in dependence on L is shown in Fig. 7.14(b) varying strongly over the displayed range for all $R = 2, 3$. The scaling parameter b_L in dependence on n is shown in Fig. 7.14(d) also not strictly constant but with very little variation over a large range of n. This indicates, that a modification of L alongside n is suitable to give a unifying description of the threshold behavior in the regime of large coupling strengths D. We have taken the average of the scaling parameter $\langle b_L \rangle$ over the range $n = 1, ..., 100$ (separately for each R) yielding values shown in Table 7.1. In Fig. 7.14(f) we have plotted the threshold curves for all considered N, R in the coordinate n and $LN^{-\langle b_L \rangle}$. In these coordinates, the threshold curves coincide to a good approximation.

We interpret the coordinate $LN^{-\langle b_L \rangle}$ at fixed values of the number n of additional links as an effective virtual length which is shorter than L due to the influence of the additional links. This is along the lines that the dispersion effects caused by a short virtual length L lead to an overall increase of the inhibitor level on the ring causing the failure of propagation below $L_{\min}$ (see Sec. 4.1.1). Additional links present on the ring also cause the inhibitor level to rise by sub-threshold excitations mediated through them. This also makes it clear why the scaling exponents differ for different R, namely because the effective weight of the additional links changes, when the coupling range R is changed.

R	1	2	3
$\langle b_L \rangle$	0.15	0.35	0.55

Table 7.1: Table of average scaling exponents $\langle b_L \rangle$ calculated as explained in Sec. 7.1.2. Parameters: $\varepsilon = 0.04$, $\beta = -1.1$.

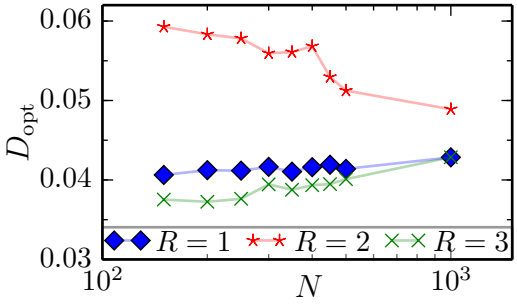

Figure 7.15: Values of the optimal coupling strength D_{opt}. Other parameters: $\varepsilon = 0.04$, $\beta = -1.1$.

7.1.3 Existence and measurement of optimum coupling strength

For a given n, when approaching either D_{min} or D_{max}, f_{sust} will go to zero. This is understandable in the context of Chapter 6, as very close to these values already for $n = 1$ there is propagation failure for all possible realizations. This observation alone leads to the conclusion that for some D between D_{min} and D_{max} there must be an optimum value D_{opt} for which the critical number n of additional links which marks the transition point is highest. We extract this point of the optimum coupling strength from the level curves $f_{\mathrm{sust}} = 0.5$ by fitting the level curves $(D_{0.5}, n_{0.5})$ (for all N and R under consideration) around the maximum of $n_{0.5}$ to a parabola and calculating the point of the maximum of this parabola. The obtained values of D_{opt} are shown in Fig. 7.15.

7.2 Mean-field approximation

In Sec. 4.2.1 we introduced the continuum limit for a ring network with diffusive coupling and coupling range R. In this continuum limit, the FitzHugh-Nagumo system on ring network system is described by a one dimensional FitzHugh-Nagumo reaction-diffusion system. In the following, we want to modify this description to incorporate the effect of the additional links of Eqs. (7.1). To this end, we split the adjacency matrix $\mathcal{A}_{ij}$ in Eq. (7.1a) into two parts. These are $\mathcal{A}_{ij} =: \mathcal{R}_{ij} + \mathcal{S}_{ij}$, with $\mathcal{R}_{ij}$ containing all links of the original ring network and $\mathcal{S}_{ij}$ containing the additional randomly added links. Thus, Eq. (7.1a)

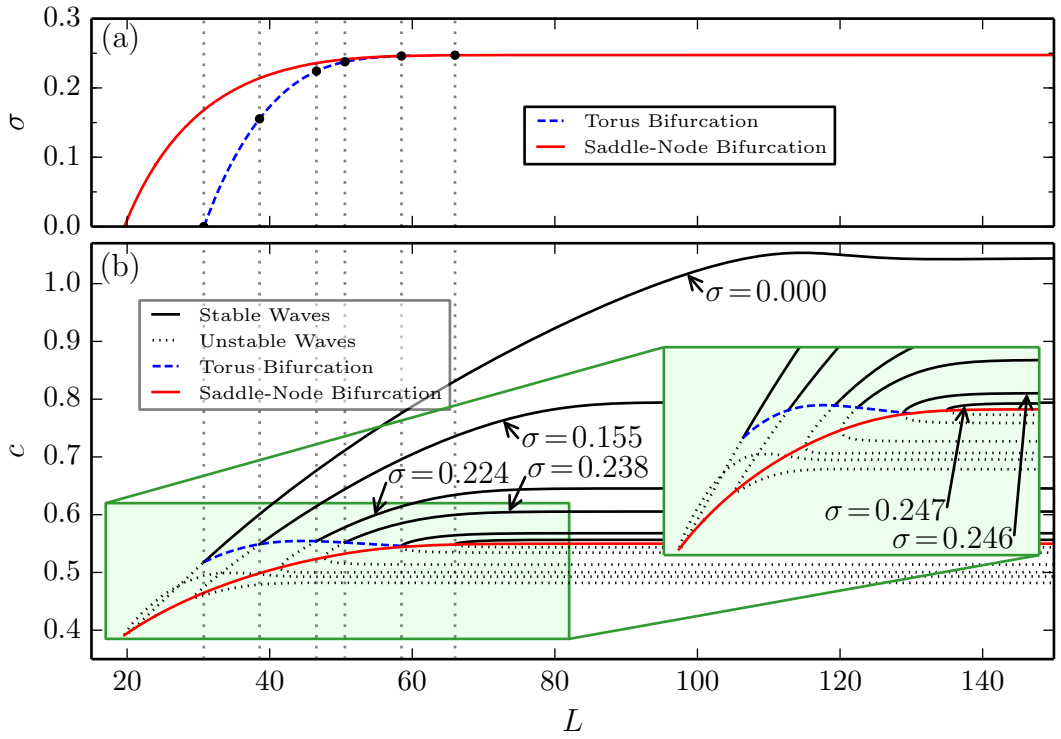

Figure 7.16: Dispersion relation for the mean-field approximation Eq. (7.4). (a) Curve of the destabilizing torus bifurcation at $L_{\min}$ (blue dashed) and of the saddle-node bifurcation (red solid) in (L, σ) space. Black dots indicate the (L, σ) values of the destabilization points in the dispersion relations shown in (b). (b) Propagation velocity c vs L: branches of stable (black solid) and unstable (black dotted) traveling waves for different values of mean-field coupling strength σ, curves of destabilizing torus bifurcation (blue dashed), and curve of the saddle-node bifurcation (red solid) in (L, c) space. The inset shows a blow-up of the green rectangle. Parameters: $\beta = -1.1,\ \varepsilon = 0.04$.

(Eq. (7.1b) is omitted for readability) reads

$$\begin{aligned}
\dot{u}_i &= u_i - \frac{u_i^3}{3} - v_i + D\left(\sum_{j=1}^{N} \mathcal{R}_{ij}(u_j - u_i) + \sum_{j=1}^{N} \mathcal{S}_{ij}(u_j - u_i)\right) \\
&= u_i - \frac{u_i^3}{3} - v_i + D\sum_{j=1}^{R}(u_{i+j} + u_{i-j} - 2u_i) + D\sum_{j=1}^{N} \mathcal{S}_{ij}(u_j - u_i) \\
&= u_i - \frac{u_i^3}{3} - v_i + \frac{\tilde{D}}{q(R)}\sum_{j=1}^{R}(u_{i+j} + u_{i-j} - 2u_i) + \frac{\tilde{D}}{q(R)}\sum_{j=1}^{N} S_{ij}(u_j - u_i)
\end{aligned} \tag{7.3}$$

where in the last equality a rescaling $D \to \tilde{D} = Dq(R)$ has been used, and the tilde will be dropped in the following.

The ring part of the coupling can be treated in the same way as in Sec. 4.2.1. We treat the small-world part of the coupling by doing the ensemble average over all realizations with a fixed number of additional links at this point. Thus, in the limit of $N \to \infty$, $\mathcal{S}_{ij}$ becomes a constant $\mathcal{S}_{ij} \to \frac{2n}{N^2}$.

For easier readability, we consider only the small-world part of the coupling term in Eq. (7.3).

$$\begin{aligned} s_i &:= \frac{D}{q(R)} \sum_{j=1}^{N} \mathcal{S}_{ij}(u_j - u_i) \\ &\to \frac{1}{q(R)} \frac{N^2}{L^2} \sum_{j=1}^{N} \left(\frac{2n}{N^2}(u_j - u_i) \right) \\ &= \frac{1}{q(R)} \frac{2n}{L^2} \sum_{j=1}^{N} (u_j - u_i) \end{aligned}$$

In performing the transition to the continuum description, we replace the sum $\sum_{j=1}^{N}$ by the integral $\int_0^L dy$ and introduce the mean value $\bar{u}$. Also, s_i becomes a function $s(x)$:

$$\begin{aligned} s(x) &= \frac{1}{q(R)} \frac{2n}{L^2} \left(\int_0^L u(y)dy - \int_0^L u(x)dy \right) \\ &= \frac{1}{q(R)} \frac{2n}{L} \left(\bar{u} - u(x) \right) \end{aligned}$$

Thus, the continuum limit description including the additional long-range links reads

$$\partial_t u = u - \frac{u^3}{3} - v + \ u_{xx} + \sigma(\bar{u} - u) \tag{7.4a}$$

$$\partial_t v = \varepsilon(u - \beta), \tag{7.4b}$$

$x \in [0, L]$ and periodic boundary conditions $u(t, 0) = u(t, L)$, $v(t, 0) = v(t, L)$ with $L = \frac{N}{\sqrt{q(R)D}}$ and $\sigma = \frac{2n}{q(R)L}$. The double subscript u_{xx} denotes the second derivative with respect to the spatial variable x. Note that this kind of global feedback coupling has also been studied for the Rinzel-Keller model in [102].

If $\sigma = 0$, Eqs. (7.4) are the same as Eqs. (4.1) (p. 38). Employing the same methods as in Sec. 4.1.1, we examine the change of the dispersion relation $c(L)$ if σ is increased, see Fig. 7.16.

For $\sigma = 0$, the destabilization happens via a torus bifurcation at $L_{\mathrm{cr}}(\sigma = 0) = L_{\mathrm{min}}$. If σ is increased, L_{cr} increases as well, i.e., the parameter range of L for stable propagation becomes smaller (Fig. 7.16(a)). At a certain value of $\sigma \approx 0.246$, the mechanism of destabilization changes, when the torus bifurcation coincides with a saddle-node bifurcation (limit point), see inset of Fig. 7.16(b). After that, the destabilization happens by a saddle-node bifurcation. However, the σ value of the locus of the destabilizing saddle-node bifurcation goes into saturation at a value of $\sigma_{\mathrm{max}} \approx 0.247$. This means that L_{cr} goes to infinity when σ approaches σ_{max} from below so that above σ_{max}, no stable propagation is possible. We display these loci of destabilization as a curve $\sigma_0(L)$ in Fig. 7.16(a). This curve can be transformed to a curve $n_0(N, R, D)$, yielding an approximation for the boundary in n above which no realizations of a small-world network will support stable traveling waves. The curve $L_{cr}(\sigma)$ in (a) is connected with the instability points of the dispersion relations shown in Fig. 7.16(b) as indicated by the vertical dotted lines.

In Figs. 7.5 and 7.6, f_{sust} is shown in the entire range of D and n for $N = 1000$ and $R = 1, 2, 3$ as well as for $N = 200$, $R = 2$. Also shown in these plots as a green solid line is the analytical curve $n_0(D)$ for the respective values of N and R which would give the expected maximum long-range link number. The transition in n to quenched wave activity happens at lower values of n. This is expected, as a significant contribution by the coupling term arising through the long-range links can only occur if the difference in activator concentration at both ends of the link is large. This is only the case if the node at one end of the shortcut is in the excited state (wave peak). Thus the critical link density is only important in part of the network. Of course, in the small-world network, the local density of the additional links is fluctuating and thus a critical density can be exceeded in (an arbitrary) part of the network even though this density averaged over the entire network is below the critical density.

Also, note that the approximation becomes worse for higher R. In the continuum description of the ring without any additional links, the three parameters of the ring network N, R, and D are reduced to one parameter L, the domain size of the reaction diffusion system. In the high-D regime on the ring network, increasing R or D has the same effect (and only this effect) of

decreasing the length of the corresponding reaction-diffusion system. When additional long-range links are added to the system, this does not hold anymore. Increasing R has the additional effect of decreasing the effective weight of the long-range links, as the ring network is locally connected by R links in each direction but each added long-range connection consists of just one link. This effect has not been included in our mean-field approximation. Therefore, the mean-field approximation for the small-world network reduces the four parameters describing the network and the coupling on the network (N, R, D, and n) to two parameters (L and σ) and the approximation works best for $R = 1$.

Chapter 8

Conclusion

In this thesis, we have studied the propagation of excitation waves on network organized FitzHugh-Nagumo systems and the influence of certain aspects of network topology on the propagation of excitation waves. We reviewed the basic concepts and materials from complex network theory and for the FitzHugh-Nagumo differential equation needed in Chapters 2 and 3. We have discussed in some detail the propagation of excitation waves on regular lattice networks in Chapter 4. We have calculated the full dispersion relation for excitation waves on a ring network, we discussed the continuum limit at high coupling strengths and the discrete limit at low coupling strengths.

After these preliminary Chapters, we have studied excitation wave propagation on regular tree networks in Chapter 5. We have discovered that for tree networks there exists a critical branching ratio respectively a critical degree of the non-leaf nodes at which a branch of stable waves and a branch of unstable waves collide in a saddle-node bifurcation. Above this critical degree, no propagation of excitation waves is possible. The value of the critical degree is dependent on the global coupling strength. We have explored this dependence using an approximate continuum system, profile equations and kinematical theory in the continuum limit, and were able to calculate the critical degree and the velocity of the waves with these methods. In the low coupling strength discrete regime, we used numerical continuation of the full system and the so-called active-point approximation to calculate the dependence of the critical degree on the coupling strength in this regime. We found that the critical coupling strength exhibits an optimum value at which the critical branching ratio

becomes maximum. Using the active point approximation, we could predict the value of this optimum coupling strength.

In Chapter 6, we have studied excitation wave propagation on minimal small-world networks, which are ring networks with one additional link. We discovered that the one additional link facilitates a host of different spatio-temporal behaviors including propagation failure, period multiplication, and mechanisms that break and reinstall a symmetry of the underlying network. We discussed all discovered behaviors in some detail and could identify and elucidate the different underlying dynamical mechanisms. We found that the spatio-temporal behavior can be selected by varying just two parameters, the global coupling strength and the distance the additional link spans. We were able to give an overview of all different behaviors in just one single quantity, i.e., the relative period. We found threshold values of the coupling strength at which the behavior of the system changes drastically. By using analytical methods, we successfully tried to approximate the locations of these threshold values. We also discovered that the size and the coupling range of the underlying ring network have an impact on which patterns are achievable at all. We studied the scaling behavior with respect to network size and coupling range and found three different regimes of the coupling strength in which this behavior differs. The scaling behavior in the low and high coupling strength regime could be explained qualitatively, the behavior for intermediate coupling strengths remains somewhat peculiar as we do not have a good explanation for its causes.

Our results concerning the influence of small-world topologies on excitation wave propagation are found in Chapter 7. In agreement with the work of other authors we found that increasing the number of long-range links impedes wave propagation. We also found a transition from supporting wave propagation to quenched propagation that is happening within a narrow range of the number of additional long-range links. We have studied this system for the full range of admissible values of the coupling strength. We were able to use results from the previous chapter to calculate the fraction of network realizations that support wave propagation in the regime of very low coupling strengths. In the high coupling strength continuum regime, we used a numerical meta-analysis to examine the scaling behavior of the system. We found that the influence

of the additional links manifests itself in a shortening of the effective length of the system. We could describe this by means of a numerically calculated scaling exponent. We were also able to construct a mean-field description with which we could predict the critical number of additional links at the transition to quenched wave propagation.

Comparing the contents of this thesis with the goals described in Sec. 1.4, we can state the following: In employing the FitzHugh-Nagumo dynamics, we used a generic, continuous time model throughout this work. Moreover, all our networks were bidirectional, which enabled us to construct continuum descriptions in Chapters 4, 5 and 7. In Chapter 4 we calculated the dispersion relation for excitation waves on a discrete lattice, showing that this consists of a closed curve, something that we did not find in the literature in this form before. By this, we worked out the range of admissible coupling strengths for those networks that are based on a ring network. For these, we studied the behavior over this entire range of the coupling strength. For all our model systems we compared solutions in the low and in the high coupling strength regime, finding differences in the shape of the solutions and in the behavior of eventual transition points. We were able to apply suitably modified versions of the analytical method from [33] in the context of regular tree networks in Sec. 5.3.2 and minimal small-world networks in Sec. 6.4. In the context of tree networks, we were able to predict quite precisely the behavior of the critical degree with varying coupling strength. In the context of minimal small-world networks, the analytical calculation of critical values and the numerically determined values showed some divergence which is most likely due to the time scale separation being not strong enough.

Using regular tree networks, we were able to identify the influence of the nodes degree on the propagation of excitation waves. By studying regular tree networks, we could also answer the question of how an excitation can reach as many nodes as possible within a certain time. This is achieved by tuning the coupling strength to the optimum value found in Chapter 5. We were also able to apply the results for regular tree networks to the early phase of excitation wave propagation on random networks, predicting the degree of the node at which a propagating wave stops.

Studying minimal small-world networks, we could answer the question whether

one additional link suffices to induce propagation failure with yes. We could elucidate the mechanism by which it does so and name the conditions for this behavior. Moreover, one additional link proved to be enough to trigger many other interesting spatiotemporal patterns and the study of excitation waves on minimal small-world networks turned out to be much more than a preliminary study for the propagation of excitation waves on small-world networks.

In the study of Newman-Watts small-world networks, we were able to use some of the results attained in the context of minimal small-world networks to understand and predict the behavior of excitation waves on small-world networks in the regime of low coupling strengths. We studied the influence of small-world topologies on excitation wave propagation on the entire range of admissible coupling strengths. The influence of the network size in the regime of low coupling strengths could be well understood. In the regime of high coupling strength we could describe the scaling behavior but a deeper (possibly analytical) understanding is yet to be explored. The same holds for the influence of the coupling range.

Putting the results of this thesis in the context of the previous work by other authors discussed in Sec. 1.3, we can state the following: To the best of our knowledge, the propagation of excitation waves on regular tree networks has not been studied before at all. Propagation failure due to very low coupling strengths for waves on lattices has been found in the literature [33, 34] before, but we are not aware of publications that put this in the context of a dispersion relation, demonstrating that the destabilization point is of saddle-node characteristic and that the same two branches of unstable and stable waves reunite again at high coupling strengths, thus forming a dispersion relation described by a closed curve. Excitation waves on minimal small-world networks have not been studied in that form before. Propagation failure of excitation waves due to small-world modifications of the topology has been reported before in [25] and [26]. However, to the best of our knowledge we were the first that described different regimes of the coupling strength in that context, took different coupling ranges into account and constructed a mean-field model in this context.

Despite these achievements, some points could not be explored as well as we would have wished. This is especially true for the influence of the coupling

range in minimal small-world and small-world networks. In these contexts we were able to describe the influence and to some extent qualitatively understand it but a derivation is yet to be explored. This holds also true for the mean-field approximation in the context of small-world networks which does not work too well for coupling ranges larger than unity.

Our results could be applied in some different contexts: The study of excitation networks on trees showed how the coupling strength needs to be tuned to reach as many nodes as possible within a certain time. The different patterns that excitation waves on minimal small-world networks exhibit and the easy selection of patterns by adjusting just two parameters makes this a good system to use as a simple pattern generator.

Future research could focus on the influence of the coupling range which remained less understood. Moreover, it would be interesting to investigate the differences, when instead of the FitzHugh-Nagumo model which describes excitability type-II, a model of excitability type-I is used. It is known that the dispersion relation for type-I systems shows different properties than that of type-II systems [62], and thus on networks some hitherto unknown behavior could be encountered. One could also pose the question whether and how it is possible, to tune parameters of individual nodes by means of control algorithms to overcome propagation failure caused by long-range links in (minimal) small-world network topologies. We also think that it would be interesting to try to set up a continuum model for minimal small world networks in which the distance that the additional link spans becomes a continuous parameter. This way, one could use numerical continuation algorithms to investigate the transitions in this model in more detail and work out the location of those transitions as continuous curves. Also, from a more general perspective it could be promising to investigate systems that exhibit a traveling wave instability as in [103] on networks, gradually breaking translational symmetries by introducing long-range links.

Appendix A

List of symbols

Symbol	Explanation	Eq./Sec.	p.
$k/k_i^{\text{in}}/k_i^{\text{out}}$	(in/out) degree of a node	Eq. (2.2)	13
N	Network size	Sec. 2.1	12
$\mathcal{A}_{ij}$	adjacency matrix	Eq. (2.1)	13
R	coupling range	Sec. 2.3.1	17
u, v	activator and inhibitor	Eqs. (3.1)	25
β	threshold parameter	Eqs. (3.1)	25
ε	timescale separation parameter	Eqs. (3.1)	25
u_0, v_0	steady state of the FitzHugh-Nagumo system	Eq. (3.3)	26
$\tilde{u}$, $\tilde{v}$	wave profile	Sec. 4.1	38
c	propagation velocity	Sec. 4.1	38
ξ	comoving frame coordinate	Sec. 4.1.1	39
L_{min}	minimum domain length for stable wave propagation	Sec. 4.1.2	40
D	global coupling strength	Eq. (4.7)	46
D_{min}	minimum coupling strength for stable wave propagation	Sec. 4.2.2	48
L	virtual length	Eq. (4.13c)	48
$q(R)$	influence of coupling range	Eq. (4.12)	48
D_{max}	maximum coupling strength for stable wave propagation	Eq. (4.14)	48
d	distance of additional link	Sec. 6.1	78
$\vartheta_d(D)$	relative period	Eq. (6.3)	81
D_1	transition value	Sec. 6.2.2	83
D_2	transition value	Sec. 6.2.3	84
D_{2-}	transition value	Sec. 6.2.3	84
n	number of additional links	Sec. 7.1	108
f_{sust}	fraction of realizations supporting sustained wave activity	Sec. 7.1	108
n_α, D_α	level curves	Sec. 7.1	108

Bibliography

[1] J. M. Davidenko, A. M. Pertsov, R. Salomonsz, W. Baxter, and J. Jalife: *Stationary and drifting spiral waves of excitation in isolated cardiac muscle*, Nature **355**, 349 (1992).

[2] A. T. Winfree: *When Time Breaks Down: The Three-Dimensional Dynamics of Electrochemical Waves and Cardiac Arrhythmias* (Princeton University Press, Princeton, NJ, 1987).

[3] H. L. Swinney and V. I. Krinsky (Editors): *Waves and Patterns in Chemical and Biological Media* (Physica D **49**, 1-256, 1991).

[4] J. P. Keener and J. J. Tyson: *Spiral waves in the Belousov-Zhabotinskii reaction*, Physica D **21**, 307 (1986).

[5] E. M. Nicola, M. Bär, and H. Engel: *Wave instability induced by nonlocal spatial coupling in a model of the light-sensitive belousov-zhabotinsky reaction*, Phys. Rev. E **73**, 066225 (2006).

[6] S. Brand, M. A. Dahlem, V. M. F. de Lima, S. C. Müller, and W. Hanke: *Dispersion relation of spreading depression waves in the chicken retina*, Int. J. Bifurcation Chaos **7**, 1359 (1997).

[7] M. A. Dahlem and T. M. Isele: *Transient localized wave patterns and their application to migraine*, J. Math. Neurosci **3**, 7 (2013).

[8] F. Kneer, E. Schöll, and M. A. Dahlem: *Nucleation of reaction-diffusion waves on curved surfaces*, New J. Phys. **16**, 053010 (2014).

[9] M. A. Dahlem, F. M. Schneider, and E. Schöll: *Failure of feedback as a putative common mechanism of spreading depolarizations in migraine and stroke*, Chaos **18**, 026110 (2008).

[10] F. M. Schneider, E. Schöll, and M. A. Dahlem: *Controlling the onset of traveling pulses in excitable media by nonlocal spatial coupling and time delayed feedback*, Chaos **19**, 015110 (2009).

[11] C. A. Bachmair and E. Schöll: *Nonlocal control of pulse propagation in excitable media*, Eur. Phys. J. B p. in print (2014), arXiv1404.4289.

[12] J. Siebert, S. Alonso, M. Bär, and E. Schöll: *Dynamics of reaction-diffusion patterns controlled by asymmetric nonlocal coupling as limiting case of differential advection*, Phys. Rev. E **89**, 052909 (2014).

[13] J. Löber, R. Coles, J. Siebert, H. Engel, and E. Schöll: *Control of chemical wave propagation*, in *Engineering of Chemical Complexity II*, edited by A. S. Mikhailov and G. Ertl (World Scientific, Singapore, 2014), arXiv:1403.3363.

[14] S. H. Strogatz: *Exploring complex networks*, Nature **410**, 268 (2001).

[15] Y.-Y. Liu, J.-J. Slotine, and A. L. Barabasi: *Controllability of complex networks*, Nature **473**, 167 (2011).

[16] J. Lehnert, T. Dahms, P. Hövel, and E. Schöll: *Loss of synchronization in complex neural networks with delay*, Europhys. Lett. **96**, 60013 (2011).

[17] T. Dahms, J. Lehnert, and E. Schöll: *Cluster and group synchronization in delay-coupled networks*, Phys. Rev. E **86**, 016202 (2012).

[18] D. P. Rosin, D. Rontani, D. J. Gauthier, and E. Schöll: *Control of synchronization patterns in neural-like Boolean networks*, Phys. Rev. Lett. **110**, 104102 (2013).

[19] S. Boccaletti, V. Latora, Y. Moreno, M. Chavez, and D. U. Hwang: *Complex networks: Structure and dynamics*, Phys. Rep. **424**, 175 (2006).

[20] M. E. J. Newman: *The structure and function of complex networks*, SIAM Review **45**, 167 (2003).

[21] M. E. J. Newman, A. L. Barabasi, and D. J. Watts: *The Structure and Dynamics of Networks* (Princeton University Press, Princeton, USA, 2006).

[22] H. Nakao and A. S. Mikhailov: *Turing patterns in network-organized activator–inhibitor systems*, Nature Physics **6**, 544 (2010).

[23] N. E. Kouvaris, H. Kori, and A. S. Mikhailov: *Traveling and pinned fronts in bistable reaction-diffusion systems on network*, PLoS ONE **7(9)**, e45029 (2012).

[24] C. R. Laing: *Fronts and bumps in spatially extended Kuramoto networks*, Physica D **240**, 1960 (2011).

[25] A. Roxin, H. Riecke, and S. A. Solla: *Self-sustained activity in a small-world network of excitable neurons*, Phys. Rev. Lett. **92**, 198101 (2004).

[26] S. Sinha, J. Saramäki, and K. Kaski: *Emergence of self-sustained patterns in small-world excitable media*, Phys. Rev. E **76**, 015101(R) (2007).

[27] V. A. Davydov, N. Manz, O. Steinbock, and S. C. Müller: *Critical properties of excitation waves on curved surfaces: Curvature-dependent loss of excitability*, Europhys. Lett. **59**, 344 (2002).

[28] V. A. Davydov, V. G. Morozov, and N. V. Davydov: *Critical properties of autowaves propagating on deformed cylindrical surfaces*, Physics Letters A **307**, 265 (2003).

[29] V. A. Davydov, N. Manz, O. Steinbock, V. S. Zykov, and S. C. Müller: *Excitation fronts on a periodically modulated curved surface*, Phys. Rev. Lett. **85**, 868 (2000).

[30] J. Maselko and K. Showalter: *Chemical waves in inhomogeneous excitable media*, Phys. D **49**, 21 (1991).

[31] M. E. J. Newman and D. J. Watts: *Renormalization group analysis of the small-world network model*, Phys. Lett. A **263**, 341 (1999).

[32] D. J. Watts and S. H. Strogatz: *Collective dynamics of 'small-world' networks*, Nature **393**, 440 (1998).

[33] A. Carpio: *Wave trains, self-oscillations and synchronization in discrete media*, Physica D: Nonlinear Phenomena **207**, 117 (2005).

[34] V. Booth and T. Erneux: *Understanding propagation failure as a slow capture near a limit point*, SIAM J. Appl. Math. **55**, 1372 (1995).

[35] D. R. Chialvo: *Generic Excitable Dynamics on a Two-dimensional Map*, Chaos, Solitons & Fractals **5**, 461 (1995).

[36] A. S. Mikhailov and V. S. Zykov: *Kinematical theory of spiral waves in excitable media: comparison with numerical simulations*, Physica D **52**, 379 (1991).

[37] D. B. West: *Introduction to Graph Theory (2nd Edition)* (Prentice Hall, 1995).

[38] L. Euler: *Solutio problematis ad geometriam situs pertinentis*, Commentarii academiae scientiarum Petropolitanae **8**, 128 (1741).

[39] R. Albert and A. L. Barabasi: *Statistical mechanics of complex networks*, Rev. Mod. Phys. **74**, 47 (2002).

[40] Y.-Y. Liu, E. Csóka, H. Zhou, and M. Pósfai: *Core percolation on complex networks*, Phys. Rev. Lett. **109**, 205703 (2012).

[41] D. S. Callaway, M. E. J. Newman, S. H. Strogatz, and D. J. Watts: *Network robustness and fragility: Percolation on random graphs*, Phys. Rev. Lett. **85**, 5468 (2000).

[42] J. M. Montoya, S. L. Pimm, and R. V. Solé: *Ecological networks and their fragility*, Nature **442**, 259 (2006).

[43] E. T. Bullmore and O. Sporns: *The economy of brain network organization*, Nature Reviews Neuroscience **13**, 336 (2012).

[44] H. Jeong, S. P. Mason, A. L. Barabasi, and Z. N. Oltvai: *Lethality and centrality in protein networks*, Nature **411**, 41 (2001).

[45] R. Albert, I. Albert, and G. L. Nakarado: *Structural vulnerability of the North American power grid*, Phys. Rev. E **69**, 025103 (2004).

[46] S. A. Gerschgorin: *Über die Abgrenzung der Eigenwerte einer Matrix*, Izv. Akad. Nauk. SSSR **6**, 749 (1931).

[47] N. Ganguly, A. Deutsch, and A. Mukherjee: *Dynamics on and of Complex Networks: Applications to Biology, Computer Science, and the Social Sciences* (Birkhauser, Basel, 2009).

[48] D. Hebb: *The Organization of Behavior: A Neuropsychological Theory* (Wiley, New York, 1949), new edition ed.

[49] L. M. Pecora and T. L. Carroll: *Master stability functions for synchronized coupled systems*, Phys. Rev. Lett. **80**, 2109 (1998).

[50] D. Rosa: *The Life and Times of Scrooge McDuck (softcover) 1* (Gemstone, 2005), p. 210.

[51] P. Erdős and A. Rényi: *On random graphs*, Publ. Math. Debrecen **6**, 290 (1959).

[52] P. Erdős and A. Rényi: *On the evolution of random graphs*, Publ. Math. Inst. Hung. Acad. Sci **5**, 17 (1960).

[53] S. Milgram: *The Small-World Problem*, Psychology Today **106**, 61 (1967).

[54] R. Monasson: *Diffusion, localization and dispersion relations on"small-world" lattices*, Eur. Phys. J. B **12**, 555 (1999).

[55] M. E. J. Newman and D. J. Watts: *Scaling and percolation in the small-world network model*, Phys. Rev. E **60**, 7332 (1999).

[56] A. Barrat and M. Weigt: *On the properties of small-world network models*, Eur. Phys. J. B **13**, 547 (2000).

[57] M. Brede: *Small worlds in space: Synchronization, spatial and relational modularity*, EPL **90**, 60005 (2010).

[58] C. Grabow, S. M. Hill, S. Grosskinsky, and M. Timme: *Do small worlds synchronize fastest?*, Europhys. Lett. **90**, 48002 (2010).

[59] S. Sinha: *Complexity vs. stability in small-world networks*, Physica A **346**, 147 (2005).

[60] Y. Liu, M. Liang, Y. Zhou, Y. He, Y. Hao, M. Song, C. Yu, H. Liu, Z. Liu, and T. Jiang: *Disrupted small-world networks in schizophrenia*, Brain **131**, 945 (2008).

[61] A. L. Hodgkin: *The local electric changes associated with repetitive action in a medullated axon*, J. Physiol. **107**, 165 (1948).

[62] G. B. Ermentrout and D. Terman: *Mathematical Foundations of Neuroscience* (Springer, 2010).

[63] E. M. Izhikevich: *Dynamical Systems in Neuroscience* (MIT Press, Cambridge, MA, 2007).

[64] C. Otto: *Dynamics of Quantum Dot Lasers – Effects of Optical Feedback and External Optical Injection*, Springer Theses (Springer, Heidelberg, 2014).

[65] C. Otto, B. Lingnau, E. Schöll, and K. Lüdge: *Manipulating coherence resonance in a quantum dot semiconductor laser via electrical pumping*, Opt. Express **22**, 13288 (2014).

[66] J. Rinzel and G. B. Ermentrout: *Analysis of neural excitability and oscillations*, in *Methods in neuronal modeling*, edited by C. Koch and I. Segev (MIT Press, Cambridge, MA, 1989), pp. 251–291.

[67] R. FitzHugh: *Impulses and physiological states in theoretical models of nerve membrane*, Biophys. J. **1**, 445 (1961).

[68] J. Nagumo, S. Arimoto, and S. Yoshizawa.: *An active pulse transmission line simulating nerve axon.*, Proc. IRE **50**, 2061 (1962).

[69] A. L. Hodgkin and A. F. Huxley: *A quantitative description of membrane current and its application to conduction and excitation in nerve*, J. Physiol. **117**, 500 (1952).

[70] J. Guckenheimer and C. Kuehn: *Homoclinic Orbits of the FitzHugh-Nagumo Equation: Bifurcations in the Full System*, SIAM J. Appl. Dyn. Syst. **9**, 138 (2010).

[71] T. Kostova, R. Ravindran, and M. Schonbek: *Fitzhugh-nagumo revisited: Types of bifurcations, periodical forcing and stability regions by a lyapunov functional*, Int. J. Bifurcation Chaos **14**, 913 (2004).

[72] N. Buric and D. Todorovic: *Dynamics of FitzHugh-Nagumo excitable systems with delayed coupling*, Phys. Rev. E **67**, 066222 (2003).

[73] M. Krupa, B. Sandstede, and P. Szmolyan: *Fast and Slow Waves in the FitzHugh-Nagumo Equation*, J. Diff. Eq. **133**, 49 (1997).

[74] H. Feddersen, P. L. Christiansen, and M. P. Soerensen: *Global bifurcations in the FitzHugh-Nagumo equations for nerve wave propagation*, Journal of Biological Physics **17**, 271 (1990).

[75] B. Lindner, J. García-Ojalvo, A. B. Neiman, and L. Schimansky-Geier: *Effects of noise in excitable systems*, Phys. Rep. **392**, 321 (2004).

[76] E. M. Izhikevich and R. A. FitzHugh: *FitzHugh-Nagumo model*, Scholarpedia **1**, 1349 (2006).

[77] C. K. R. T. Jones: *Geometric singular perturbation theory*, in *Dynamical Systems* (Springer Berlin Heidelberg, 1995), vol. 1609 of *Lecture Notes in Mathematics*.

[78] N. Fenichel: *Geometric singular perturbation theory for ordinary differential equations*, J. Diff. Eq. **31**, 53 (1979).

[79] F. Schlögl: *Chemical reaction models for non-equilibrium phase transitions*, Z. Phys. **253**, 147 (1972).

[80] E. Schöll, G. Hiller, P. Hövel, and M. A. Dahlem: *Time-delayed feedback in neurosystems*, Phil. Trans. R. Soc. A **367**, 1079 (2009).

[81] S. A. Brandstetter, M. A. Dahlem, and E. Schöll: *Interplay of time-delayed feedback control and temporally correlated noise in excitable systems*, Phil. Trans. R. Soc. A **368**, 391 (2010).

[82] E. J. Doedel and B. E. Oldeman: *Auto-07P: Continuation and bifurcation software for ordinary differential equations*, Concordia University, Montreal, Canada (2009).

[83] R. Benzi, A. Sutera, and A. Vulpiani: *The mechanism of stochastic resonance,*, J. Phys. A **14**, L453 (1981).

[84] E. E. Benoit, J. L. Callot, F. Diener, and M. M. Diener: *Chasse au canard (première partie)*, Collect. Math. **32**, 37 (1981).

[85] E. M. Izhikevich: *Neural excitability, spiking and bursting*, Int. J. Bifurcation Chaos **10**, 1171 (2000).

[86] R. FitzHugh: *Mathematical models of threshold phenomena in the nerve membrane*, Bull. Math. Biol. **17**, 257 (1955).

[87] A. M. Turing: *The chemical basis of morphogenesis*, Phil. Trans. R. Soc. B **237**, 37 (1952).

[88] M. Wolfrum: *The Turing bifurcation in network systems: Collective patterns and single differentiated nodes*, Physica D **241**, 1351 (2012).

[89] P. K. Moore and W. Horsthemke: *Localized patterns in homogeneous networks of diffusively coupled reactors*, Physica D **206**, 121 (2005).

[90] W. Horsthemke, K. Lam, and P. K. Moore: *Network topology and turing instabilities in small arrays of diffusively coupled reactors*, Phys. Lett. A **328**, 444 (2004).

[91] G. Röder, G. Bordyougov, H. Engel, and M. Falcke: *Wave trains in an excitable FitzHugh-Nagumo model: Bistable dispersion relation and formation of isolas*, Phys. Rev. E **75**, 036202 (2007).

[92] G. Bordyougov and H. Engel: *From trigger to phase waves and back again*, Physica D: Nonlinear Phenomena **215**, 25 (2006).

[93] A. Kothe, V. S. Zykov, and H. Engel: *Second universal limit of wave segment propagation in excitable media*, Phys. Rev. Lett. **103**, 154102 (2009).

[94] J. Rademacher, B. Sandstede, and A. Scheel: *Computing absolute and essential spectra using continuation*, Physica D: Nonlinear Phenomena **229**, 166 (2007).

[95] B. Sandstede: *Stability of traveling waves*, in *Handbook of Dynamical Systems*, edited by B. Fiedler (Elsevier/North-Holland, Amsterdam, 2002).

[96] N. E. Kouvaris, T. M. Isele, A. S. Mikhailov, and E. Schöll: *Propagation failure of excitation waves on trees and random networks*, EPL **106**, 68001 (2014).

[97] N. E. Kouvaris and A. S. Mikhailov: *Feedback-induced stationary localized patterns in networks of diffusively coupled bistable elements*, Europhys. Lett. **102**, 16003 (2013).

[98] I. Mitkov, K. Kladko, and J. E. Pearson: *Tunable pinning of burst waves in extended systems with discrete sources*, Phys. Rev. Lett. **81**, 5453 (1998).

[99] A. Carpio and L. L. Bonilla: *Depinning transitions in discrete reaction-diffusion equations*, SIAM J. Appl. Math. **63**, 1056 (2003).

[100] T. M. Isele, B. Hartung, P. Hövel, and E. Schöll: *Excitation waves on a minimal small-world model*, in preparation for Eur. Phys. J. B (2014), in preparation.

[101] T. M. Isele and E. Schöll: *Effect of small-world topology on wave propagation on networks of excitable elements*, arXiv (2014), 1408.5731.

[102] H. Hempel, I. Schebesch, and L. Schimansky-Geier: *Traveling pulses in reaction-diffusion systems under global constraints*, Eur. Phys. J. B **2**, 399 (1998).

[103] K. Krischer and A. S. Mikhailov: *Bifurcation to traveling spots in reaction-diffusion systems*, Phys. Rev. Lett. **73**, 3165 (1994).

Publikationsliste

Teilweise wurden die Ergebnisse aus meiner Dissertationsschrift in den hier aufgelisteten Artikeln veröffentlicht.

- N. E. Kouvaris, T. M. Isele, A. S. Mikhailov, and E. Schöll. Propagation failure of excitation waves on trees and random networks. *EPL*, 106:68001, 2014.
- T. M. Isele and E. Schöll. Effect of small-world topology on wave propagation on networks of excitable elements. *arXiv*, 2014. 1408.5731.
- T. M. Isele, B. Hartung, P. Hövel, and E. Schöll. Excitation waves on a minimal small-world model. *Eur. Phys. J. B*, 2014. in preparation.

Ich habe für jeden dieser Artikel in Zusammenarbeit mit den anderen Autoren die Fragestellung entwickelt, das Manuskript geschrieben Berechnungen angestellt, Daten analysiert und Abbildungen erstellt.

Die Anmeldung einer Promotionsabsicht wurde weder früher noch gleichzeitig bei einer anderen Hochschule oder Fakultät beantragt.

Thomas Isele